

REPORT DOCUMENTATION PAGE			1 Form Approved OMB NO. 0704-0188		
<p>The public reporting burden for this collection of information is estimated to average 1 hour per response, including the time for reviewing instructions, searching existing data sources, gathering and maintaining the data needed, and completing and reviewing the collection of information. Send comments regarding this burden estimate or any other aspect of this collection of information, including suggestions for reducing this burden, to Washington Headquarters Services, Directorate for Information Operations and Reports, 1215 Jefferson Davis Highway, Suite 1204, Arlington VA, 22202-4302. Respondents should be aware that notwithstanding any other provision of law, no person shall be subject to any penalty for failing to comply with a collection of information if it does not display a currently valid OMB control number.</p> <p>PLEASE DO NOT RETURN YOUR FORM TO THE ABOVE ADDRESS.</p>					
1. REPORT DATE (DD-MM-YYYY) 31-08-2014		2. REPORT TYPE Ph.D. Dissertation		3. DATES COVERED (From - To) -	
4. TITLE AND SUBTITLE Quantum Optics with Atom-like Systems in Diamond			5a. CONTRACT NUMBER W911NF-11-1-0400		
			5b. GRANT NUMBER		
			5c. PROGRAM ELEMENT NUMBER 611103		
6. AUTHORS Yiwen Chu			5d. PROJECT NUMBER		
			5e. TASK NUMBER		
			5f. WORK UNIT NUMBER		
7. PERFORMING ORGANIZATION NAMES AND ADDRESSES Massachusetts Institute of Technology (MIT) 77 Massachusetts Ave. NE18-901 Cambridge, MA 02139 -4307			8. PERFORMING ORGANIZATION REPORT NUMBER		
9. SPONSORING/MONITORING AGENCY NAME(S) AND ADDRESS (ES) U.S. Army Research Office P.O. Box 12211 Research Triangle Park, NC 27709-2211			10. SPONSOR/MONITOR'S ACRONYM(S) ARO		
			11. SPONSOR/MONITOR'S REPORT NUMBER(S) 59745-PH-MUR.79		
12. DISTRIBUTION AVAILABILITY STATEMENT Approved for public release; distribution is unlimited.					
13. SUPPLEMENTARY NOTES The views, opinions and/or findings contained in this report are those of the author(s) and should not be construed as an official Department of the Army position, policy or decision, unless so designated by other documentation.					
14. ABSTRACT The nitrogen vacancy (NV) center in diamond is a unique quantum system that combines solid state spin qubits with coherent optical transitions. The spin states of the NV center can be initialized, read out, and controlled with RF fields at room temperature. It can be coupled to other spin systems in the environment while at the same time maintaining an extraordinary degree of quantum coherence. Experiments utilizing the NV center's spin states have led to a wide range of demonstrations from quantum error correction to high-sensitivity magnetometry. This thesis, however, focuses on creating an interface between NV centers and light in the visible domain by making use of its					
15. SUBJECT TERMS QuISM					
16. SECURITY CLASSIFICATION OF:			17. LIMITATION OF ABSTRACT UU	15. NUMBER OF PAGES	19a. NAME OF RESPONSIBLE PERSON Paola Cappellaro
a. REPORT UU	b. ABSTRACT UU	c. THIS PAGE UU			19b. TELEPHONE NUMBER 617-253-8137

## **Report Title**

### **Quantum Optics with Atom-like Systems in Diamond**

#### **ABSTRACT**

The nitrogen vacancy (NV) center in diamond is a unique quantum system that combines solid state spin qubits with coherent optical transitions. The spin states of the NV center can be initialized, read out, and controlled with RF fields at room temperature. It can be coupled to other spin systems in the environment while at the same time maintaining an extraordinary degree of quantum coherence. Experiments utilizing the NV center's spin states have led to a wide range of demonstrations from quantum error correction to high-sensitivity magnetometry. This thesis, however, focuses on creating an interface between NV centers and light in the visible domain by making use of its optical transitions. Such an interface connects the quantum system consisting of NV centers and nuclear spins to photons, which can then be used to both manipulate the spin qubits themselves or transport quantum information over large distances.

HARVARD UNIVERSITY  
Graduate School of Arts and Sciences



DISSERTATION ACCEPTANCE CERTIFICATE

The undersigned, appointed by the  
Department of Physics  
have examined a dissertation entitled

Quantum optics with atom-like systems in diamond

presented by Yiwen Chu

candidate for the degree of Doctor of Philosophy and hereby  
certify that it is worthy of acceptance.

Signature

A handwritten signature in blue ink, appearing to read "M. Lukin", written over a horizontal line.

Typed name: Professor Mikhail Lukin, Chair

Signature

A handwritten signature in blue ink, appearing to read "John Doyle", written over a horizontal line.

Typed name: Professor John Doyle

Signature

A handwritten signature in blue ink, appearing to read "Evelyn Hu", written over a horizontal line.

Typed name: Professor Evelyn Hu

Date: November 19, 2013



# Quantum optics with atom-like systems in diamond

A dissertation presented

by

Yiwen Chu

to

The Department of Physics

in partial fulfillment of the requirements

for the degree of

Doctor of Philosophy

in the subject of

Physics

Harvard University

Cambridge, Massachusetts

November 2013

©2013 - Yiwen Chu

All rights reserved.

Dissertation Advisor:

Author

**Professor Mikhail D. Lukin****Yiwen Chu****Quantum optics with atom-like systems in diamond****Abstract**

The nitrogen vacancy (NV) center in diamond is a unique quantum system that combines solid state spin qubits with coherent optical transitions. The spin states of the NV center can be initialized, read out, and controlled with RF fields at room temperature. It can be coupled to other spin systems in the environment while at the same time maintaining an extraordinary degree of quantum coherence. Experiments utilizing the NV center's spin states have led to a wide range of demonstrations from quantum error correction to high-sensitivity magnetometry. This thesis, however, focuses on creating an interface between NV centers and light in the visible domain by making use of its optical transitions. Such an interface connects the quantum system consisting of NV centers and nuclear spins to photons, which can then be used to both manipulate the spin qubits themselves or transport quantum information over large distances.

We begin by introducing the structure, symmetry, and energy levels of the NV center that give rise to its optical properties. We then present the demonstration of entanglement between the electronic spin of the NV center and an optical photon. In addition to being the first step toward using NV centers in long distance quantum networks, this work showed that coherent control of optical transitions in the NV

*Abstract*

---

center is possible. Inspired by this, we then demonstrated all-optical sensing and manipulation of the nuclear spin bath using coherent population trapping of the NV center. We then turn to the issue of moving beyond these proof-of-principle experiments toward implementing robust and scalable diamond-based photonic devices. To this end, we demonstrate the creation of spectrally stable NV centers in a device layer near the diamond surface. Finally, we discuss the implementation of nanophotonic devices to enhance the interactions between NV centers and light.



# Contents

Title Page . . . . .	i
Abstract . . . . .	iii
Table of Contents . . . . .	v
Citations to Previously Published Work . . . . .	viii
Acknowledgments . . . . .	ix
Dedication . . . . .	xv
<b>1 Introduction</b>	<b>1</b>
1.1 Background . . . . .	1
1.2 Overview of thesis . . . . .	4
1.2.1 Optical properties of NV centers . . . . .	5
1.2.2 Spin-photon entanglement . . . . .	6
1.2.3 All optical measurement and manipulation of the nuclear spin bath . . . . .	7
1.2.4 Creation of optically coherent NV centers . . . . .	8
1.2.5 Nanophotonics with NV centers . . . . .	9
<b>2 Optical properties of the NV center</b>	<b>10</b>
2.1 Introduction . . . . .	10
2.2 Level structure and polarization properties of the NV center . . . . .	12
2.2.1 Electronic states of the NV center . . . . .	12
2.2.2 Properties of optical transitions . . . . .	17
2.2.3 The effect of strain . . . . .	18
2.3 Experimental techniques . . . . .	19
2.3.1 Diamond materials . . . . .	21
2.3.2 Experimental setup for optical characterization of NV centers . . . . .	24
2.3.3 PLE spectroscopy of NV centers . . . . .	26
2.4 Studies of the optical properties of NV centers . . . . .	29
2.4.1 Optical Rabi oscillations and resonant spin readout . . . . .	31
2.4.2 Multi-level systems and all-optical spin manipulation . . . . .	34

## Contents

---

<b>3</b>	<b>Quantum entanglement between an optical photon and a solid-state spin qubit</b>	<b>42</b>
3.1	Introduction . . . . .	42
3.2	Characterization of NV centers . . . . .	44
3.3	Experimental demonstration of spin-photon entanglement . . . . .	47
3.4	Conclusions and outlook . . . . .	53
<b>4</b>	<b>Laser cooling and real-time measurement of nuclear spin environment of a solid-state qubit</b>	<b>54</b>
4.1	Introduction . . . . .	54
4.2	Coherent population trapping with NV centers . . . . .	56
4.3	Optical cooling and conditional preparation of $^{14}\text{N}$ nuclear spin states . . . . .	59
4.4	Observation of instantaneous Overhauser field from the $^{13}\text{C}$ spin bath . . . . .	61
4.5	Measurement-based preparation of $^{13}\text{C}$ spin bath . . . . .	64
4.6	Conclusions and outlook . . . . .	68
<b>5</b>	<b>Coherent optical transitions in implanted nitrogen vacancy centers</b>	<b>69</b>
5.1	Introduction . . . . .	69
5.2	Procedure for NV center creation . . . . .	72
5.3	Spectroscopy of implanted NV centers . . . . .	74
5.4	Mechanism for NV center creation . . . . .	77
5.5	Conclusions . . . . .	79
<b>6</b>	<b>Diamond-based nanophotonic devices</b>	<b>82</b>
6.1	Introduction . . . . .	82
6.2	Cavity QED with NV centers . . . . .	84
6.3	Diamond-based nanophotonic devices . . . . .	88
6.4	Spectral properties of NV centers inside nanoscale structures . . . . .	93
6.5	Purcell enhancement from a coupled NV-cavity system . . . . .	94
<b>7</b>	<b>Conclusions and outlook</b>	<b>98</b>
<b>A</b>	<b>Supporting material for Chapter 3</b>	<b>103</b>
A.1	Calculation of entanglement fidelity . . . . .	103
A.2	Experimental details . . . . .	104
A.2.1	Overview of experimental setup . . . . .	104
A.2.2	Optical setup . . . . .	106
A.2.3	Microwave control . . . . .	107
A.2.4	Experiment control and data acquisition . . . . .	109
A.3	Spin readout . . . . .	110
A.4	Verification of polarization selection rules for $ A_2\rangle$ state . . . . .	116
A.5	Effects of magnetic environment, detunings, and echo . . . . .	119
A.5.1	Effect of finite detuning . . . . .	120

## Contents

---

A.5.2	Spin echo sequence . . . . .	121
A.6	Fidelity estimates . . . . .	123
A.6.1	Time bin optimization . . . . .	123
A.6.2	Maximum likelihood estimate . . . . .	124
<b>B</b>	<b>Supporting material for Chapter 4</b>	<b>130</b>
B.1	Experimental details . . . . .	130
B.1.1	Sample description . . . . .	130
B.1.2	Experimental setup . . . . .	131
B.1.3	Effects of ionization and other forms of spectral drift . . . . .	132
B.2	Multilevel description of the NV center . . . . .	133
B.3	Measurement of branching ratios . . . . .	137
B.4	$^{14}\text{N}$ polarization via optical pumping and measurement based preparation	139
B.4.1	Optical Pumping . . . . .	139
B.4.2	Details of measurement based preparation . . . . .	141
B.5	Strain dependence of CPT width . . . . .	142
B.6	Autocorrelation measurements and spectral density of signal . . . . .	146
B.7	Nuclear configuration measurements using fast magnetic field ramps .	148
B.8	$B_{\text{prep}}$ dependence of the observed width . . . . .	151
B.9	Lifetime in the absence of optical fields . . . . .	154
B.10	Discussion . . . . .	155
	<b>Bibliography</b>	<b>158</b>

# Citations to Previously Published Work

Parts of Chapter 2 have appeared as the supplementary information to the following two papers:

“Quantum entanglement between an optical photon and a solid-state spin qubit”, E. Togan, Y. Chu, A. S. Trifonov, L. Jiang, J. Maze, L. Childress, M. V. G. Dutt, A. S. Sørensen, P. R. Hemmer, A. S. Zibrov & M. D. Lukin *Nature* **466**, 730734 (2010);

“Laser cooling and real-time measurement of the nuclear spin environment of a solid-state qubit”, E. Togan, Y. Chu, A. Imamoglu & M. D. Lukin, *Nature* **478**, 497501 (2011).

and Chapter 3, in its entirety, has been published as

“Quantum entanglement between an optical photon and a solid-state spin qubit”, E. Togan, Y. Chu, A. S. Trifonov, L. Jiang, J. Maze, L. Childress, M. V. G. Dutt, A. S. Sørensen, P. R. Hemmer, A. S. Zibrov & M. D. Lukin *Nature* **466**, 730734 (2010).

and Chapter 4 appears, in its entirety, as

“Laser cooling and real-time measurement of the nuclear spin environment of a solid-state qubit”, E. Togan, Y. Chu, A. Imamoglu & M. D. Lukin, *Nature* **478**, 497501 (2011).

# Acknowledgments

To begin, I would like to thank my advisor, Misha Lukin. In the time that I worked with him, he has taken on innovative and courageous projects that led the field of quantum optics with solid-state systems toward whole new directions. I feel very fortunate to have been part of this process and to have had an advisor with so much knowledge, patience, and concern for his students. One of my first impressions of Misha involved the quite alarming statement "No ice cream for you guys until you tell me resonant photon scattering cross section!" However, I soon discovered that, far from being intimidating, my conversations with him turned out to always be enlightening and encouraging. I have come away from them with much valuable advice on science, on doing science, and on living life while doing science. These I will always remember and be grateful for.

Next, I would like to thank my other committee members, John Doyle and Evelyn Hu. Most of the work presented in Chapters 2, 3 and 4 were actually done in a lab belonging to the Doyle group. I am very grateful to John for his generosity in providing us with such an auspicious space and to his group for being such accommodating neighbors. I want to thank Evelyn for her support and kindness over the years. We've all been lucky to have her as the newest member of the Harvard "diamond community".

In addition, I've had the fortunate opportunity to interact with a number of other professors and groups, both at Harvard and from around the world. First, I want to thank Fedor Jelezko, who was instrumental in starting our very first experiments. To this day, he continues to be one of the most valuable sources of knowledge and expertise in the field. His generosity has set a precious example of collaboration

## *Acknowledgments*

---

and openness for the entire community. Phil Hemmer and Anders Sørensen made possible the earliest work on spectroscopy of NV centers and inspired the idea for the work presented in Chapter 3. It was a great pleasure working with Atac Imamoglu, whose knowledge and insight has been invaluable to us. I also want to thank him for his hospitality during my visits to Zurich. I would like to thank Adam Gali for his contributions to our understanding of the NV center and diamond material. The many professors at Harvard working on NV centers have also been a great resource to me. I've had the pleasure of working closely with Marko Loncar, whose pioneering work on diamond fabrication made possible the work presented in 5 and 6. His inexhaustible enthusiasm and excitement for science is contagious, and I am still searching for further evidence of his alternate persona as a rock star. I've also greatly enjoyed collaborating with Hongkun Park and his group. His presence at our nanophotonics meetings often provided (at times much needed) motivation and impetus for moving forward. Ron Walsworth has also been an unfailing source of encouragement, and I want to thank him for his version of events concerning my dramatic escape from the PRC and subsequent "blossoming" in the fertile environment that is the Harvard university physics department. It has also been a great help to exchange knowledge and information with Amir Yacoby and his diamond team. Finally, I want to thank the Doyle, Greiner, and Gabrielse groups for sharing their vast technical expertise.

I have worked with a large number of extremely talented post-docs and students during grad school. This thesis certainly would not have been possible without them. First and foremost, I would like to thank my colleague, mentor, and dear friend Emre Togan. I deeply admire his incredible humility and patience, even more so considering

## *Acknowledgments*

---

that he is one of the most talented and hard-working people I know. Together, we have shared the joy of discovery, like when we saw our first dark state resonance while dancing around the lab with magnets in our hands. However, the true tests of our collaboration were those numerous times of frustration, but I could not have asked for a better person with whom to have searched long and hard for tiny handfuls of precious ZPL photons. I could write a whole chapter thanking Emre for teaching me everything from proper micrometer turning ergonomics to the Turkish alphabet to conserving angular momentum on a bike, but words in any language would not even come close to expressing the extent of my gratitude to him.

Sharing the excitement of those years in the Lyman basement with Emre and I were several other intrepid NV center experimentalists. I hope that Lily Childress, Gurudev Dutt, Alexei Trifonov, Jero Maze, Johnathan Hodges, Paul Stanwix, and Liang Jiang remember that crowded and dark little room with as much fondness as I do. I've learned so much from all of them. I especially want to thank Jero and Liang, the multitalented theorist-experimentalists. Their work on the theoretical description of the NV center's level structure and optical properties made much of this thesis possible. I also want to thank Lily for her advice and support, and for her masterpiece, the AMO class notes, which has been my bible all these years.

I would like to acknowledge Nathalie de Leon and Ruffin Evans, who worked with me on the diamond nanophotonics project in more recent times. Nathalie has always impressed me with her confidence, work ethic, and vast knowledge in so many scientific subjects. Ruffin's enthusiasm for new information and novel ideas has also been inspiring, and I wish the two of them the best of luck in continuing this exciting and

## *Acknowledgments*

---

challenging project. There were also many others who made important contributions to this effort over the years. It was a great privilege to work with diamond fabrication pioneer Birgit Hausmann from the Loncar group, who is also an incredibly kind and joyful person to be around. In these last few months, I've also discovered a great collaborator in Michael Burek, and I look forward to continuing to work with him in my remaining time here. From the Yacoby group, I'd like to thank Patrick Maletinsky, who first suggested investigating the optical properties of high-temperature annealed diamond. I don't know where we'd all be if it weren't for his persistence and great ideas. I've also had the pleasure of working with Brendan Shields, who, in addition to being my colleague, has also been, among other things, my friend, my violinist, and my go-to person for talking about science, life, and basically anything else. Grad school would surely would not have been the same without him.

There are also several people who have been bottomless sources of knowledge and expertise for me. My am very grateful for the help of Sasha Zibrov, the laser whisperer who whispers in Russian, Stan Cotreau, who has the unfathomably difficult job of making sure a bunch of bumbling grad students don't hurt themselves in the machine shop, and Jim MacArthur, who can make anything your heart desires as long as your heart desires electronics (which mine often does). I am also grateful to the diamond-growers at Element Six, Daniel Twitchen, Matthew Markham, and Alastair Stacey, along with the staff of CNS for their patient help and support.

I would like to thank Adi Pick and Swati Singh for giving me the opportunity to foray into being a theorist, and for their persistence and patience in working on such a difficult project. I also enjoyed briefly working with Michael Goldman and Alex



## *Acknowledgments*

---

Kubaneck on Fabry-Perot cavities, and I'm glad to hear that there are plans to renew that effort.

I have benefitted greatly from discussions and interactions with many current and past members of the Lukin group. I am deeply grateful to them for providing such a supportive and intellectually stimulating community. There are simply too many at this point to list all of them by name, but I would like to especially thank a few of my closest friends from the group who have not already been mentioned. Nick Chisholm has been a constant source of support and kindness, even in the toughest of times. Alp Sipahigil, who is really just too cool for any of us, has nevertheless deigned to be my personal tour guide, serenader, and guide into brave new experiences. I thank him for many enlightening discussions about physics, for his good humor when I try to say things in Turkish, and for never giving up on me or our friendship. Last, but certainly not least, my deepest gratitude goes to Norman Yao, with whom I've shared an office, a castle, and countless stories. I have never encountered such a combination of brilliance and joyful energy in another human being, and often times I wonder if I am in the presence of superman himself. I am truly honored by his trust in me, and look forward to soon becoming the confidant of one of the great physicists of our time. For my dear friends Norm, Emre, Brendan, and Alp, I present Figure 0.1 as graphical representation of how much fun we had in grad school, should they ever need a reminder.

There have been times in grad school when I could have easily lost track of the outside world, but I am fortunate that I've always had wonderful people to pull me back. I want to thank Chris Laumann for taking me horseback riding and my

## Acknowledgments

---

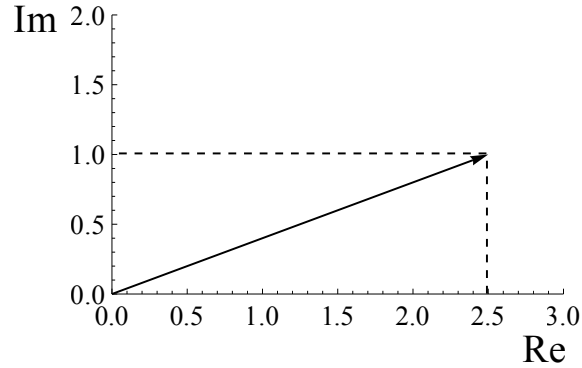


Figure 0.1: Perhaps a steady state, perhaps not.

classmates for our days puppeteering and mountaineering together. My friends and floor-mates from college, Ming Yi, Pei-Lan Hsu, Nivedita Chandrasekaran, and Risa Kawai, have been the much needed voices of sanity and perspective for me. I would also like to thank Deborah Pan. I could not have asked for a better roommate and friend.

Finally, I am grateful to my parents Leilei and Shaoyan for their endless support and patience. I learned my first bit of physics from one of them at an age that I can no longer recall, and the other has encouraged me to keep at it to this day. I know that I can never fully appreciate everything they have done for me, but I also know that I would have never reached this milestone without them.

*To my parents*

# Chapter 1

## Introduction

### 1.1 Background

The study of classical mechanics, thermodynamics, and electromagnetism have brought on great technological advances over the course of history. We now live in an exciting era where quantum mechanics begins to join these other fields of physics in enabling new technologies with unprecedented capabilities. Theoretical and experimental efforts have moved toward harnessing the power of various different physical systems for applications in metrology, quantum information, and furthering our understanding of quantum mechanics itself.

Some of the most successful of applications of quantum mechanical systems to date have been in the field of metrology, or the accurate sensing and measurement of forces, fields, frequencies, etc. One important example of such a quantum technology is the optical clock, which provides high accuracy standards for frequency and time based on the fundamental stability of transition frequencies between quantum states of neutral

atoms or trapped ions [1, 2]. One challenge of implementing such optical clocks is lies in reducing the uncertainty of the clock transition frequency caused by external effects. To this end, for example, different atomic species and level structures have been extensively studied to find transitions between energy levels that are particularly insensitive to external electromagnetic fields. In addition, the atoms are trapped and cooled using ion traps or optical lattices to reduce the effect of atomic motion. The other major challenge is developing techniques for probing the transition frequency with high enough resolution and stability. This has led to the development of, for example, high quality optical cavities for laser stabilization and the use of frequency combs for analyzing and comparing the accuracy of different clocks [3, 4].

The field of quantum information and communications has given rise to another class of quantum technologies that has become the focus of much effort in recent years. There has been a large number of theoretical proposals for using quantum systems for efficient computation, simulation of complex systems, secure dissemination of information, etc. [5, 6, 7]. However, the practical implementation of these proposals in real physical systems remains an open challenge. A variety of different avenues are being actively explored, ranging from photons, neutral atoms, ions, impurities and structures in solid state systems, to more exotic materials such as electrons on the surface of liquid helium [8, 9, 10, 11, 12]. To get a sense of both the exciting developments and difficult challenges of this field, one can look at the example of superconducting quantum bits (qubits). This class of qubits consists of devices constructed from superconducting circuit elements such as Josephson junctions and engineered to satisfy requirements such as energy level anharmonicity, addressability,

and immunity to external perturbations [10]. When these qubits are integrated with resonator and waveguide structures, they can be initialized, manipulated, and read out with very high fidelity through microwave fields [13, 14]. In addition, the strong coupling achievable between superconducting qubits and microwave resonators have led to demonstrations of multi-qubit gates and operations that pave the way towards scalable architectures for quantum computation [15, 16]. As complex mesoscopic systems, however, these qubits can be highly sensitive to their environment, which leads to loss of quantum information through decoherence. Tremendous progress has been made to isolate these systems from the environment, with qubit relaxation and decoherences times increasing from nanoseconds to nearly 0.1 ms in a little over a decade [17, 18, 19]. However, fully understanding the underlying mechanisms for decoherence in these systems will require further studies in the fields of material science, surface chemistry, and the physics of superconductors [20, 21].

From the above examples, it can be seen that a common theme for the implementation of quantum technologies is the seemingly contradictory need for controllability and isolation from external effects. Undesirable effects of the environment must be minimized, while at the same time techniques and tools must be developed that enable us to interact with the system in a controllable and well-defined manner. This thesis addresses several aspects of this theme with regards to a particularly promising candidate for developing applications in both metrology and quantum information: the nitrogen-vacancy (NV) center in diamond. In particular, we explore how the NV center can be investigated, controlled, and efficiently coupled with optical photons, and tackle the challenges of controlling the optical properties of these emitters inside

a complex solid-state environment.

As with other solid state systems such as quantum dots, rare earth dopants in inorganic crystals, and superconducting qubits, NV centers present the attractive feature of eliminating the need for trapping and cooling, as is usually required for atomic systems. In addition to greatly reducing the complexity of experiments, solid state systems offer the possibility of straightforward integration with fabricated structures and development of scalable quantum devices. The issue of scalability, however, is not simply a matter of being able to create a large number of physical devices in a small volume. In order to truly move beyond proof-of-principle experiments, the properties of many qubits and devices must all be well controlled in a reproducible, reliable, and efficient manner. In other words, while it is important to demonstrate that a certain quantum operation, coherence time, metrological sensitivity, etc. is possible in one particular device with favorable characteristics, it must also be possible to reproduce these characteristics for a large number of systems.

## **1.2 Overview of thesis**

With the above considerations in mind, this thesis is organized as follows. After an introduction to the system we are working with, we present two proof-of-principle experiments where the NV center is utilized as an interface between spin qubits and light. The first is a crucial step toward the implementation of long-distance quantum communication schemes, while the second demonstrates the power of this optical interface for controlling the spin qubits themselves. In the following chapter, we then lay the groundwork for future quantum devices based on these types of experiments by

developing a method for reliably creating NV centers with desirable optical properties inside a well-controlled environment. This then opens up the possibility of creating structures to tailor the interactions between NV centers and photons, which will be explored in the next chapter. Finally we will conclude by discussing some remaining challenges for implementing quantum devices with NV centers and light, and present an outlook for the field.

### **1.2.1 Optical properties of NV centers**

Unlike atomic systems, where optical spectroscopy has been used for decades to elucidate the energy levels and interactions of the system, a complete and detailed description of the NV center's level structure has only become fully developed over the past several years. Chapter 2 gives a theoretical description of the optical transitions, along with a collection of experimental methods and results concerning spectroscopy of NV centers. The model of the NV center's electronic structure is built up from symmetry considerations followed by the inclusion of various interactions and external effects such as spin-orbit, spin-spin, and crystal strain. We then describe the experimental techniques that are used to investigate the NV center's optical properties through PLE spectroscopy and coherent manipulation. Finally, we demonstrate the interplay between the spin and electronic degrees of freedom by using the optical transitions to probe and control the ground state spin sublevels. The ideas and techniques described in this chapter provide the foundation for the work presented in the rest of the thesis.



### 1.2.2 Spin-photon entanglement

Chapter 3 describes the realization of quantum entanglement between a NV center and a single photon. The scheme we use is inspired by previous work done in trapped ions [22]. Based on our knowledge of the NV center’s level structure, as described in Chapter 2, we identify a  $\Lambda$  type three-level structure that enables the generation of entanglement between the  $m_s = \pm 1$  spin sublevels of the NV center’s ground state and the polarization degree of freedom of spontaneously emitted photons. In addition, we demonstrate resonant readout of the spin-state of the NV center using a different, cycling optical transition involving the  $m_s = 0$  spin states, which allows us to verify the fidelity of the entanglement.

The demonstration of spin-photon entanglement is the first step in implementing a quantum network architecture for long-distance quantum communications using NV centers [6]. Such an entangled state connects the solid state, spin-based local quantum register with optical photons, which can then be disseminated over free space or through optical fibers. Following this experiment, tremendous progress has been made in achieving the next steps in building a diamond-based quantum network. Hong-Ou-Mandel interference was demonstrated with indistinguishable photons from remote NV centers hosted in separate diamond samples [23, 24]. Combined with spin-photon entanglement, this allowed for the remote entanglement of two NV centers separated by a distance of three meters through entanglement swapping [25].

### 1.2.3 All optical measurement and manipulation of the nuclear spin bath

In addition to being an ideal carrier of quantum information over long distances, optical fields are also powerful tools for quantum control of the local system associated with the NV center. In Chapter 4, we use the optical transitions of the NV center to sense and manipulate its surrounding spin bath, which consists of the spin of the  $^{14}\text{N}$  nucleus associated with the NV center itself and the  $^{13}\text{C}$  nuclei in the diamond lattice. We do this by making use of the same  $\Lambda$  type system involved in generating spin-photon entanglement. Such a level structure allows us to use coherent population trapping to optically pump the NV center into a particular dark state of the  $m_s = \pm 1$  spin sublevels if their energies satisfy a two-photon resonance. The energies of these spin sublevels are in turn determined by the Zeeman splitting due to a combination of the externally applied magnetic field and the Overhauser field from nuclear spin bath. Therefore, by monitoring the photons collected from the NV center for different external fields, we are able to determine the state of the nuclear spins on a timescale faster than their inherent dynamics. In addition, our measurement can be used to prepare the spin bath in a well-defined state. Such a decrease in the uncertainty of the nuclear spin state can be used to improve the sensitivity of diamond-based magnetometers by reducing the decoherence caused by hyperfine coupling between the NV center and the spin bath. In addition, this work has inspired ongoing experimental and theoretical work in studying the complex dynamics of the nuclear spin bath itself and its interactions with the NV center under optical addressing. For example, there are indications that such a scheme can be used to observe Levy-flight statistics in a

single quantum system [26, 27].

### **1.2.4 Creation of optically coherent NV centers**

The experiments presented in Chapters 4 and 3 were both performed using a natural diamond sample, known as the "Magic Russian Diamond", that was one-of-a-kind in its resolvable concentration of native NV centers with stable, coherent optical transitions. However, such specialized samples can only be used for proof-of-principle experiments, while the development of scalable diamond-based quantum optical devices requires high quality starting materials that are reproducible. Such a material has two basic requirements. First, the NV centers must have optical transitions that are stable in frequency, which is in general not the case due to spectral diffusion caused by fluctuations in the local charge environment. Second, they must be introduced at a well-defined depth and concentration near the surface of the diamond to allow for incorporation into structures and devices. To this end, Chapter 5 presents a method for satisfying both of these requirements by creating NV centers inside synthetic diamond material through a combination of techniques including ion implantation, high temperature annealing, and surface treatments. The resulting NV centers demonstrate spectral diffusion that can be less than a factor of three of the lifetime-limited linewidth of the optical transition, which is a record for the spectral stability of NV centers in any material. The depth and concentration of the NV centers can also be controlled by the energy and dose of the implantation. This work provides an ideal starting material for the creating of diamond-based nanophotonic structures, which are discussed in the next chapter.

### 1.2.5 Nanophotonics with NV centers

In this last chapter, we describe some preliminary work to create structures and devices to enhance the interaction between NV centers and light. These devices will be necessary for using techniques such as those demonstrated in Chapters 3 and 4 to build efficient optical devices based on NV centers. We begin by discussing how cavity quantum electrodynamics (cQED) can be used to effectively improve the quality of the NV center's optical properties and increase the amount of useful, coherent photons that can be extracted from the system. Starting with the material developed in Chapter 5, we describe several directions for the fabrication of nanoscale structures such as photonic crystal cavities. Using one such device, we demonstrate Purcell enhancement of coherent emission from the NV center, which is an important step toward implementing scalable, diamond-based optical devices based on interactions between NV centers and photons.

## Chapter 2

# Optical properties of the NV center

### 2.1 Introduction

Optical spectroscopy is a powerful tool for determining the structure and behavior of quantum systems, and has historically been the main experimental method contributing to the understanding of atoms, ions, and molecules. There are now well-established methods in the field of atomic, optical and molecular physics for trapping, cooling, and manipulating the internal states of these systems with light. More recently, however, there has been significant interest in discovering and exploring solid state systems that exhibit atom-like optical properties for the goal of building scalable, compact devices. Great progress has been made in understanding and utilizing the optical properties of, for example, self-assembled quantum dots, dye molecules embedded in organic matrix materials, rare earth ions in doped crystals, and impurities

in insulators and semiconductors [28, 29, 30, 31].

Diamond is a particularly interesting host material for optically active quantum emitters due to its wide bandgap (5.5 eV) and consequently large transparency window. It supports a huge variety of impurities and defects that give rise to optical bands at energies throughout the infrared and visible spectrum [32]. The NV center is unique in that it combines well-defined optical transitions with long-lived spin sublevels in the ground state, much like alkali atoms with transitions involving hyperfine sublevels. In recent years, a comprehensive theoretical model has been developed to describe the spin and optical properties of the NV center. We begin this chapter by summarizing this theoretical framework, which allows us to understand the underlying physics of the subsequent experimental results. We then describe the experimental techniques that are used to investigate and address the optical properties of NV centers. As part of this description, we will encounter some general characteristics of the system that will become important issues to be addressed later in the thesis, such as the Debye-Waller factor and the sensitivity of the excited state to the local environment. Based on our theoretical understanding and spectroscopic results, we find that the level structure of the NV center gives rise to a rich set of possibilities for coherent optical control of the system. In particular, we show that the spin state of the NV center can be measured and manipulated all optically.

## 2.2 Level structure and polarization properties of the NV center

As is the case in any system, the electronic structure of the NV center can be analyzed by considering its symmetry, in addition to the various interactions that are present. Our description below starts with electronic states that obey the  $C_{3v}$  symmetry of the NV center. We then consider the effect of various interactions one by one, starting from the the Coulomb interaction that sets the energy scale of the optical transitions. Spin-orbit and spin-spin interactions act to lift the degeneracy of the different states in the ground and excited state manifolds. Finally, we consider the effect of external perturbations such as electric and magnetic fields that change the nature and energies of the unperturbed states. More detailed analysis of many of the concepts presented in this section can be found in [33].

### 2.2.1 Electronic states of the NV center

The negatively-charged NV center has six electrons, five of which are from the nitrogen and the three carbons surrounding the vacancy. They occupy the orbitals states  $a'_1, a_1, e_x, e_y$ , which are combinations of the four dangling bonds surrounding the vacancy that satisfy the symmetry imposed by the nuclear potential. These states can be written as

$$a'_1 = \alpha \frac{\sigma_1 + \sigma_2 + \sigma_3}{3} + \beta \sigma_n, \quad (2.1)$$

$$a_1 = \beta \frac{\sigma_1 + \sigma_2 + \sigma_3}{3} + \alpha \sigma_n, \quad (2.2)$$

$$e_x = \frac{2\sigma_1 - \sigma_2 - \sigma_3}{\sqrt{6}}, \quad (2.3)$$



Figure 2.1: Single electron orbitals of the NV center. The nitrogen and three carbons surrounding the vacancy are shown, and the perspective is along the NV axis. The color scale roughly represents the sign and occupation of each orbital.

$$e_y = \frac{\sigma_2 - \sigma_3}{\sqrt{2}} \quad (2.4)$$

where  $\sigma_1$ ,  $\sigma_2$ ,  $\sigma_3$  and  $\sigma_n$  are the dangling bonds from the three carbons and the nitrogen, respectively. These orbitals transform as the irreducible representations of the  $C_{3v}$  group and have been extensively used by many authors [34, 35, 36, 37]. They are schematically illustrated in Figure 2.1 to give an idea of their symmetries. From these pictorial representations, one can deduce that, for example,  $\langle e_y | \hat{y} \cdot \vec{r} | e_x \rangle = \langle e_x | \hat{x} \cdot \vec{r} | e_y \rangle = -\langle e_y | \hat{x} \cdot \vec{r} | e_y \rangle \neq 0$ . This means that the  $|e_x\rangle$  and  $|e_y\rangle$  states have permanent electric dipole moments, which will become important later for understanding the electric field sensitivity of the NV center's excited states and spectral diffusion of the optical transitions. In addition, one also sees that  $\langle a | \hat{x} \cdot \vec{r} | e_x \rangle = \langle a | \hat{y} \cdot \vec{r} | e_y \rangle \neq 0$ , which gives rise to the transition dipole moments between the ground and excited states. These properties will be discussed in more detail in the following sections.

In the ground state of the NV center, the  $a'_1$  and  $a_1$  states, which are lowest in energy, are filled by four electrons, as shown in Figure 2.2. The remaining two electrons occupy the degenerate orbitals  $e_x$  and  $e_y$ . The orbitals  $e_x$  and  $e_y$  can be viewed as  $p$ -type orbitals, and we can define their combinations,  $e_+ = -e_x - ie_y$ ,  $e_- = e_x - ie_y$ , that are analogous to  $p$  states with definite orbital angular momentum. An antisymmetric combination of the orbital states minimizes the Coulomb energy



and results in a spin-triplet ground state manifold

$$|{}^3A_2\rangle = |E_0\rangle \otimes \begin{cases} | +1\rangle \\ | 0\rangle \\ | -1\rangle \end{cases} \quad (2.5)$$

where  $|\pm 1\rangle, |0\rangle$  correspond to the  $m_s = \pm 1, 0$  states, respectively. The notation  $|E_0\rangle = |e_x e_y - e_y e_x\rangle$  indicates that the orbital state has 0 orbital angular momentum projection along the NV axis.  $A_2$  denotes the orbital symmetry of the state, which is determined by the symmetries of the  $e_x$  and  $e_y$  orbitals. From here on, we will often denote these ground states simply as  $|0\rangle$  and  $|\pm 1\rangle$  when it's clear that we are referring to the full electronic state and not just the spin projections.

The relevant excited state for the optical transitions of the NV center is a pair of triplets which arises from the promotion of one of the electrons occupying the orbital  $a_1$  to the  $e_x$  or  $e_y$  orbitals [35]. Note that this state can be modeled by one hole in the orbital  $e$  and another hole in the orbital  $a_1$ , i.e. a triplet in the  $ae$  electronic configuration (similarly, the ground state can be modeled by two holes in the  $e^2$  electronic configuration). A total of six states can be formed in this configuration and their symmetries are determined by a group theoretical analysis [33],

$$\begin{aligned} |A_1\rangle &= |E_-\rangle \otimes | +1\rangle - |E_+\rangle \otimes | -1\rangle \\ |A_2\rangle &= |E_-\rangle \otimes | +1\rangle + |E_+\rangle \otimes | -1\rangle \\ |E_x\rangle &= |X\rangle \otimes |0\rangle \\ |E_y\rangle &= |Y\rangle \otimes |0\rangle \\ |E_1\rangle &= |E_-\rangle \otimes | -1\rangle - |E_+\rangle \otimes | +1\rangle \\ |E_2\rangle &= |E_-\rangle \otimes | -1\rangle + |E_+\rangle \otimes | +1\rangle \end{aligned} \quad (2.6)$$

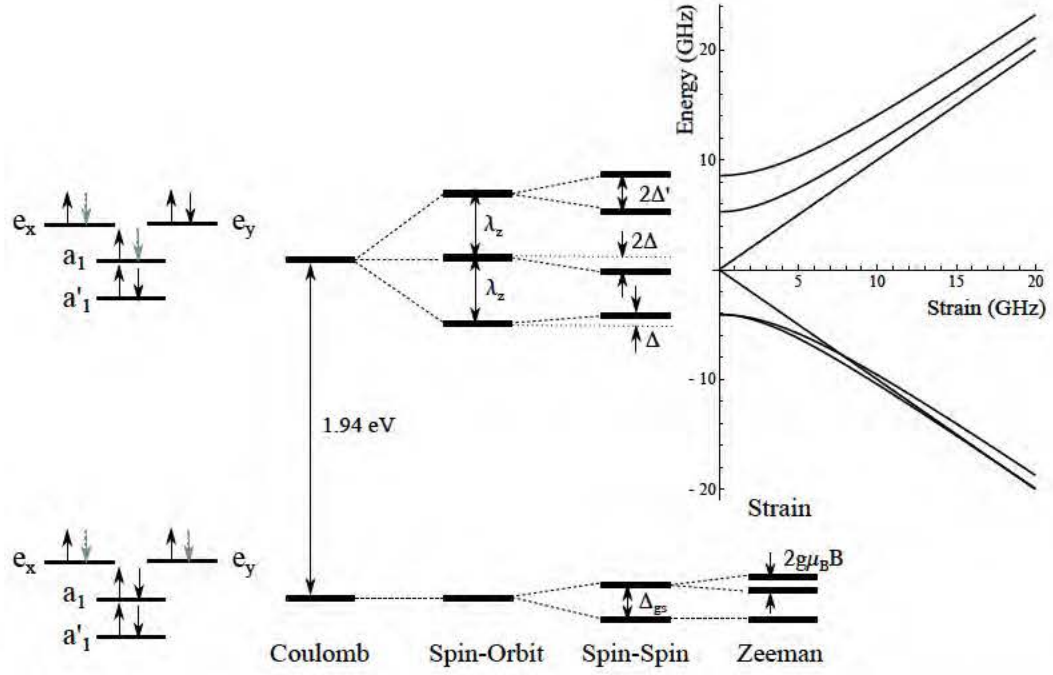


Figure 2.2: Ground and excited states associated with the NV center's optical transitions. The four symmetrized states are filled by six electrons, which can also be viewed as two holes (indicated with green, dashed arrows). The Coulomb interaction defines the optical transition energy of the NV center. The effect of the spin-orbit and spin-spin interactions are indicated for both the ground and excited states. In the ground state, the application of a magnetic field further splits the  $|m_s = \pm 1\rangle$  states due to the Zeeman interaction. In the excited state, crystal strain modifies the energies of sublevels.

where we have named the first four states as  $A_1$ ,  $A_2$ ,  $E_x$  and  $E_y$  according to their symmetries and named the last two states as  $E_1$  and  $E_2$  since they also transform according to the irreducible representation  $E$ . Here,  $|E_{\pm}\rangle = |ae_{\pm} - e_{\pm}a\rangle$  and  $|X(Y)\rangle = |ae_{x(y)} - e_{x(y)}a\rangle$ .

As spin-orbit and spin-spin interactions are invariant under any operation of the  $C_{3v}$  group, the states given in equation (2.6) are eigenstates of the full Hamiltonian including these interactions and in the absence of any perturbation such as magnetic field and/or crystal strain. The Hamiltonians for the spin-orbit and spin-spin interactions can be written in the basis of the six states listed above as

$$H_{so} = \lambda_z (|A_1\rangle\langle A_1| + |A_2\rangle\langle A_2| - |E_1\rangle\langle E_1| - |E_2\rangle\langle E_2|) \quad (2.7)$$

$$\begin{aligned} H_{ss} = & \Delta (|A_1\rangle\langle A_1| + |A_2\rangle\langle A_2| + |E_1\rangle\langle E_1| + |E_2\rangle\langle E_2|) \\ & - 2\Delta (|E_x\rangle\langle E_x| + |E_y\rangle\langle E_y|) + \Delta' (|A_2\rangle\langle A_2| - |A_1\rangle\langle A_1|) \\ & + \Delta'' (|E_1\rangle\langle E_y| + |E_y\rangle\langle E_1| - i|E_2\rangle\langle E_x| + i|E_x\rangle\langle E_2|) \end{aligned} \quad (2.8)$$

where  $\lambda_z$  is the axial spin-orbit interaction and  $3\Delta \approx 1.42$  GHz and  $\Delta' \approx 1.55$  GHz characterize the spin-spin induced zero-field splittings [36, 38, 33]. It can be seen that spin-orbit interaction splits states with different total angular momentum, i.e., the pairs  $(A_1, A_2)$ ,  $(E_x, E_y)$  and  $(E_1, E_2)$  are split from each other by about 5.5 GHz [36, 39, 40]. The  $\Delta''$  term leads to non-spin preserving cross transitions, which results to optical pumping of the spin states and plays a role in, for example, limiting the efficiency of spin readout using resonant excitation. The spin-spin interaction also plays a crucial role in the stability of the states  $|A_1\rangle$  and  $|A_2\rangle$ . This interaction shifts up the non-zero spin states  $(A_1, A_2, E_1$  and  $E_2)$  by  $\sim \frac{1}{3}1.42$  GHz [41, 40] and shift the states  $|E_x\rangle$  and  $|E_y\rangle$  down by  $\sim \frac{2}{3}1.42$  GHz. Thus, the gap between  $(A_1, A_2)$  and

$(E_x, E_y)$  is increased, but the gap between the states  $(E_x, E_y)$  and  $(E_1, E_2)$  is reduced. In addition, the spin-spin interaction splits the states  $|A_2\rangle$  and  $|A_1\rangle$  by  $\sim 3.3$  GHz [40]. Thus, for relatively low strain, we obtain a very robust  $|A_2\rangle$  state with stable symmetry properties that are protected by an energy gap arising from the spin-orbit and spin-spin interactions.

We note here that the zero-field splitting in the ground state also arises from the spin-spin interaction, and gives an energy difference of  $\Delta_{gs} \sim 2.88$  GHz between the  $|m_s = 0\rangle$  and  $|m_s = \pm 1\rangle$  states.

## 2.2.2 Properties of optical transitions

Once the wavefunctions are known, it is possible to calculate the selection rules of optical transitions between the triplet excited state and the triplet ground state. The dipole moment between the ground and excited state is produced by the hole left in the  $a$  orbital under optical excitation. As mentioned earlier, the matrix elements  $\langle a | \hat{x} \cdot \vec{r} | e_x \rangle$  and  $\langle a | \hat{y} \cdot \vec{r} | e_y \rangle$  are non-zero, where  $\hat{x}$  and  $\hat{y}$  represent the polarization of the involved photon. We can then calculate the selection rules for transitions between every pair of ground and excited states, as shown in Table 2.1. As expected, these selection rules conserve the total angular momentum of the photon-NV center system.

The allowed optical transitions and their polarization properties indicate several possible  $\Lambda$  schemes in the NV center. However, while these properties are relatively robust in the  $|A_1\rangle$  and  $|A_2\rangle$  states, the  $|A_1\rangle$  state is coupled non-radiatively to a metastable singlet state, which then decays to the ground state  $|0\rangle$ . This results in leakage out of the  $\Lambda$  system consisting of the  $|A_1\rangle$  state and the  $|\pm 1\rangle$  states. Thus, we

Table 2.1: Selection rules for optical transitions between the triplet excited state ( $ae$ ) and the triplet ground state ( $e^2$ ). Linear polarizations are represented by  $\hat{x}$  and  $\hat{y}$ , while circular polarization are represented by  $\hat{\sigma}_{\pm} = \hat{x} \pm i\hat{y}$ . As an example, a photon with  $\sigma_+$  polarization is emitted when the electron decays from state  $A_2$  to state  ${}^3A_{2-}$ .

Pol	$A_1$	$A_2$	$E_1$	$E_2$	$E_x$	$E_y$
${}^3A_{2-}$	$\hat{\sigma}_+$	$\hat{\sigma}_+$	$\hat{\sigma}_-$	$\hat{\sigma}_-$		
${}^3A_{20}$					$\hat{y}$	$\hat{x}$
${}^3A_{2+}$	$\hat{\sigma}_-$	$\hat{\sigma}_-$	$\hat{\sigma}_+$	$\hat{\sigma}_+$		

find that the  $|A_2\rangle$  state provides the an almost ideal closed  $\Lambda$  scheme for experiments such as spin-photon entanglement, as described in Chapter 3. On the other hand, the open  $\Lambda$  system involving  $|A_1\rangle$  can be useful for efficient detection of dark states during coherent population trapping, as shown in Chapter 4.

### 2.2.3 The effect of strain

We now discuss the effect of local strain on the properties of the optical transitions in order to understand variations between different NV centers and deviations from the unperturbed system described above. This perturbation splits the degeneracy between the  $e_x$  and  $e_y$  orbitals and results in their mixing. In the limit of high strain (larger than the spin-orbit splitting), the excited state manifold splits into two triplets, each with a particular well defined spatial wavefunction. Orbital and spin degrees of freedom separate in this regime and spin-preserving transitions are excited by linearly polarized light.

The strain Hamiltonian is given by [38, 33]

$$H_{strain} = \delta_1 (|e_x\rangle\langle e_x| - |e_y\rangle\langle e_y|) + \delta_2 (|e_x\rangle\langle e_y| + |e_y\rangle\langle e_x|) \quad (2.9)$$

where  $\delta_1$  and  $\delta_2$  are different parameters describing the crystal strain. Figure 2.3

shows an example of how  $\delta_1$  strain splits and mixes the excited states, and as a results changes the polarization properties of the optical transitions. A similar effect occurs for  $\delta_2$  strain, where  $|A_2\rangle$  is mixed with  $|E_1\rangle$ . The full Hamiltonian for the excited state manifold of the NV center is then

$$H = H_{ss} + H_{so} + H_{strain}, \quad (2.10)$$

which can be written in the set of basis states  $\{|A_1\rangle, |A_2\rangle, |E_x\rangle, |E_y\rangle, |E_1\rangle, |E_2\rangle\}$  as

$$H = \begin{pmatrix} \Delta - \Delta' + \lambda_z & 0 & 0 & 0 & \delta_1 & -i\delta_2 \\ 0 & \Delta + \Delta' + \lambda_z & 0 & 0 & i\delta_2 & -\delta_1 \\ 0 & 0 & -2\Delta + \delta_1 & \delta_2 & 0 & i\Delta'' \\ 0 & 0 & \delta_2 & -2\Delta - \delta_1 & \Delta'' & 0 \\ \delta_1 & -i\delta_2 & 0 & \Delta'' & \Delta - \lambda_z & 0 \\ i\delta_2 & -\delta_1 & -i\Delta'' & 0 & 0 & \Delta - \lambda_z \end{pmatrix} \quad (2.11)$$

It is worth mentioning that while the excited state configuration is highly affected by strain, the ground state configuration is unaffected to first order due to its anti-symmetric combination of  $e_x$  and  $e_y$  orbitals. It is also protected by the large optical gap between the ground and excited state to second order perturbation in strain.

## 2.3 Experimental techniques

Having developed a theoretical model for the optical transitions of the NV center, we now move on to experimental explorations of these properties. While there are

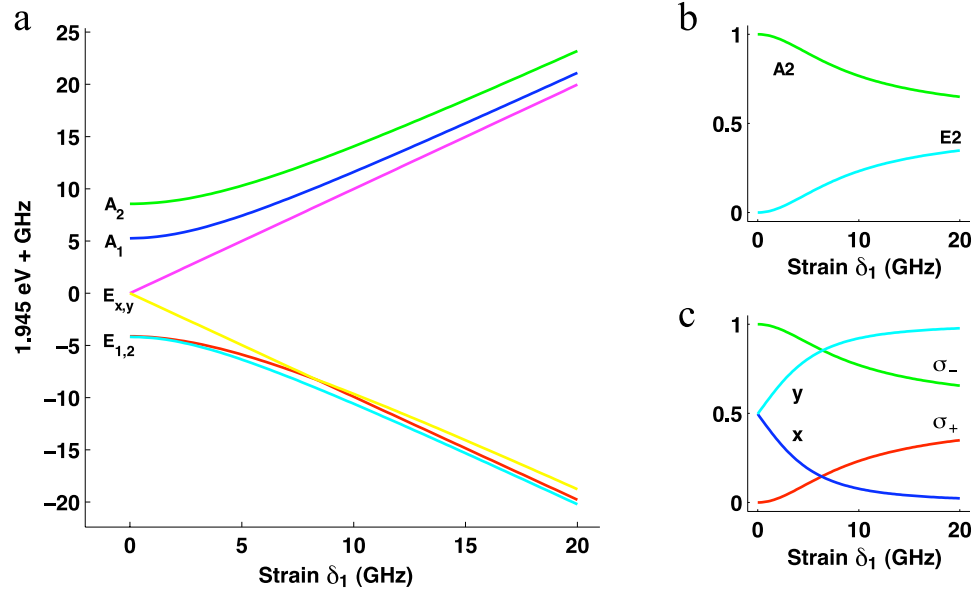


Figure 2.3: Effect of strain on the properties of the NV center. **a.** Energies of the excited states as a function of strain, expressed in units of the linear strain induced splitting between the  $|E_x\rangle$  and  $|E_y\rangle$  states. **b.** Strain induced mixing of the  $|A_2\rangle$  and  $|E_2\rangle$  states, showing the fraction of  $A_2$  and  $E_2$  character of the highest energy excited state. **c.** Polarization character of the optical transition between  $|A_2\rangle$  state and the ground state  $|+1\rangle$  as a function of strain. As strain increases, the polarization changes from circularly to linearly polarized. The transition between  $|A_2\rangle$  and  $|-1\rangle$  shows the same behavior, except with  $\sigma_-$  and  $\sigma_+$  switched. Therefore, at high strain, decay from the  $|A_2\rangle$  results in a separable state of the photon polarization and spin rather than an entangled state.

many available descriptions of setups and procedures for room temperature experiments with NV centers [42, 43], we will focus here on some techniques relevant for low-temperature studies of the optical properties.

### **2.3.1 Diamond materials**

We begin this section with a description of different types of single crystal diamond samples and their differences with regard to NV center properties. The first type of commonly available diamond material is classified as type Ib. In these diamonds, substitutional nitrogen atoms (also called P1 centers) are the dominant defects, which cause the samples to have a yellow color [32]. Type Ib diamonds can occur naturally and are typically grown by the high-pressure-high-temperature (HPHT) method by companies such as Element Six and Sumitomo. Element Six specifies their type Ib diamond as having substitutional nitrogen concentrations of  $<200$  ppm. In our experience, the concentration of NV centers in type Ib samples vary widely through different samples, but NV centers in bulk samples are usually unresolvable under confocal microscopy. There have been no reports of coherent optical transitions from type Ib diamonds, except in one nanocrystal sample where a narrow, but spectrally unstable line was observed under photoluminescence excitation (PLE) spectroscopy [44]. However, as far as we know, this result has never been reproduced. In our experiments, type Ib samples are typically used for developing and fabricating nanophotonic structures, along with studies of NV centers in these structures at room temperature.

The rest of the diamond samples that we typically work with can be classified as type IIa, which is typically defined as having nitrogen impurity concentrations of



less than 1ppm. Type IIa diamonds are rare in nature, but one such sample was found containing a resolvable concentration of single NV centers that show optical linewidths that are close to the lifetime limited linewidth of 13 MHz [45]. Many initial experiments on the optical properties of NV centers were performed on several different pieces of this sample, including the ones in Chapters 3 and 4 of this thesis, along with, for example, [45] and [46]. The unique properties of this sample, and its somewhat murky origins in the Ural mountains, has earned it the name “The Magic Russian Diamond”. The piece used in our experiments is shown in Figure 2.4a, but was accidentally cracked into several smaller pieces some time after the picture was taken. Clearly, such specialized samples cannot be used for wide-scale experiments and development of diamond-based devices. Therefore, we have also worked extensively with synthetic type IIa diamonds grown using microwave assisted chemical vapor deposition (CVD) at Element Six. Standard type IIa grade samples typically also show a unresolvable concentration of NV centers. However, “electronic grade” diamonds developed by Element Six, which are specified to have substitutional nitrogen concentrations of  $<5$  ppb, have NV center concentrations that range from barely resolvable single NVs to less than 1 NV per tens of  $\mu\text{m}^3$ . Native NV centers found in these samples often have linewidths that are broadened by spectral diffusion to several hundred MHz [24, 47, 48]. Nevertheless, they have been used in a variety of experiments involving optical transitions of NV centers [25, 24, 23], and are also excellent starting materials for introducing optically coherent NV centers through ion implantation, as described in Chapter 5.

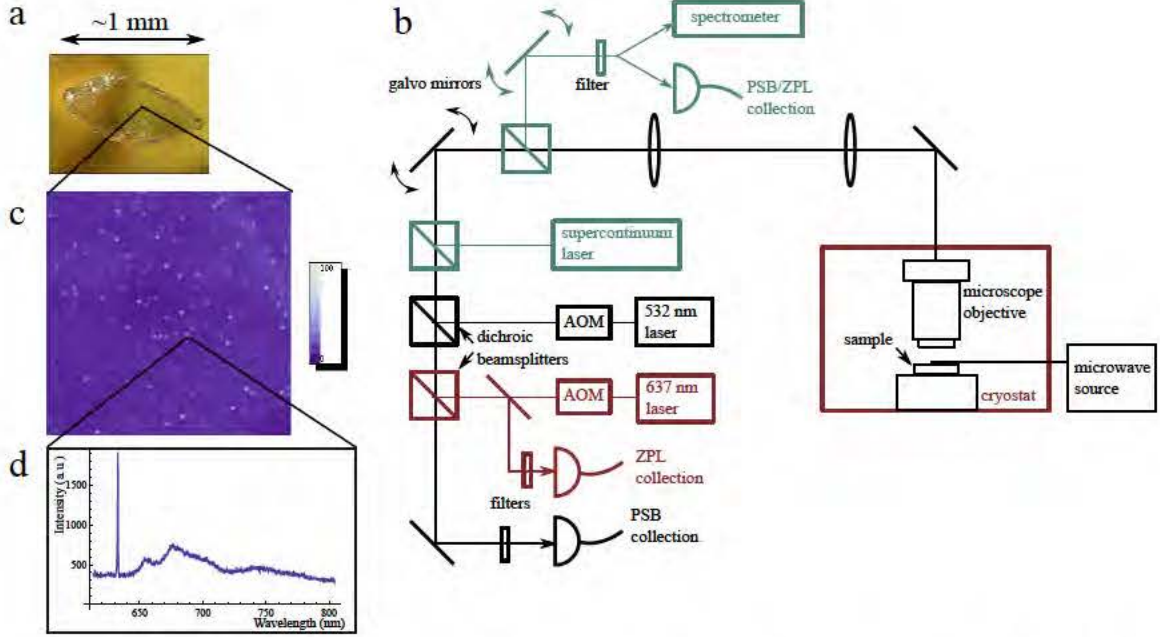


Figure 2.4: Experimental setup and characterization of NV centers. **a.** The type IIa natural diamond sample used for the experiments in Chapters 3 and 4. **b.** Confocal microscope setup. Components in black are needed for a basic room temperature apparatus for investigating the ground state spin physics of the NV center. Red components, such as a cryostat and resonant excitation laser, are additionally needed for low temperature studies of coherent optical properties. A supercontinuum laser is added for characterization of photonic devices such as cavities and waveguides, and an additional, independent collection channel is used for collecting light from a different spatial location than the excitation, as shown in green. In addition, the spectrometer can also be used for photoluminescence studies for the NV center. **c.** Confocal image of single NV centers obtained using 532 nm excitation and PSB collection. **d.** Low temperature photoluminescence spectrum of a NV center. Sharp peak is ZPL at 637 nm.

### 2.3.2 Experimental setup for optical characterization of NV centers

Figure 2.4b shows a schematic of a multi-purpose setup used for optical investigation of NV centers and diamond-based photonic devices. Depending on the type of experiment, only parts of this comprehensive setup are needed. A typical basic confocal microscope for room-temperature studies of NV centers is shown in black. A high numerical aperture (NA) objective is used to focus laser light onto the sample. In order to scan over the sample and locate individual centers in a confocal image such as shown in Figure 2.4c, the diamond is either mounted on a high resolution positioning stage, or the optical path is scanned using a galvo mirror imaged onto the back of the objective with a pair of lenses comprising a 4f imaging system. The vibronic sidebands of the NV center's optically excited states can be addressed using a laser of higher energy than the 637 nm zero-phonon line (ZPL). Typically, this is done using a 532 nm frequency doubled Nd:YAG laser, which is the most common method for controlling the charge state of the NV center. CW 532 nm excitation can ionize both the negatively charged NV center and surrounding charge donors such as substitutional nitrogens, resulting in a equilibrium charge state of the NV center that is  $\sim 70\%$   $\text{NV}^-$  and  $\sim 30\%$   $\text{NV}^0$  [49]. Off resonant excitation is also used in room temperature experiments to polarize the spin of the NV center in to the  $|m_s = 0\rangle$  ground state. This process happens through non-spin preserving transitions from the optically excited state into spin-singlet states of the NV center, which then preferentially decays to the  $|m_s = 0\rangle$  state [39]. Finally, microwave and RF fields for driving spin transitions of the NV centers can be applied with a variety of methods, including

copper wires, coplanar waveguides, and resonator structures.

For low temperature experiments, the diamond sample is placed inside a helium flow cryostat (Janis ST-500) and cooled to  $\sim 4\text{K}$ . Alternative low temperature systems such as closed-cycle pulse tube coolers and bath cryostats can also be used. Diamond samples are typically mounted onto the cold finger, or some intermediate substrate such as a silicon wafer, using indium or silver paste. For resonant excitation of the NV centers, an external cavity diode laser around 637 nm is introduced into the optical path. The New Focus TLB 6304 laser is a popular choice due to its large mode-hop-free scanning range of 60-80 GHz, wavelength tunability over several nanometers, and ease of operation. Both the 532 nm and 637 nm lasers need to be pulsed for most experiments, which can be accomplished using acoustic-optical modulators (AOM) or electro-optical modulators (EOM).

Fluorescence from the NV center is collected through the same optical path, coupled into single-mode fibers, and detected using avalanche photodiodes (APD) or a spectrometer. Filters are placed in the collection path to remove reflected excitation light and separate different parts of the emission spectrum. As shown in Figure 2.4d, the NV center spectrum consists of a broad separate phonon-sideband (PSB) and a sharp ZPL at low temperatures. The percentage of emission into the ZPL is typically 3–5%, which is a major limitation on the efficiency of applications based on coherent photons from the NV center. In Chapter 6, we will address this issue by enhancing the emission into the ZPL using cavity QED with nanophotonic structures. In order to characterize these structures, we use an additional supercontinuum laser as a broadband light source to perform transmission measurements of cavities and waveg-

uities. The light is coupled into one port of the optical device, and the transmitted light must be collected from an output port at a spatially separate location. For this purpose, a second collection channel can be added with its own set of galvo mirrors. In addition, the signal from the two channels can be combined on a time-correlated single photon counting (TCSPC) device for measurements of the second-order autocorrelation function  $g^2(\tau)$  of the emission from individual NV centers to show that they are single-photon emitters [50]. This can also be accomplished by splitting the light collected in a single channel using a fiber beamsplitter.

### 2.3.3 PLE spectroscopy of NV centers

The optical transitions of the NV center can be identified using PLE spectroscopy by scanning the resonant excitation laser across the ZPL and collecting photons in the PSB. Since the  $|0\rangle \rightarrow |E_x\rangle$  and  $|0\rangle \rightarrow |E_y\rangle$  are best the cycling transitions, they are usually the ones observed in PLE spectroscopy in the absence of microwave driving or laser modulation. However, repeated resonant excitation eventually ionizes the  $\text{NV}^-$  or optically pumps the NV center into a different ground state spin sublevel due to the small non-spin conserving cross transitions out of the  $|m_s = 0\rangle$  excited states into the  $|\pm 1\rangle$  ground states [51]. Therefore, some form of charge and spin repumping must eventually be performed. As shown in Figure 2.5b, the first method we use involves scanning the 637 nm laser across the NV transitions and turning on the laser while simultaneously collecting PSB counts for  $\sim 2$  ms at each frequency. At the end of the scan, the 637 nm laser is turned off and a 532 nm repumping pulse is applied. Any duration of repumping longer than a few  $\mu\text{s}$  is sufficient to

reinitialize the NV center. Depending on the charge environment of the NV center and its strain-dependent level structure, however, it may be difficult to obtain good signal from this simple method. For example, in the presence of a large number of other charge traps in the environment, the NV center may be ionized before a sufficient number of photons are scattered on resonance. Another potential issue is that the finite branching ratio of the  $|0\rangle \rightarrow |E_x\rangle$  and  $|0\rangle \rightarrow |E_y\rangle$  transitions into the  $m_s = \pm 1$  states causes a decrease in fluorescence on the timescale of several microseconds. However, fluorescence can potentially still be detected due to off-resonant excitation of transitions from the  $|\pm 1\rangle$  spin states. For example, at high strain, the  $|\pm 1\rangle \rightarrow |A_1\rangle$  transition becomes almost degenerate with the  $|\pm 1\rangle \rightarrow |E_x\rangle$  transition, allowing a steady state fluorescence to be established. However, this may not be the case for all NV centers. More robust methods of obtaining the PLE spectrum without repumping during the scan involve either CW microwave mixing of the  $|0\rangle$  and  $|\pm 1\rangle$ , or modulation of the resonant excitation laser by the ground state zero-field splitting, which also allows the  $|m_s = \pm 1\rangle$  transitions to be observed [51, 52, 53].

Figure 2.5b shows the results of PLE scans taken using this first method. A clear resonance can be seen in each scan, whose frequency then jumps during each successive scan. This is an indication of spectral diffusion, where changes in the local electric field environment of the NV center causes the energies of its excited states to fluctuate over time. As mentioned earlier, from the electronic orbitals  $|e_x\rangle$  and  $|e_y\rangle$  involved in the excited states, one can see that the  $|E_x\rangle$  and  $|E_y\rangle$  states have a permanent electric dipole moment. This dipole moment has been measured to be  $\sim 0.8$  Debye, which

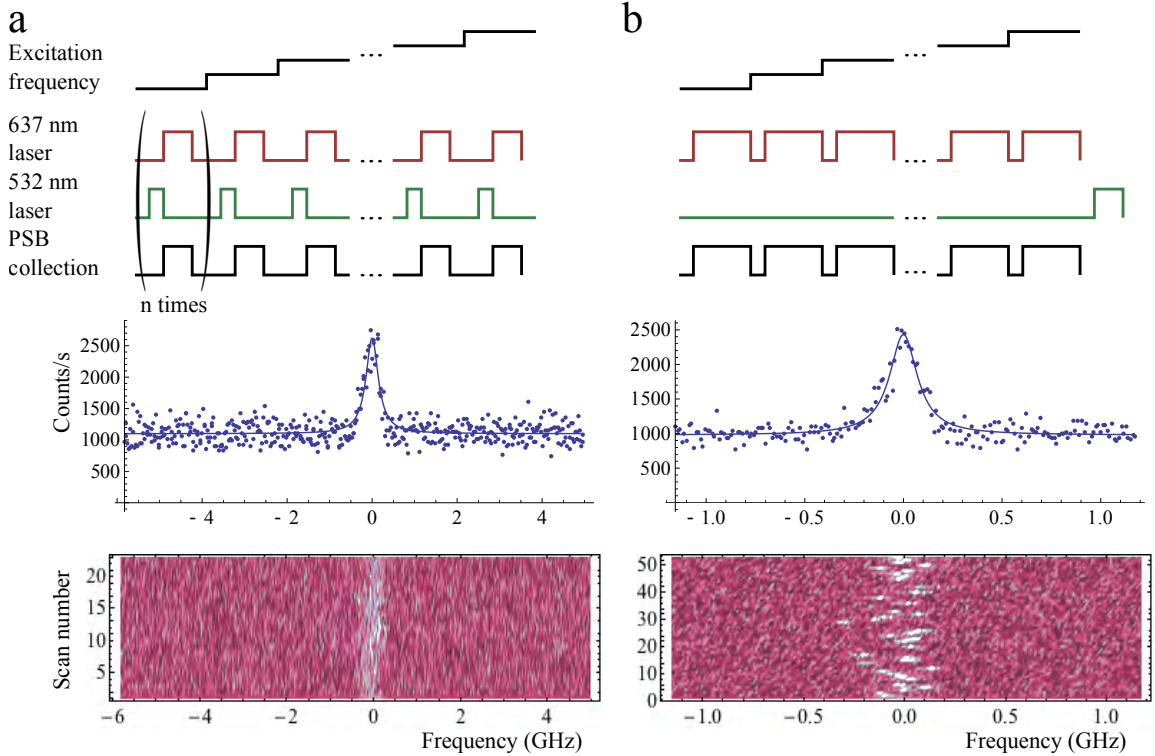


Figure 2.5: Methods for PLE spectroscopy of NV centers. **a.** Pulse sequence for repumping during each PLE scan (top), along with an example showing the result of successive scans (bottom) and the averaged spectrum (middle). **b.** Pulse sequence for repumping at the end of each PLE scan (top), along with corresponding results for the same transition as in a., except zoomed in over a smaller frequency range.

gives rise to energy shifts of  $\sim 4$  GHz/MV/m [33]. It is now well established that 532 nm repumping causes complex charge dynamics in the diamond environment by photoionizing impurities that act as charge donors [54]. Therefore, while very narrow single-scan linewidths can be obtained using this method [44, 45, 52], the long-term, extrinsically broadened linewidth obtained by averaging many such scans can be much broader [24, 47, 48]. This issue is addressed in detail in Chapter 5 of this thesis.

A second method of obtaining the PLE spectrum involves a pulse sequence consisting of a 1  $\mu$ s 532 nm repumping pulse, followed by a 10  $\mu$ s resonant excitation pulse, during which PSB counts are collected. As the 637 nm laser is scanned across the NV transitions, this sequence is repeated many times for each frequency, as illustrated in Figure 2.5a. This method has the advantage that it is robust against ionization and spin polarization, and should in principle give good signal to noise regardless of the charge environment and strain-dependent level structure of the NV center. It also shows the overall lineshape of the transition, including the effects of spectral diffusion, in a single scan. Again, microwave fields are used to obtain a spectrum of all the possible transitions, including those that involve the  $|m_s = \pm 1\rangle$  states.

## 2.4 Studies of the optical properties of NV centers

Figure 2.6a shows a PLE spectrum taken with CW microwave excitation that mixes the ground states during the 637 nm laser pulse. All resonances expected from the direct and cross transitions are observed, as shown in 2.6b, along with some possible microwave-optical two photon transitions.



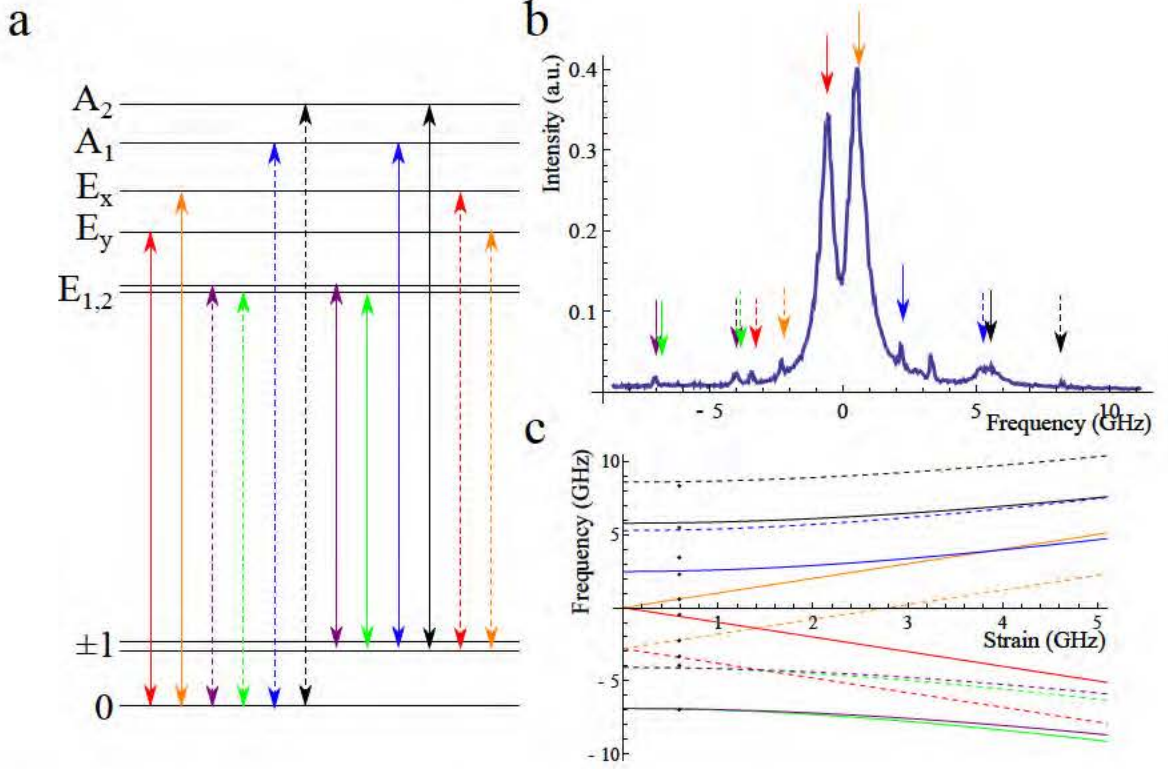


Figure 2.6: Optical transitions of the NV center. **a.** All possible transitions between the ground and excited states, with direct transitions indicated with solid lines, and spin non-conserving cross transitions indicated with dashed lines. **b.** PLE spectrum taken with CW microwave excitation. **c.** Frequencies of all possible transitions shown in **a.** as a function of strain. The frequencies of the peaks in **b.** are matched to a particular strain value (black dots). The extra unidentified peak may be due to a two photon transition from the  $|0\rangle$  state to the  $|E_x\rangle$  state through the absorption of an optical photon and emission of a microwave photon.

### 2.4.1 Optical Rabi oscillations and resonant spin readout

The strongest transitions in 2.6a are the  $|0\rangle \rightarrow |E_x\rangle$  and  $|0\rangle \rightarrow |E_y\rangle$  cycling transitions. Figure 2.7a shows an example of optical Rabi oscillations on the  $|0\rangle \rightarrow |E_y\rangle$  transition, measured by turning on a 40 ns resonant laser pulse a rise time of  $\sim 1$  ns using an EOM (Guided Color Technologies). We then accumulate a histogram of photon arrival times on a TCSPC device with a timing resolution of 195 ps. The photon count rate is proportional to the population in the  $|E_y\rangle$  state, which, in the absence of decay or decoherence, is given by  $P_{E_y}(t) = \sin^2(|\Omega|t)$ , where  $\Omega = \vec{\mu} \cdot \vec{E}/\hbar$  is the Rabi frequency. In this case, however, the oscillations are damped by the finite lifetime of the excited states, which can be measured by fitting to the exponentially decaying tail after the pulse turns off. In addition to population decay, additional decoherence, such as frequency fluctuations of the transition frequency relative to the laser frequency caused by, for example, spectral diffusion, will also contribute to the damping of Rabi oscillations. We note here, however, that this additional dephasing alone does not give a good estimate of the spectral diffusion of the NV center, unlike what is claimed in [46]. For example, if the transition frequency jumps well outside of the power-broadened linewidth of the transition, then the NV center will effectively not be excited, and there will simply be no contribution to the Rabi oscillation data.

By measuring Rabi oscillations, we can determine the length of laser pulse needed to, for example, perform an optical  $\pi$  pulse to transfer population to the  $|A_2\rangle$  state for entanglement generation, as described in Chapter 3. Note that, while optical Rabi oscillations can also be observed between the  $|m_s = \pm 1\rangle$  ground and excited states, the dynamics are more complicated due to the fact that these are  $\Lambda$ -type

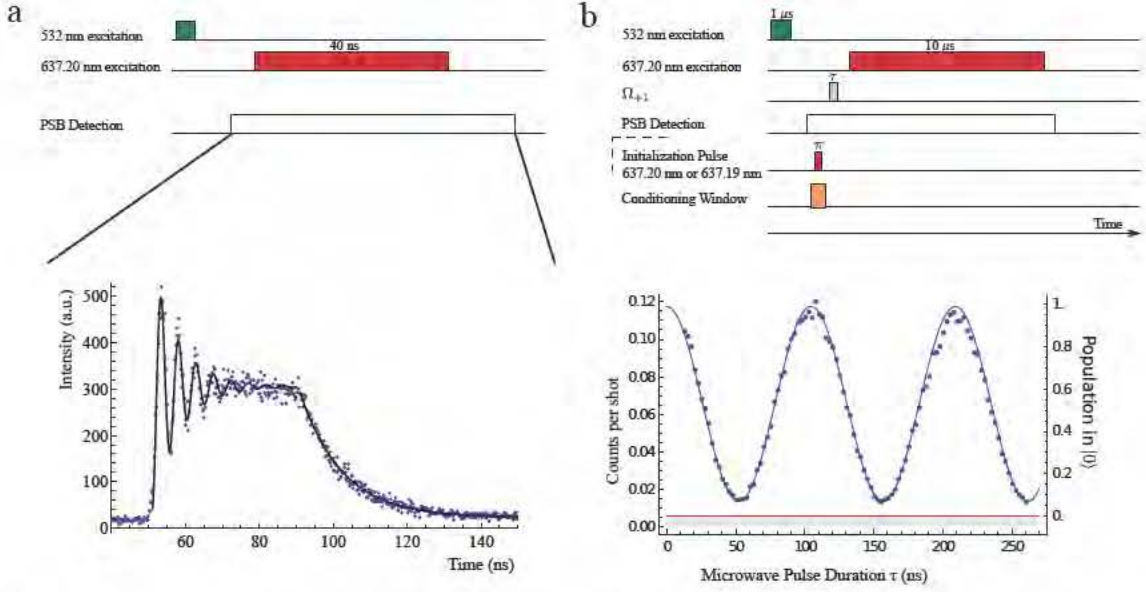


Figure 2.7: a. Optical Rabi oscillations detected using PSB fluorescence and resonant excitation, along with corresponding pulse sequence. The 637.2 nm laser is tuned to the  $|0\rangle \rightarrow |E_y\rangle$  transition and is on from 50 ns to 90 ns. b. Rabi oscillations between  $|0\rangle$  and  $|+1\rangle$  (blue) detected using resonant spin readout and corresponding pulse sequence. Red lines are calibration levels for the  $|0\rangle$  and  $|+1\rangle$  states. To initialize the spin states for this calibration, we use a measurement-based technique where the  $|0\rangle$  is prepared conditioned on the detection of a PSB photon after excitation to the  $|E_y\rangle$  state. To prepare the  $|+1\rangle$  state, we then apply a microwave  $\pi$  pulse before readout. More details are available in section A.3

transitions. In the absence of a magnetic field, instead of settling to a steady state value corresponding to 50% population in the excited state, the photon count rate continually decreases after a few optical cycles as population is pumped into a "dark" ground state that is not excited by the laser. However, the observed Rabi oscillations are usually sufficient for determining the optical  $\pi$  pulse length.

The cycling transitions of the NV center can also be used to efficiently read out the spin state of the NV center. As shown in Figure 2.7, when a resonant laser pulse is turned on for 10  $\mu$ s, the number of photons scattered is proportional to the population in the  $|m_s = 0\rangle$  states, and microwave-driven Rabi oscillations between the  $|0\rangle$  and  $|+1\rangle$  ground state sublevels can be observed. A detailed description of the resonant spin-readout procedure used in Chapter 3 can be found in section A.3. The efficiency and fidelity of this spin readout method is limited by the photon collection efficiency, the temperature, and the branching ratio out of the  $|m_s = 0\rangle$  manifold. As can be predicted by the Hamiltonian given in Equation 2.2.3, this branching ratio depends on the local strain. In our first experiments, the spin readout contrast was limited to  $c_M = 0.11 \pm 0.0022$  counts/shot when the spin was prepared in the  $|0\rangle$  state and a background-limited  $c_B = 0.0057 \pm 0.0010$  counts/shot when the spin was prepared in the  $|\pm 1\rangle$  states. Therefore, to determine the spin of the NV center, the state had to be prepared and read-out many times to obtain an average number of counts per shot  $C$ , which then allows us to calculate the population in the  $|0\rangle$  state as  $P = (C - c_B) / (c_M - c_B)$ . By increasing the collection efficiency with a solid immersion lens and working with low strain NV centers, single shot resonant readout of the spin state has subsequently been demonstrated [55].

### 2.4.2 Multi-level systems and all-optical spin manipulation

While the previous section mostly focused on cycling optical transitions, the NV center's level structure enables us to explore and make use of more complex dynamics beyond that of a two-level system. For example, Chapter 4 makes use of the  $\Lambda$ -type system between the  $|\pm 1\rangle$  ground states and the  $|A_1\rangle$  or  $|A_2\rangle$  excited state to perform coherent population trapping (CPT). A single linearly polarized laser field was used to simultaneously drive the  $\sigma^+$  and  $\sigma^-$  polarized transitions. In this case, for the  $|A_2\rangle$  system, the Hamiltonian in the rotating frame is given by

$$H = \Delta |A_2\rangle \langle A_2| - \frac{\delta}{2} |-1\rangle \langle -1| + \frac{\delta}{2} |+1\rangle \langle +1| \quad (2.12)$$

$$- \Omega_+ |A_2\rangle \langle +1| + \Omega_- |A_2\rangle \langle -1| - \Omega_+^* |+1\rangle \langle A_2| + \Omega_-^* |-1\rangle \langle A_2|, \quad (2.13)$$

where  $\Delta$  is the one-photon detuning and  $\delta$  is the two photon detuning corresponding to the Zeeman splitting between the  $|\pm 1\rangle$  states. From this Hamiltonian it can be seen that the dark state

$$|D\rangle = \frac{\Omega_- |+1\rangle + \Omega_+ |-1\rangle}{\sqrt{|\Omega_-|^2 + |\Omega_+|^2}} \quad (2.14)$$

is perfectly decoupled from the excited state when  $\delta = 0$ . Since  $\delta$  is given by the sum of the externally applied magnetic field and the Overhauser field from the nuclear spin bath, we can determine the nuclear spin configuration by finding the external field for which the NV fluorescence is suppressed, indicating that the system is trapped in the dark state. This is the idea behind the work presented in Chapter 4.

Based on this description of multi-level dynamics, we now describe several experiments to manipulate the spin of the NV center by all-optical means. Even though methods for microwave manipulation of the spin states are well established, all-optical

spin manipulation is useful in potentially allowing more flexibility in the transitions addressed and achieving faster operations, especially in applications where the geometry does not allow easy access with high power microwave fields. For example, in photonic devices where light fields are well coupled to the NV center and are already being used as the signal, it would be desirable use all-optical means to control and initialize the device as well and eliminate the need for fabricating additional structures for microwave delivery.

As a first example of all-optical spin manipulation, we demonstrate two-photon Rabi oscillations between the  $|\pm 1\rangle$  states mediated by the  $|A_2\rangle$  state. We explore the case where there is no externally applied magnetic field so that the  $|\pm 1\rangle$  states are mostly degenerate except for hyperfine couplings with nuclear spins. This is one situation where all-optical spin manipulation is advantageous. Without a Zeeman splitting, is difficult to selectively address a well-defined combination of the  $|\pm 1\rangle$  states with microwaves, since the polarization of microwave fields are much more difficult to control than the laser polarization.

Again, we use a single linearly polarized laser to address both branches of the three level system, now far detuned from the  $|\pm 1\rangle \rightarrow |A_2\rangle$  transition, i.e.  $\Delta$  is large and  $\delta = 0$ . In this case, the system behaves as if the  $|\pm 1\rangle$  states are coupled by an effective two-photon Rabi frequency  $\Omega' = \Omega_+^* \Omega_- / \Delta$ . In the limit that the detuning  $\Delta$  is large enough so that

$$\frac{\Omega_+^2}{\Delta^2} \gamma, \frac{\Omega_-^2}{\Delta^2} \gamma \ll \Omega', \quad (2.15)$$

where  $\gamma$  is the lifetime of the excited state, one should be able to observe Rabi oscillations between the  $|\pm 1\rangle$  states.

Lacking the ability to selectively transfer population between  $|\pm 1\rangle$  and  $|0\rangle$  with microwaves and perform conventional resonant spin readout, we must be able to both prepare and directly read out the population in the  $|+1\rangle$  or  $|-1\rangle$  states all-optically to observe the spin dynamics. State preparation can be achieved by optical pumping. For example, to prepare the  $|-1\rangle$  state, we first apply a laser pulse for 20  $\mu\text{s}$  on the  $|0\rangle \rightarrow |E_x\rangle$  transition. This optically pumps the spin states in to  $|\pm 1\rangle$ . We then apply a  $\sigma_-$  polarized laser to selectively excite the  $|+1\rangle \rightarrow |A_2\rangle$  transition for 400 ns. Using this method, a spin polarization of  $\sim 80\%$  in the  $|-1\rangle$  state was achieved. The effectiveness of this method is limited by off-resonant excitation of the  $|\pm 1\rangle$  during the first pumping step, and imperfect state selection during the second step. In addition, the long optical pumping step can result in ionization of the NV center. It should be possible to improve spin polarization by optimizing the power and duration of the  $|0\rangle \rightarrow |E_x\rangle$  pulse, and by better controlling the polarization of the  $|+1\rangle \rightarrow |A_2\rangle$  laser.

In the low strain limit, unlike the  $|m_s = 0\rangle$  transitions, the transitions involving the  $|m_s = \pm 1\rangle$  states are not cycling. Therefore, we read out the spin state by applying a  $\pi$  pulse to the  $|A_2\rangle$  state and collecting the emitted photons. We can choose the particular superposition of  $|+1\rangle$  and  $|-1\rangle$  by choosing the polarization of the readout laser. To separately characterize the effectiveness of this method, we first apply a magnetic field and use this technique to detect microwave-driven transitions between  $|+1\rangle$  and  $|0\rangle$ . Figure 2.8 shows a comparison of the two methods for reading out the  $|+1\rangle$  and  $|0\rangle$  populations, along with the associated level scheme and pulse sequences. As expected, the oscillations are  $\pi$  out of phase from each other. While the laser power and duration was not optimized for the  $|0\rangle \rightarrow |E_x\rangle$  data, we see that the  $|+1\rangle \rightarrow |A_2\rangle$



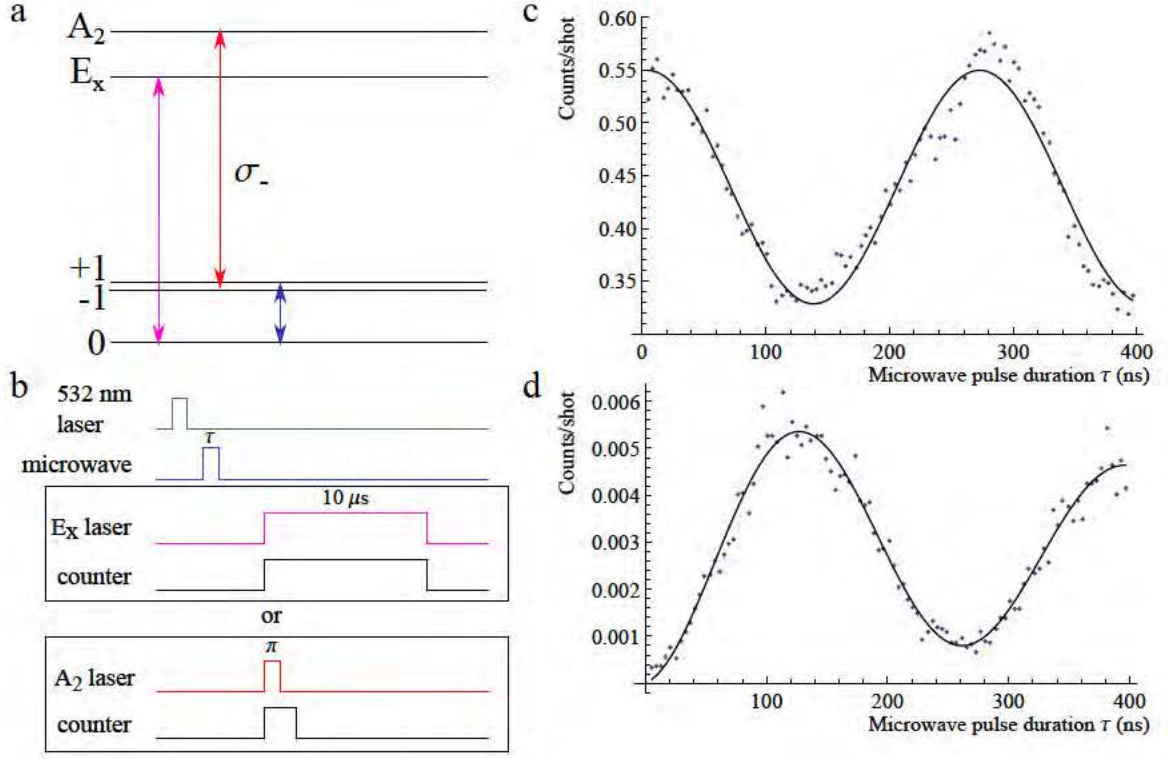


Figure 2.8: Readout of  $|-1\rangle$  spin state population. **a.** Level structure showing laser excitation and microwave field. An external field was applied here so that the microwaves are state-selective. However, the Zeeman splitting is not resolvable with the  $|+1\rangle \rightarrow |A_2\rangle$ , so state selectivity is ensured by using making the laser  $\sigma_-$  polarized. **b.** Pulse sequence showing two alternative readout schemes. **c.** Ground state Rabi oscillations detected using conventional spin readout with  $|0\rangle \rightarrow |E_x\rangle$  transition. **d.** Ground state Rabi oscillations detected using  $|+1\rangle \rightarrow |A_2\rangle$  transition.

readout results in better contrast, but much fewer counts.

We now remove the external magnetic field and combine the spin polarization and readout techniques above to demonstrate two-photon Rabi oscillations, as shown in Figure 2.9. First, the NV center is optically pumped into the  $|-1\rangle$  state as described above. Using an EOM, we then apply a linearly polarized laser pulse of varying duration that is detuned 2.24 GHz from the  $|\pm 1\rangle \rightarrow |A_2\rangle$  transition. The population in the  $|+1\rangle$  state is then read out with the same laser as the one used for  $|+1\rangle$  to  $|-1\rangle$



optical pumping. As a reference, we again read out the  $|+1\rangle$  state after applying only the  $|0\rangle \rightarrow |E_x\rangle$  optical pumping step, which should prepare the spin state in an equal superposition of  $|+1\rangle$  and  $|-1\rangle$ . We normalize the counts obtained during the readout after two-photon Rabi to the counts obtained during readout after the reference sequence. As can be seen in Figure 2.9c, we observe oscillations of the  $|+1\rangle$  state population that eventually decays to a steady state value of 1 relative to the reference, which corresponds to 50% population. The two-photon Rabi frequency follows a linear dependence in the laser power, as expected (Figure 2.9)d. We estimate the expected two-photon Rabi frequencies by directly measuring the Rabi frequencies on either the  $|0\rangle \rightarrow |E_x\rangle$  or  $|+1\rangle \rightarrow |A_2\rangle$  transition. We also take into account the fact that the  $|\pm 1\rangle \rightarrow |A_1\rangle$  is close by, with an additional detuning of 3.2 GHz. Since the  $|A_1\rangle$  state has the opposite relative phase as the  $|A_2\rangle$  state between the  $|\pm 1\rangle$  spin components, we expect that  $\Omega_+(A_2) = -\Omega_+(A_1)$ . Therefore, the two-photon Rabi frequency is given by

$$\Omega' = \frac{\Omega_+\Omega_-}{\Delta_2} - \frac{\Omega_+\Omega_-}{\Delta_1} \quad (2.16)$$

where  $\Delta_{1,2}$  are the detunings from the  $|A_{1,2}\rangle$  states, respectively.

The decay of the oscillations is due to off-resonant excitation of the excited states. The decay rate is given by the total population in the excited states multiplied by their decoherence rate, which we estimate to be  $\Gamma \sim 100$  MHz including the effect of spontaneous decay, spectral diffusion, and laser frequency fluctuations. Therefore, we estimate the effective decay rate to be

$$\Gamma' = \left( \frac{\Omega_+^2}{\Delta_2^2} + \frac{\Omega_-^2}{\Delta_2^2} + \frac{\Omega_+^2}{\Delta_1^2} + \frac{\Omega_-^2}{\Delta_1^2} \right) \Gamma. \quad (2.17)$$

We again plot this quantity using the two estimates of the Rabi frequency in Figure

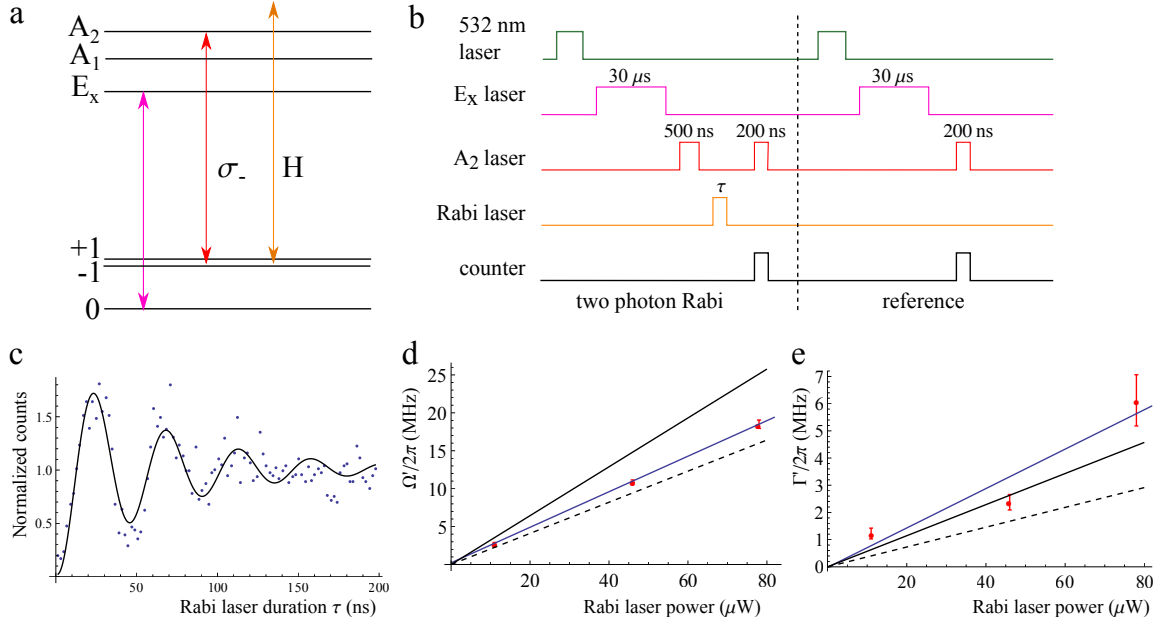


Figure 2.9: Two-photon Rabi oscillations between the  $|\pm 1\rangle$  ground states. **a.** Level structure showing the transitions involved. One laser is used for optical pumping from  $|0\rangle$  state (magenta). Another  $\sigma_-$  polarized laser is used for optical pumping and spin readout from  $|+1\rangle$  state (red). A third, linearly polarized laser is used for driving the two-photon transition (orange). **b.** Pulse sequence showing spin preparation, manipulation, and readout steps. An additional set of pulses provide a reference for eliminating the effects of count rate fluctuations due to spatial drift of the NV center and laser frequency fluctuations. **c.** Two-photon Rabi oscillations with 46  $\mu\text{W}$  of laser power. **d.** Two-photon Rabi frequency as a function of laser power, with linear fit (blue line) and estimates based on Rabi frequencies of the  $|0\rangle \rightarrow |E_x\rangle$  (black, solid line) or  $|+1\rangle \rightarrow |A_2\rangle$  transition (black, dashed line). **e.** Decay rate of two-photon Rabi oscillations as a function of laser power, with fit and estimates as in d.

2.9e.

In order to achieve full all-optical control of the spin states, we also require a method of coherently transferring population between the  $|0\rangle$  and  $|\pm 1\rangle$  states. This requires the use of non-spin preserving cross transitions between the ground and excited states. Cross transitions involving the lower branch of the excited state levels under high strain were previously used in CPT experiments [53]. We choose to instead

use the tripod system formed between the  $|A_2\rangle$  excited state and all three ground state levels in the same low-strain NV center as above. In principle, such a system would allow for selective coherent operations between  $|0\rangle$  and either  $|+1\rangle$  or  $|-1\rangle$  even at zero magnetic field, since the two branches of the  $\Lambda$  subsystem between  $|A_2\rangle$  and  $|\pm 1\rangle$  have orthogonal circular polarizations. This is not the case for high strain NV centers. Here, we present an initial characterization of the tripod system. To do this, we scan a single linearly polarized laser across the  $|0\rangle \rightarrow |A_2\rangle$  transition and modulate the same laser using an EOM to create sidebands for addressing the  $|\pm 1\rangle \rightarrow |A_2\rangle$  transition. In this case, the Hamiltonian of the system is given by

$$\begin{aligned}
H = & -\Delta|0\rangle\langle 0| - (\Delta' + \frac{\delta}{2})|+1\rangle\langle +1| - (\Delta' - \frac{\delta}{2})|-1\rangle\langle -1| \\
& -(\Omega_0|A_2\rangle\langle 0| + \Omega_+|A_2\rangle\langle +| + \Omega_-|A_2\rangle\langle -| + c.c.). \tag{2.18}
\end{aligned}$$

Here, as illustrated in Figure 2.10a,  $\Delta$  is the one photon detuning of the carrier laser frequency,  $\delta$  is the Zeeman splitting between the  $|\pm 1\rangle$  states, and  $\Delta' = \Delta - \Delta_{ZFS} + \omega_{mod}$ , where  $\Delta_{ZFS} = 2.88$  GHz is the ground state zero field splitting and  $\omega_{mod}$  is the laser modulation frequency. In the experiment, we perform the usual PLE spectroscopy with a 50  $\mu$ s resonant excitation pulse and collect PSB photons during that interval. In addition, during each successive scan, we change the modulation frequency such that the sideband sweeps through the  $|\pm 1\rangle \rightarrow |A_2\rangle$  transition. An external magnetic field was applied to split the  $|\pm 1\rangle$  states by 18 MHz. As can be seen in Figure 2.10c, when the sideband is far detuned from the  $|\pm 1\rangle \rightarrow |A_2\rangle$  transitions, we simply obtain a resonance corresponding to the  $|0\rangle \rightarrow |A_2\rangle$  cross transition. When the modulation frequency is such that the  $\Lambda$  systems involving the  $|0\rangle$  and  $|+1\rangle$  or  $|0\rangle$  and  $|-1\rangle$  states are in two-photon resonance, we see a decrease in fluorescence

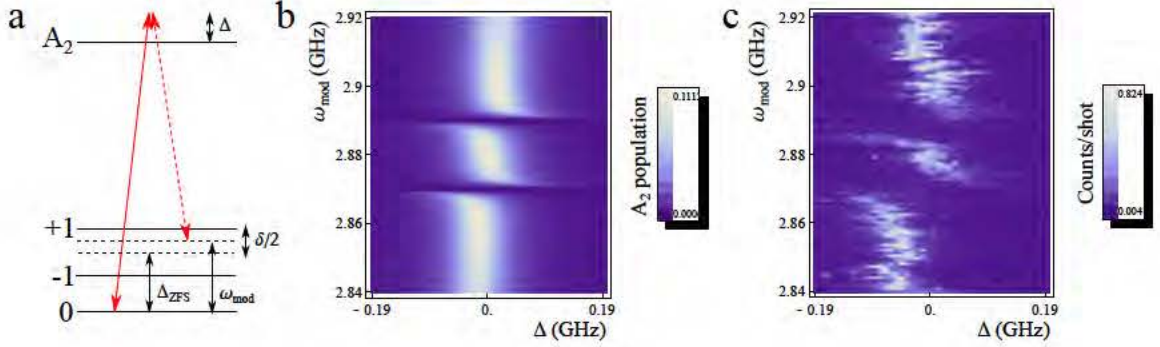


Figure 2.10: Spectroscopy of the  $|A_2\rangle$  state tripod system. **a.** Level structure. **b.** Theoretical excited state population as a function of one-photon detuning and modulation frequency. **c.** Experimental data showing PSB fluorescence during laser excitation as a function of one-photon detuning and modulation frequency.

indicative of population becoming trapped in a dark state. We can model this system including the effects of excited state decay using a full master equation approach. The results are shown in Figure 2.10b, and agree qualitatively with the experimental data.

The four-level system investigated here can be used for transferring population between the  $|0\rangle$  and  $|\pm 1\rangle$  states using, for example, two-photon Rabi or stimulated Raman adiabatic passage (STIRAP) techniques. In addition, there have been proposals for using tripod systems for performing robust geometric gates between two of the ground state levels for quantum computation applications [56, 57].

## Chapter 3

# Quantum entanglement between an optical photon and a solid-state spin qubit

### 3.1 Introduction

A quantum network [6] consists of several nodes, each containing a long-lived quantum memory and a small quantum processor, that are connected via entanglement. Its potential applications include long-distance quantum communication and distributed quantum computation [58]. Several recent experiments demonstrated on-chip entanglement of solid-state qubits separated by nanometer [59] to millimeter [60, 61] length scales. However, realization of long-distance entanglement based on solid-state systems coupled to single optical photons [62] is an outstanding challenge. The nitrogen-vacancy (NV) center, a defect in diamond consisting of a substitutional

*Chapter 3: Quantum entanglement between an optical photon and a solid-state spin qubit*

---

nitrogen atom and an adjacent vacancy, is a promising candidate for implementing a quantum node. The ground state of the negatively charged NV center is an electronic spin triplet with a 2.88 GHz zero-field splitting between the  $|m_s = 0\rangle$  and  $|m_s = \pm 1\rangle$  states (from here on denoted  $|0\rangle$  and  $|\pm 1\rangle$ ). With long coherence times [63], fast microwave manipulation, and optical preparation and detection [64], the NV electronic spin presents a promising qubit candidate. Moreover, it can be coupled to nearby nuclear spins that provide exceptional quantum memories and allows for the robust implementation of few-qubit quantum registers [59, 65]. In this work we demonstrate the preparation of quantum entangled states between a single photon and the electronic spin of a NV center:

$$|\Psi\rangle = \frac{1}{\sqrt{2}}(|\sigma_-\rangle|+1\rangle + |\sigma_+\rangle|-1\rangle), \quad (3.1)$$

where  $|\sigma_+\rangle$  and  $|\sigma_-\rangle$  are orthogonal circularly polarized single photon states.

The key idea of our experiment is illustrated in Figure 3.1a. The NV center is prepared in a specific excited state ( $|A_2\rangle$  in Fig 3.1a) that decays with equal probability into two different long lived spin states ( $|\pm 1\rangle$ ) by the emission of orthogonally polarized optical photons at 637 nm. The entangled state given by Eq. 3.1 is created because photon polarization is uniquely correlated with the final spin state. This entanglement is verified by spin state measurement using a cycling optical transition following the detection of a 637 nm photon of chosen polarization.



*Chapter 3: Quantum entanglement between an optical photon and a solid-state spin qubit*

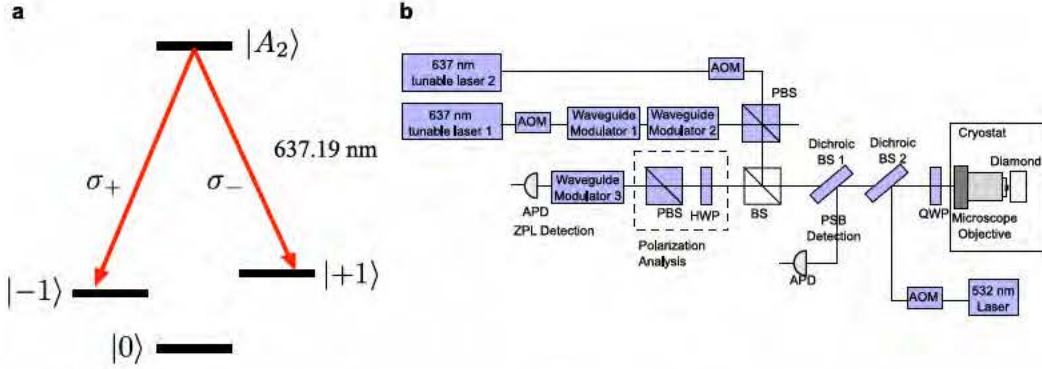


Figure 3.1: Scheme for spin-photon entanglement. **a.** Following selective excitation to the  $|A_2\rangle$  state, the  $\Lambda$  system decays to two different spin states through the emission of orthogonally polarized photons, resulting in spin-photon entanglement. **b.** Schematic of the optical setup. Individual NV centers are isolated and addressed optically using a microscope objective. Two resonant lasers at 637 nm and an off resonant laser at 532 nm address various optical transitions. Fluorescence emitted from the NV center is spectrally separated into PSB and ZPL channels, and are detected with APDs. The latter channel contains entangled photons and is sent through a polarization analysis stage.

## 3.2 Characterization of NV centers

Understanding and controlling excited state properties is a central challenge for achieving such a coherent interface between spin memory and optical photons. In contrast to isolated atoms and ions, solid state systems possess complex excited state properties that depend sensitively on their local environment [51]. Non-axial crystal strain is particularly important to the present realization because it affects the optical transitions' selection rules and polarization properties [39].

In the absence of external strain and electric or magnetic fields, properties of the six electronic excited states are determined by the NV center's  $C_{3V}$  symmetry and spin-orbit and spin-spin interactions (shown in Figure 3.2a) [39]. Optical transitions between the ground and excited states are spin preserving, but could change electronic

*Chapter 3: Quantum entanglement between an optical photon and a solid-state spin qubit*

---

orbital angular momentum depending on the photon polarization. Two of the excited states, labeled  $|E_x\rangle$  and  $|E_y\rangle$  according to their orbital symmetry, correspond to the  $m_s = 0$  spin projection. Therefore they couple only to the  $|0\rangle$  ground state and provide good cycling transitions, suitable for readout of the  $|0\rangle$  state population through fluorescence detection. The other four excited states are entangled states of spin and orbital angular momentum. Specifically, the  $|A_2\rangle$  state has the form

$$|A_2\rangle = \frac{1}{\sqrt{2}}(|E_- \rangle | +1 \rangle + |E_+ \rangle | -1 \rangle), \quad (3.2)$$

where  $|E_{\pm}\rangle$  are orbital states with angular momentum projection  $\pm 1$  along the NV axis. At the same time, the ground states ( $|0\rangle$ ,  $|\pm 1\rangle$ ) are associated with the orbital state  $|E_0\rangle$  with zero projection of angular momentum (for simplicity the spatial part of the wavefunction is not explicitly written). Hence, due to total angular momentum conservation, the  $|A_2\rangle$  state decays with equal probability to the  $|-1\rangle$  ground state through  $\sigma_+$  polarized radiation and to  $|+1\rangle$  through  $\sigma_-$  polarized radiation.

The inevitable presence of a small strain field, characterized by the strain splitting ( $\Delta_s$ ) of  $|E_{x,y}\rangle$ , reduces the NV center's symmetry and shifts the energies of the excited state levels according to their orbital wavefunctions. For moderate and high strain, the excited states are separated into two branches and there is mixing between levels [53]. In the upper branch, an energy gap protects  $|A_2\rangle$  against low strain and magnetic fields, preserving the polarization properties of its optical transitions. A group theoretical analysis of the excited states and polarization properties of the transitions are provided in Section 2.2.

To ensure that  $|E_y\rangle$  is a good cycling transition and  $|A_2\rangle$  acts as an entanglement generation transition as required for the current study, we select a NV center with



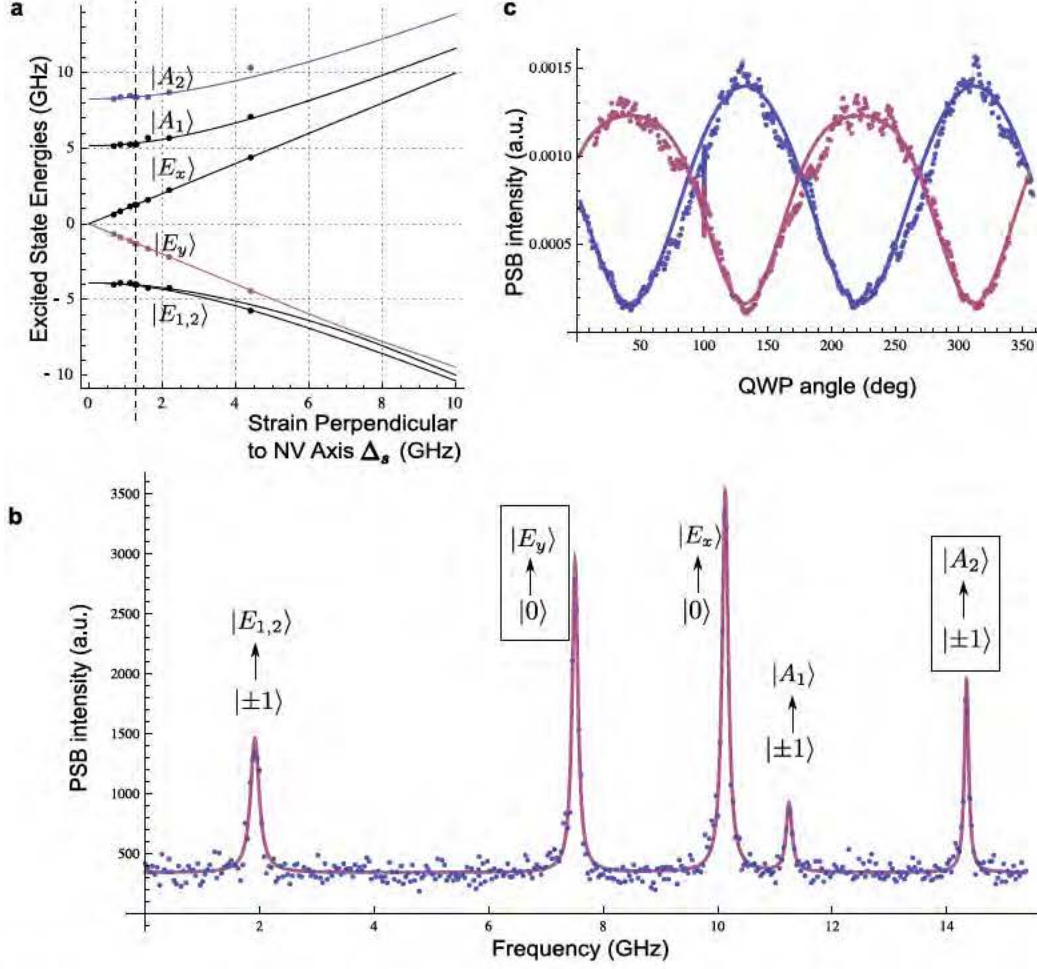


Figure 3.2: Characterization of NV centers. **a.** Energy levels of the NV center under strain. Solid lines are based on a theoretical model from [51] and dots are data from seven NV centers. The dashed line indicates the NV center used in this paper. **b.** Excitation spectrum of the NV center under CW microwave radiation. **c.** Polarization properties of the  $|\pm 1\rangle \rightarrow |A_2\rangle$  transition in absorption. The system is initially prepared in  $|+1\rangle$  (blue) or  $|-1\rangle$  (red). We then apply a laser pulse of varying polarization to the  $|A_2\rangle$  state while collecting fluorescence. Oscillations with visibility  $77 \pm 10\%$  indicate that the transitions linking  $|\pm 1\rangle$  to  $|A_2\rangle$  are circularly polarized and mutually orthogonal (see Section A.4 for details).

relatively small strain splitting ( $\Delta_s \sim 2 \times 1.28$  GHz). Figure 3.2b presents its excitation spectrum, while Figure 3.2c demonstrates the desired polarization properties of the  $|\pm 1\rangle \leftrightarrow |A_2\rangle$  transitions via resonant excitation.

### 3.3 Experimental demonstration of spin-photon entanglement

We now turn to the experimental demonstration of spin-photon entanglement. Our experimental setup is outlined in Figure 3.1b and described in Section A.2. To create the entangled state, we use coherent emission within the narrow-band zero phonon line (ZPL), which consists of only 4% of the NV center’s total emission. The remaining optical radiation occurs in the frequency shifted phonon side band (PSB), which is accompanied by phonon emission that deteriorates the spin-photon entanglement [66]. Isolating the weak ZPL emission presents a significant experimental challenge due to strong reflections of the resonant excitation pulse reaching the detector. By exciting the NV center with a circularly polarized 2 ns  $\pi$  pulse that is shorter than the emission timescale, we can use detection timing to separate reflection from fluorescence photons. A combination of confocal rejection, modulators, and finite transmittivity of our optics suppresses the reflections sufficiently to clearly detect the NV center’s ZPL emission in a 20 ns region (Figure 3.3).

For photon state determination, ZPL photons in either the  $|\sigma_{\pm}\rangle$  or  $|H\rangle = \frac{1}{\sqrt{2}}(|\sigma_{+}\rangle + |\sigma_{-}\rangle)$ ,  $|V\rangle = \frac{1}{\sqrt{2}}(|\sigma_{+}\rangle - |\sigma_{-}\rangle)$  basis are selected by a polarization analysis stage and detected after an optical path of  $\sim 2$  m. Spin readout then occurs after a 0.5  $\mu$ s spin

*Chapter 3: Quantum entanglement between an optical photon and a solid-state spin qubit*

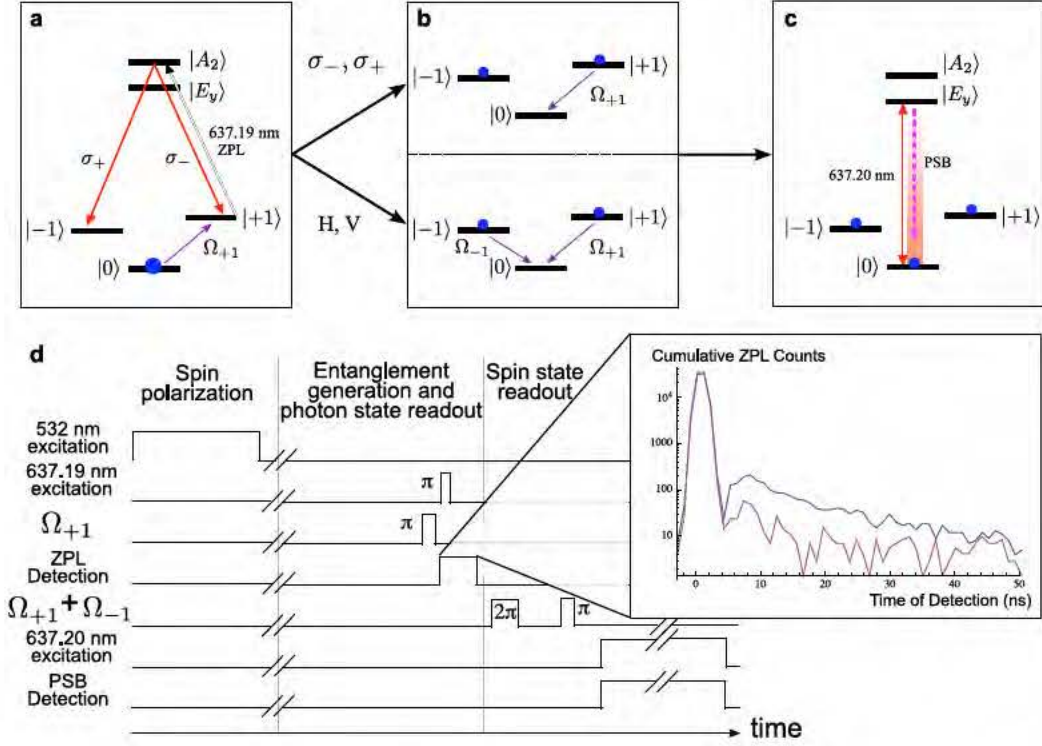


Figure 3.3: Experimental procedure for entanglement generation. **a.** After spin polarization into  $|0\rangle$ , population is transferred to  $|+1\rangle$  by a microwave  $\pi$  pulse ( $\Omega_{+1}$ ). The NV is excited to  $|A_2\rangle$  with a 637.19 nm  $\pi$  pulse and the ZPL emission is collected. **b.** If a  $\sigma_+$  or  $\sigma_-$  photon is detected, the population in  $|+1\rangle$  or  $| -1\rangle$  is transferred to  $|0\rangle$ . If a  $|H\rangle$  or  $|V\rangle$  photon is detected, a  $\tau - 2\pi - \tau$  echo sequence (see Section A.5) is applied with  $\Omega_{+1}$  and  $\Omega_{-1}$ , followed by a  $\pi$  pulse which transfers the population in  $|M\rangle$  (see text) to  $|0\rangle$ . **c.** The population in  $|0\rangle$  is measured using the 637.20 nm optical readout transition. **d.** Pulse sequence for the case where a  $|H\rangle$  or  $|V\rangle$  ZPL photon is detected (time axis not to scale). If a  $\sigma_{\pm}$  photon is detected instead, only a  $\pi$  pulse on either  $\Omega_{+1}$  or  $\Omega_{-1}$  is used for spin readout. Inset: Detection time of ZPL channel photons showing reflection from diamond surface and subsequent NV emission (blue) and background counts (purple).

*Chapter 3: Quantum entanglement between an optical photon and a solid-state spin qubit*

---

memory interval following photon detection by transferring population from either the  $|\pm 1\rangle$  states or from their appropriately chosen superposition into the  $|0\rangle$  state using microwave pulses  $\Omega_{\pm 1}$ . The pulses selectively address the  $|0\rangle \leftrightarrow |\pm 1\rangle$  transitions with resonant frequencies  $\omega_{\pm}$  that differ by  $\delta\omega = \omega_+ - \omega_- = 122$  MHz due to an applied magnetic field. For superpositions of  $|\pm 1\rangle$  states an echo sequence is applied before the state transfer to extend the spin coherence time (see Section A.5). The transfer is followed by resonant excitation of the  $|0\rangle \leftrightarrow |E_y\rangle$  transition and collection of the PSB fluorescence. We carefully calibrate the transferred population measured in the  $|0\rangle$  state using the procedure detailed in Section A.3.

Figure 3.4a shows the populations in the  $|\pm 1\rangle$  states, measured conditionally on the detection of a single circularly polarized ZPL photon. Excellent correlations between the photon polarization and NV spin states are observed.

To complete the verification of entanglement, we now show that correlations persist when ZPL photons are detected in a rotated polarization basis. Upon detection of a linearly polarized  $|H\rangle$  or  $|V\rangle$  photon at time  $t_d$ , the entangled state in Eq. 3.1 is projected to  $|\pm\rangle = \frac{1}{\sqrt{2}}(|+1\rangle \pm |-1\rangle)$ , respectively. These states subsequently evolve in time ( $t$ ) according to

$$|\pm\rangle_t = \frac{1}{\sqrt{2}} \left( e^{-i\omega_+(t-t_d)} |+1\rangle \pm e^{-i\omega_-(t-t_d)} |-1\rangle \right). \quad (3.3)$$

In order to read out the relative phase of superposition states between  $|+1\rangle$  and  $|-1\rangle$ , we use two resonant microwave fields with frequencies  $\omega_+$  and  $\omega_-$  to coherently transfer the state  $|M\rangle = \frac{1}{\sqrt{2}} \left( e^{-i\omega_+t} |+1\rangle + e^{-i(\omega_-t - (\phi_+ - \phi_-))} |-1\rangle \right)$  to  $|0\rangle$  (see Figure 3.3b), where the initial relative phase  $\phi_+ - \phi_-$  is set to the same value for each round



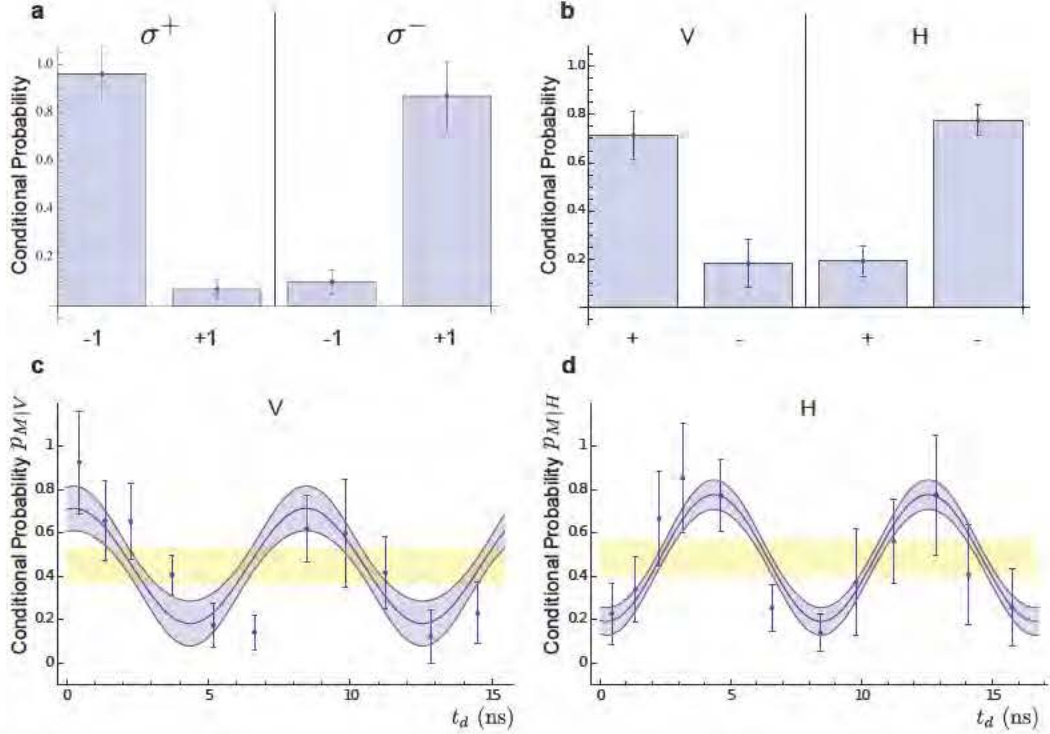


Figure 3.4: Measurement of spin-photon correlations in two bases. **a.** Conditional probability of measuring  $|\pm 1\rangle$  after the detection of a  $\sigma^+$  or  $\sigma^-$  photon. **b.** Conditional probability of measuring  $|\pm\rangle$  after the detection of a  $H$  or  $V$  photon, extracted from a fit to data shown in (c) and (d). **c&d.** Measured conditional probability of finding the electronic spin in the state  $|M\rangle$  after detection of a  $V$  (c) or  $H$  (d) photon at time  $t_d$ . Blue shaded region is the 68% confidence interval for the fit (solid line) to the time-binned data (see Section A.6.1). Errors on data points are one STD. Combined with the data shown in Figure 3.4(a), oscillations with amplitude outside of the yellow regions result in fidelities greater than 0.5. The visibility of the measured oscillations are  $0.59 \pm 0.18$  (c) and  $0.60 \pm 0.11$  (d).

*Chapter 3: Quantum entanglement between an optical photon and a solid-state spin qubit*

---

of the experiment. Thus, the conditional probability of measuring the state  $|M\rangle$  is

$$p_{M|H,V}(t_d) = \frac{1 \pm \cos \alpha(t_d)}{2}, \quad (3.4)$$

where  $\alpha(t_d) = (\omega_+ - \omega_-)t_d + (\phi_+ - \phi_-)$ . Eq. 3.4 indicates that the two conditional probabilities should oscillate with a  $\pi$  phase difference as a function of the photon detection time  $t_d$ . This can be understood as follows. In the presence of Zeeman splitting ( $\delta\omega \neq 0$ ), the NV center's spin state is entangled with both the polarization and frequency of the emitted photon. The photon's frequency provides which-path information about its decay. In the spirit of quantum eraser techniques, the detection of  $|H\rangle$  or  $|V\rangle$  at  $t_d$  with high time resolution ( $\sim 300 \text{ ps} \ll 1/\delta\omega$ ) erases the frequency information [67, 68]. When the initial relative phase between the microwave fields  $\Omega_{\pm 1}$  is kept constant, the acquired phase difference  $(\omega_+ - \omega_-)t_d$  gives rise to oscillations in the conditional probability and produces an effect equivalent to varying the relative phase in the measured superposition, allowing us to verify the coherence of the spin-photon entangled state.

The detection times of ZPL photons are recorded during the experiment without any time gating, which allows us to study spin-photon correlations without reducing the count rate. The resulting data are analyzed in two different ways. First, we time-bin the data and use it to evaluate the conditional probabilities of measuring spin state  $|M\rangle$  as a function of  $|H\rangle$  or  $|V\rangle$  photon detection time (Figures 3.4c,d). Off-diagonal elements of the spin-photon density matrix are evaluated from a simultaneous fit to the binned data (see Section A.6.1). The time bins are chosen to minimize fit uncertainty as described in Section A.6.1. The resulting conditional probabilities are used to evaluate a lower bound on the entanglement fidelity of  $F \geq 0.69 \pm 0.068$ ,

*Chapter 3: Quantum entanglement between an optical photon and a solid-state spin qubit*

---

above the classical limit of 0.5, indicating the preparation of an entangled state.

We further reinforce our analysis using the method of maximum likelihood estimate. As described in Section A.6.2, this method is applied to raw, un-binned ZPL photon detection and spin measurement data and yields a probability distribution of a lower bound on the fidelity. Consistent with the time-binned approach, we find that our data are described by a near Gaussian probability distribution associated with a fidelity of  $F \geq 0.70 \pm 0.070$  (see Figure A.6.2). Significantly, the cumulative probability distribution directly shows that the measured lower bound on the fidelity is above the classical limit with a probability of 99.7 %.

Several experimental imperfections reduce the observed entanglement fidelity. First, the measured strain and magnetic field slightly mixes  $|A_2\rangle$  state with the other excited states. Based on Figure 3.2b, we estimate that  $|A_2\rangle$  state imperfection and photon depolarization in the setup together reduce the fidelity by 12 %, the latter being the dominant effect. Imperfections in readout and echo microwave pulses decrease the fidelity by 3 %. Other error sources include finite signal to noise in the ZPL channel (fidelity decrease 11 %), as well as timing jitter (another 4 %). The resulting expected fidelity (73 %) is consistent with our experimental observations. Finally, the entanglement generation succeeds with probability  $p \sim 10^{-6}$ , which is limited by low collection and detection efficiency as well as the small probability of ZPL emission.

### 3.4 Conclusions and outlook

Entanglement of pairs of remote quantum registers is one important potential application of the technique described in this chapter [69]. This can be done by coincidence measurements on a pair of photons emitted by two remote NV centers. The key figure of merit for such an entanglement operation over a distance  $L$  is proportional to  $p^2 \frac{\gamma T}{1+\gamma\tau}$ , where  $\gamma \sim 2\pi \times 15$  MHz is the spontaneous decay rate of the NV center,  $\tau = L/c$  is the photon travel time, and  $T$  is the memory lifetime. A large figure of merit is critical for applications such as quantum repeaters and entanglement purification protocols. The  $0.5 \mu\text{s}$  spin memory interval in our experiments can be extended to several hundred microseconds using spin echo techniques. Furthermore, by mapping the electronic spin state onto proximal nuclei,  $T$  can be extended to hundreds of milliseconds [65]. The key limitation in attaining a large figure of merit is low  $p$ . It can be circumvented if optical cavities are utilized, which simultaneously enhances emission into the ZPL and improves collection efficiency through integration with appropriate waveguides. For example, by using a photonic crystal nanocavity [70, 71, 72], the potential rate for spin-spin entanglement generation can be about a MHz for  $\tau < 1/\gamma$  and a few Hz for  $\tau$  corresponding to  $L \sim 100$  km, resulting in  $p^2 \frac{\gamma T}{1+\gamma\tau} \geq 1$ . Beyond this specific application, our ability to control interactions between NV centers and quantum light fields demonstrate that quantum optical techniques, such as all-optical spin control, nonlocal entanglement [69], and photon storage [73], can be implemented using long-lived solid-state qubits, paving the way for a wide variety of potential applications in quantum optics and quantum information science.



# Chapter 4

## Laser cooling and real-time measurement of nuclear spin environment of a solid-state qubit

### 4.1 Introduction

Over the past two decades, CPT has been employed for laser cooling of neutral atoms and ions [27], creation of ultra-cold molecules [74], optical magnetometry [75, 76], and atomic clocks [77], as well as for slowing and stopping light pulses [73]. The electronic spin of the NV center is a promising system for extending these techniques to the solid state. The NV center has a long-lived spin triplet as its electronic ground state [39], whose  $m_s = \pm 1, 0$  sublevels are denoted as  $|\pm 1\rangle$  and  $|0\rangle$ . In pure samples, the electron spin dynamics are governed by interactions with the spin-1  $^{14}\text{N}$  nucleus of the NV center and spin-1/2  $^{13}\text{C}$  nuclei present in 1.1 % natural abundance in

the diamond lattice (Fig. 4.1a). Control over nuclear spins [65, 78] is of interest for both fundamental studies and for applications such as nanoscale magnetic sensing [79, 80] and realization of quantum networks [43, 81]. Here we achieve such control via two complimentary methods: effective cooling of nuclear spins through nuclear state selective CPT [82] and conditional preparation based on fast measurements of the nuclear environment and subsequent post-selection [83].

While most prior work involved the use of microwave and RF fields for manipulating both the electronic and nuclear spin states, we utilize all-optical control of the electronic spin [84, 53, 85]. Specifically, we make use of  $\Lambda$ -type level configurations involving the NV center's  $|A_1\rangle$  and  $|A_2\rangle$  optically excited electronic states and the  $|\pm 1\rangle$  ground states (Fig. 4.1a) [81, 33]. At low temperatures ( $<10$  K) and in the limit of zero strain,  $|A_1\rangle$  and  $|A_2\rangle$  are entangled states of spin and orbital momentum coupled to the  $|+1\rangle$  ( $|-1\rangle$ ) state with  $\sigma_-$  ( $\sigma_+$ ) circularly polarized light. Correspondingly, excitation with linearly polarized light drives the NV center into a so-called dark superposition state when the two-photon detuning is zero [86]. In the present case the two-photon detuning is determined by the Zeeman splitting between the  $|\pm 1\rangle$  states due to the combined effect of the Overhauser field originating from the nuclear spin environment and any externally applied magnetic field [82, 87]. When the external field exactly compensates the Overhauser field, the electronic spin of the NV center is pumped into the dark state after a few optical cycles and remains in the dark state, resulting in vanishing fluorescence. This is the essence of the dark resonances and CPT.

## 4.2 Coherent population trapping with NV centers

In our experiments, the  $|A_1\rangle$  and  $|A_2\rangle$  states are separated by approximately 3 GHz and are addressed individually with a single linearly polarized laser at near zero magnetic field. Since there is a finite branching ratio from the  $m_s = \pm 1$  manifold of the electron spin into the  $|0\rangle$  state, we use a recycling laser that drives the transition between  $|0\rangle$  and the  $|E_y\rangle$  excited state, which decays with a small but non-vanishing probability ( $\sim 10^{-2}$ ) back to the  $|\pm 1\rangle$  states. Figure 4.1b presents experimental observation of the CPT spectrum as a function of an external magnetic field at three different powers of a laser tuned to the  $|\pm 1\rangle \rightarrow |A_2\rangle$  transition. While a broad resonance is observed at high power levels, as the power is reduced, we clearly resolve three features in the spectrum separated by 4.4 MHz, which is two times the hyperfine splitting between three  $^{14}\text{N}$  nuclear spin states. This separation corresponds to the magnetic field required to bring the electronic  $m_s = \pm 1$  hyperfine states with equal nuclear spin projection ( $m_I = \pm 1, 0$ ) into two-photon resonance.

The dependance of the CPT resonance width upon the laser power, shown in Figure 4.1c, reveals an important role played by repumping on the near-cycling  $|0\rangle \leftrightarrow |E_y\rangle$  transition. In contrast to a conventional, closed three-level system, this recycling transition can be used to enhance the utility of our CPT system by both decreasing the width of the CPT resonance and increasing the signal to noise ratio. The  $|A_1\rangle$  state decays into the  $m_s = 0$  ground state through the singlet with a substantial probability of  $\sim 40\%$  (see Section B.3). However, the population is returned back

Chapter 4: Laser cooling and real-time measurement of nuclear spin environment of a solid-state qubit

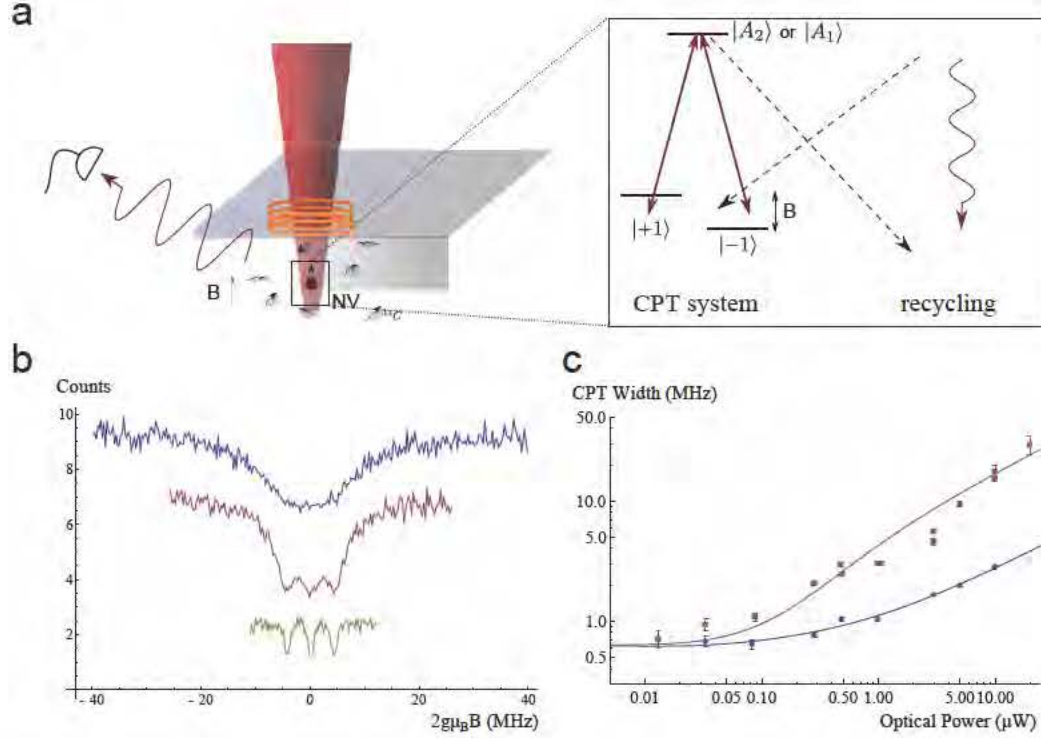


Figure 4.1: Coherent population trapping in NV centers **a.** The  $\Lambda$ -type transitions between the ground states  $|\pm 1\rangle$  and excited states  $|A_{1,2}\rangle$  of a single NV center are addressed with a CPT laser, while a recycling laser drives the  $|0\rangle$  to  $|E_y\rangle$  transition. An external magnetic field is applied using a solenoid. **b.** Photon counts from NVa in a 300  $\mu$ s window are plotted versus the applied field for 10  $\mu$ W (blue), 3  $\mu$ W (red), and 0.1  $\mu$ W (yellow) of laser power addressing the  $|A_2\rangle$  state. Blue and red datasets are shifted vertically by 5 and 2 counts for clarity. **c.** Width of individual  $^{14}\text{N}$  CPT lines versus CPT laser power when the  $|A_1\rangle$  (blue) or  $|A_2\rangle$  (red) state is used. Errorbars in all figures show  $\pm 1$  s.d. Solid curves represent theoretical model discussed in the main text and Section B.2.

*Chapter 4: Laser cooling and real-time measurement of nuclear spin environment of a solid-state qubit*

---

into the  $m_s = \pm 1$  state from  $|E_y\rangle$  only after  $\sim 100$  optical excitation cycles. As a result, away from the two-photon resonance, the NV quickly decays to the  $|0\rangle$  state after being excited, where it then scatters many photons through the  $|0\rangle \leftrightarrow |E_y\rangle$  cycling transition before returning to the  $\Lambda$  system. If the NV center is not in a dark state, this process effectively increases the number of photons we collect by  $2/\eta = \gamma_{s1}/\gamma_{ce}$ , where  $\gamma_{ce}$  is the cross transition rate from  $|E_y\rangle$  into  $|\pm 1\rangle$  and  $\gamma_{s1}$  is the rate from  $|A_1\rangle$  to the singlet. The cycling effect also reduces the width of the CPT line since the  $|0\rangle \leftrightarrow |E_y\rangle$  transition is quickly saturated away from two-photon resonance, provided that the CPT laser excitation rate exceeds the leakage rate out of recycling transition. Significantly, both of these effects lead to improved sensitivity of dark resonances to small changes in two-photon detuning.

To demonstrate this effect, the widths of dark resonances observed via excitation of  $|A_1\rangle$  and  $|A_2\rangle$  are compared in Figure 4.1c. Through an independent measurement of the branching ratios (see Section B.3), we determined that  $|A_{1(2)}\rangle$  corresponds to an open (nearly closed)  $\Lambda$  system with  $\eta_{A_1} \sim 3.1 \times 10^{-2}$  ( $\eta_{A_2} \sim 2.6$ ). These experimental results are compared with a theoretical model described in Section B.2, which predicts that the resonance linewidth  $\delta_0$  is given by  $\delta_0 = \sqrt{R_A^2 / \left[1 + \frac{1}{\eta} \left(\frac{R_A}{R_E} + \frac{2R_A}{\gamma}\right)\right]} \sim \sqrt{R_A R_E \eta \gamma / (R_E + \gamma)}$  for small  $\eta$ , where  $R_{A(E)}$  corresponds to the optical excitation rate by a laser tuned to the  $A(E)$  state and  $\gamma$  is the decay rate of excited states. The width at low powers is determined by the random magnetic field associated with surrounding  $^{13}\text{C}$  nuclear states. When this line broadening mechanism is taken into account (see Section B.2), the experimental results are in excellent agreement with these predictions, plotted as solid lines, showing that a high degree of optical control

over the electronic spins of NV center can be achieved.

## 4.3 Optical cooling and conditional preparation of

### $^{14}\text{N}$ nuclear spin states

Having resolved the hyperfine coupling between the NV electron and  $^{14}\text{N}$  spins, we now demonstrate optical cooling of the nuclear spin states using dark resonances. This method, illustrated in Figure 4.2a, is reminiscent of laser cooling of atomic motion via velocity-selective CPT [27, 82]. A redistribution of the  $^{14}\text{N}$  spin state population upon optical excitation takes place because the hyperfine coupling in the excited electronic state of the NV center is enhanced by a factor of  $\sim 20$  compared to the ground state [41]. If the external field is set such that, for example, the  $m_I = 0$  hyperfine states are in two photon resonance, only the states with nuclear configuration  $m_I = \pm 1$  will be promoted to the excited states, where flip-flops with the electron spin will change the nuclear spin state to  $m_I = 0$ . When the NV center spontaneously decays into the dark superposition of electronic spin states, optical excitation will cease, resulting in effective polarization (cooling) of nuclear spin into  $m_I = 0$  state.

Figure 4.2c presents experimental observation of laser cooling of  $^{14}\text{N}$  nuclear spin via CPT. For each point, the pulse sequence shown in Figure 4.2b is applied, where the magnetic field  $B_{\text{prep}}$  is kept at 0 during the preparation/optical pumping process, while fluorescence is collected when the field is switched to a particular value of  $B_{\text{RO}}$ . The increased contrast of the  $m_I = 0$  CPT line relative to the other two corresponds to a nuclear spin polarization of  $61.5 \pm 4.4\%$ . As shown in Figure 4.2d, by optimizing

Chapter 4: Laser cooling and real-time measurement of nuclear spin environment of a solid-state qubit

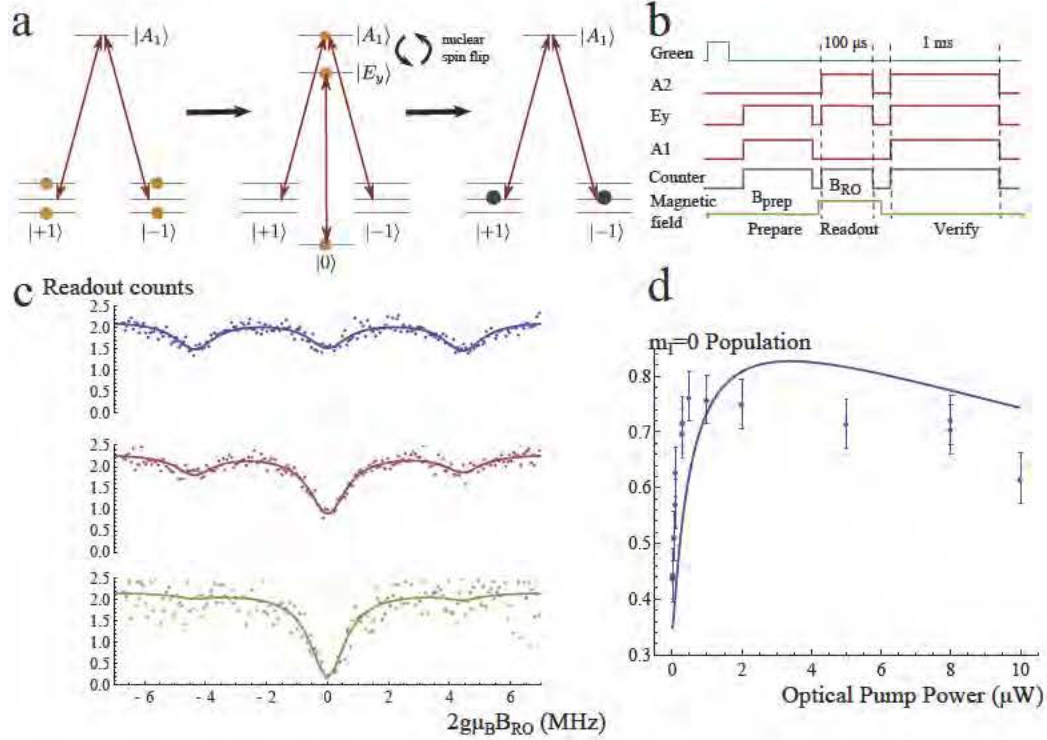


Figure 4.2: Optical control and conditional preparation of the proximal  $^{14}\text{N}$  nuclear spin. **a.** Mechanism for optical pumping of  $^{14}\text{N}$  states. **b.** Pulse sequence for  $^{14}\text{N}$  optical pumping using  $|A_1\rangle$  laser and a fixed readout of the prepared state using  $|A_2\rangle$  laser. To ensure that the NV was not ionized for all subsequent data runs, we turn on all three lasers at the end of each run so that there is no dark state and only keep data from runs where we obtain a high number of counts during this verification step. **c.** Counts collected with NVa during the readout step versus the readout magnetic field for no preparation step (blue) and preparation with optical pumping using 100 nW of  $A_1$  laser power for 1.9 ms (red). Yellow curve shows the results of  $^{14}\text{N}$  polarization via measurement based preparation by selecting the readout events in which the number of counts collected during the last 500  $\mu\text{s}$  of preparation is zero (see Section B.4.2). **d.** Steady-state population in the  $m_I = 0$  state after optical pumping for varying powers of  $A_1$  laser, with theoretical model described in Section B.2 (solid line).

the power of the  $A_1$  laser, we achieve a maximum nuclear polarization of  $76.4 \pm 4.4\%$  within a timescale of  $353 \pm 34 \mu\text{s}$ . The degree of polarization is likely limited by the escape rate out of the dark state due to off-resonant excitation of the  $A_2$  state and dephasing caused by surrounding  $^{13}\text{C}$  nuclei. A simple theoretical model taking into account these two processes and using independently measured parameters (solid line in Fig. 4.2d) reproduces the qualitative features of our experimental results.

We can further improve preparation of the  $^{14}\text{N}$  nuclear spin in a desired state via measurement and post-selection, as predicted by theoretical proposals [87, 83, 88]. Specifically, the observation of zero photodetection events during the preparation step at  $B_{\text{prep}} = 0$  measures the  $^{14}\text{N}$  to be in the  $m_I = 0$  state. For instances where such a measurement result is obtained, the nuclear spin populations are subsequently probed and shown in the bottom plot of Figure 4.2c. The resulting  $^{14}\text{N}$  polarization of greater than  $92 \pm 6\%$  demonstrates that high-fidelity conditional preparation of nuclear spins is possible.

## 4.4 Observation of instantaneous Overhauser field from the $^{13}\text{C}$ spin bath

While the  $^{14}\text{N}$  nuclear spin transitions can be spectroscopically resolved and manipulated individually, we next extend our technique to control the many-body environment of the NV center, consisting of  $^{13}\text{C}$  nuclei distributed throughout the diamond lattice. The large number of nuclear spin configurations associated with an unpolarized environment results in a random Overhauser field ( $B_{\text{ov}}$ ) with unresolved



*Chapter 4: Laser cooling and real-time measurement of nuclear spin environment of a solid-state qubit*

---

hyperfine lines. It produces a finite CPT linewidth in measurements that average over all configurations of the  $^{13}\text{C}$  spin bath (Figure 4.1b, c).

We now describe how this limitation can be circumvented using fast measurements. The key idea of our approach is to make use of the long correlation time ( $T_1^{\text{nuc}}$ ) associated with evolution of the nuclear bath to observe its instantaneous state and its dynamics. Such a fast measurement is illustrated in Figure 4.3a, where the externally applied field is ramped across a single  $^{14}\text{N}$   $m_I = 0$  line while the CPT lasers are on. The yellow curve in Fig. 4.3c shows the lineshape averaged over many experimental runs. At the same time, the intensity plot in Fig. 4.3b shows counts collected in  $80\ \mu\text{s}$  time bins during successive individual runs, many of which distinctly show a narrow dark region. Lorentzian fits to selected experimental scans (blue and red curves in Fig. 4.3c) reveal “instantaneous” CPT resonances with linewidths that are over a factor three less than those of the averaged measurement. The motion of the dark line centers (green dots in Figure 4.3b) indicates that the instantaneous field evolves in time.

In order to provide more quantitative insight into the dynamics of the nuclear environment, we record the fluorescence counts at a fixed value of the external magnetic field with  $80\ \mu\text{s}$  time resolution during 50 ms time intervals. The resulting autocorrelation of photon detection events, shown in Fig. 4.3d, clearly reveals two distinct time scales corresponding to  $\tau_1 = 350 \pm 30\ \mu\text{s}$ , consistent with  $^{14}\text{N}$  nuclear spin polarization timescale, and  $\tau_2 = 8.40 \pm 0.20\ \text{ms}$ . Most significantly, since we can detect dark states of the NV center within  $80\ \mu\text{s}$ , these results clearly indicate that reliable measurements of the Overhauser field is possible within its correlation time.

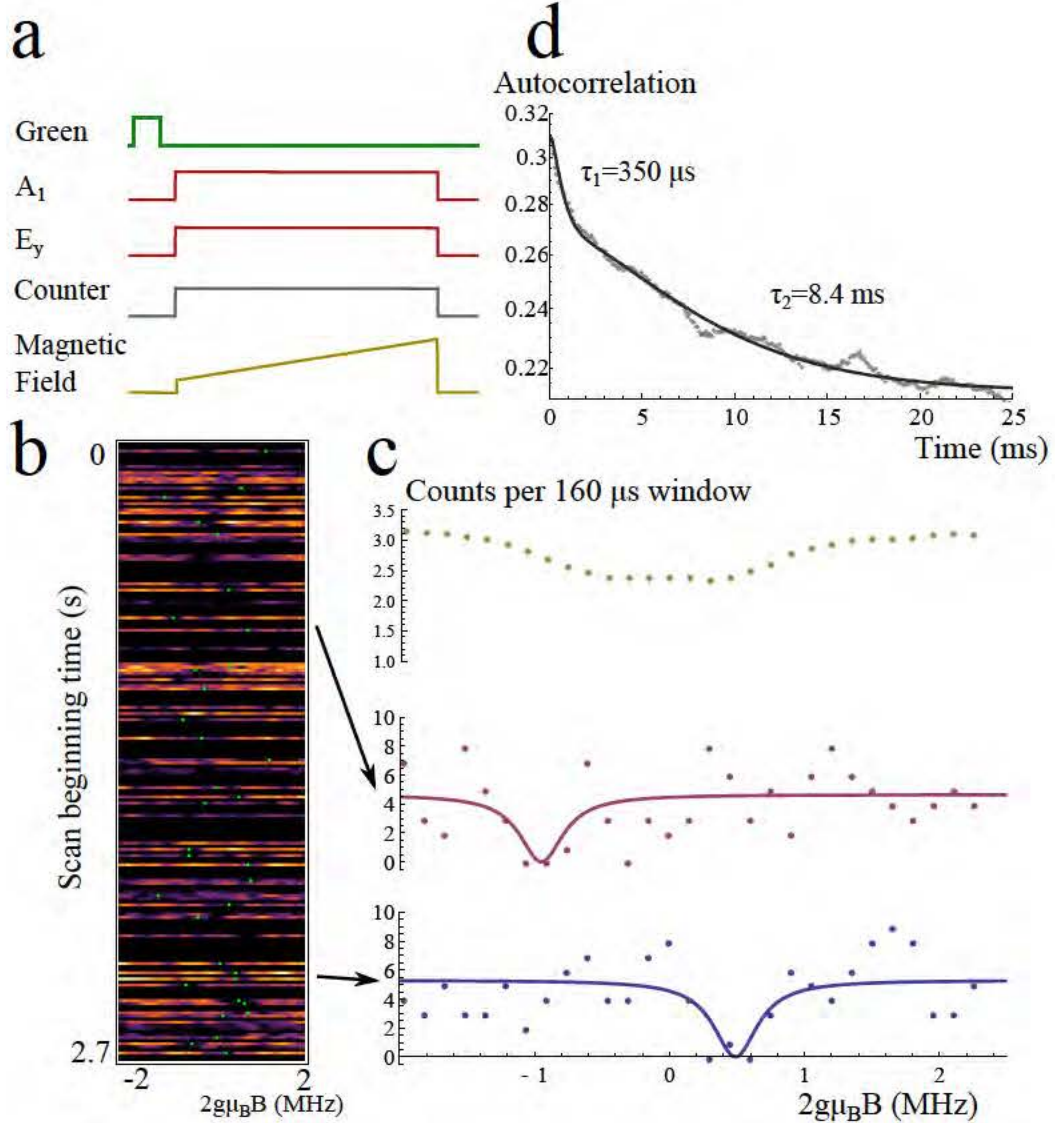


Figure 4.3: Observation of instantaneous Overhauser field from the  $^{13}\text{C}$  spin bath. **a.** Pulse sequence for real-time measurement of the  $^{13}\text{C}$  nuclear configuration. The applied magnetic field is ramped over a single  $^{14}\text{N}$  CPT line over 5 ms while counts are collected in  $80 \mu\text{s}$  bins. **b.** Counts from 200 successive runs are shown on horizontal lines for NVb. Runs where the verification step fails are blacked out. The centers of the constrained Lorentzian fits (Section B.7) to individual runs are indicated with a green dot. **c.** Two such individual runs are shown with their fits (red and blue), along with an average of scans that passed verification (yellow). **d.** Autocorrelation of counts with magnetic field fixed at the  $m_I = 1$   $^{14}\text{N}$  line. Fit is to a bi-exponential decay.

## 4.5 Measurement-based preparation of $^{13}\text{C}$ spin bath

We now demonstrate how fast measurements can be used to conditionally prepare the  $^{13}\text{C}$  environment of the NV center in a desired state with post-selection. We record counts accumulated during both the preparation and readout stages with relatively low power using the sequence shown in Figure 4.4a. Similar to measurement-based preparation of the  $^{14}\text{N}$  spin, by conditionally selecting zero photon detection events during preparation step, we can select the states of the  $^{13}\text{C}$  environment with vanishing two photon detuning  $\delta = 2g\mu_B(B_{\text{prep}} + B_{\text{ov}}) = 0$ , where  $\mu_B$  is the Bohr magneton. The red curve in Figure 4.4b shows (unconditioned) readout counts recorded following the preparation step, while the blue curve shows the result of measurement-based preparation. The measured width of such a conditionally prepared distribution is significantly smaller than the width corresponding to individual  $^{14}\text{N}$  resonances obtained without preparation. We find that while this width depends on  $B_{\text{prep}}$ , the position of the narrow feature follows  $B_{\text{prep}}$ , indicating that we can conditionally prepare the  $^{13}\text{C}$  environment via post-selection in a configuration of our choice (Fig. ramp2). The prepared configurations appear to be long-lived both in the dark ( $\gg 6$  ms, Figure B.9) and in the presence of laser light, consistent with autocorrelation measurements ( $\tau_2 = 8.4$  ms, Fig. 4.3d).

We now discuss the experimental results and explore the limits of our ability to probe and prepare the  $^{13}\text{C}$  environment.

We consider the situation in which the NV center is continuously monitored for a time  $T_{\text{cond}}$ . The average number of photons detected during preparation is given by  $\bar{n}(\delta)T_{\text{cond}}$ , where the photon detection rate  $\bar{n}(\delta) = C\delta^2/(\delta_0^2 + \delta^2)$  is related to

Chapter 4: Laser cooling and real-time measurement of nuclear spin environment of a solid-state qubit

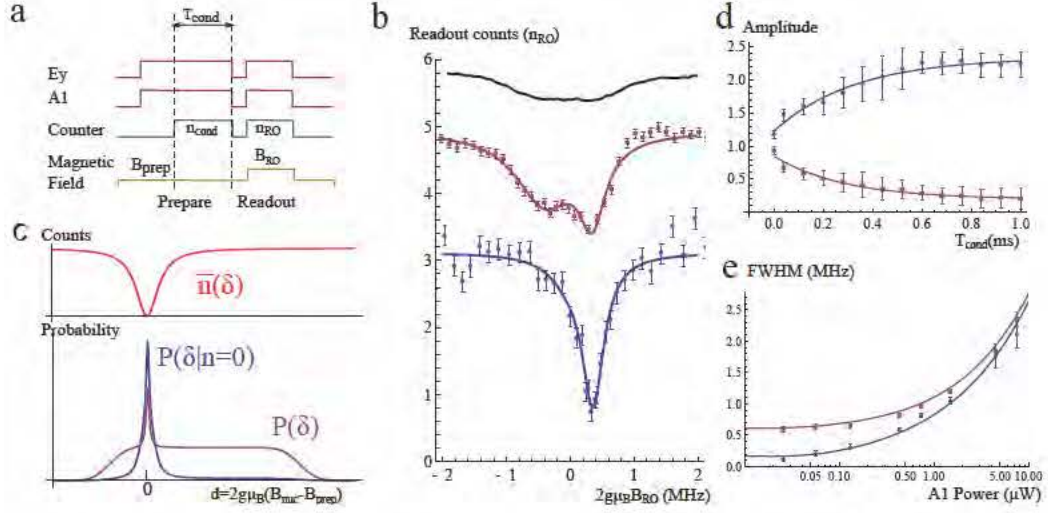


Figure 4.4: Measurement-based preparation of  $^{13}\text{C}$  spin bath. **a.** Pulse sequence for preparation and subsequent measurement of the  $^{13}\text{C}$  configuration.  $B_{\text{prep}}$  is set within the central  $^{14}\text{N}$  line while  $B_{\text{RO}}$  is varied to cover all associated  $^{13}\text{C}$  states. A preceding green laser pulse and  $^{14}\text{N}$  optical pumping step with the  $A_2$  and  $E_y$  lasers are not shown. Counts during a conditioning window of length  $T_{\text{cond}}$  ( $n_{\text{cond}}$ ) at the end of preparation and the readout window ( $n_{\text{RO}}$ ) are recorded for each run. Data presented is an average of many such experimental runs. **b.**  $n_{\text{RO}}$  for NVb versus  $B_{\text{RO}}$  is shown in red with double Lorentzian fit. The same dataset analyzed by keeping only events with  $n_{\text{cond}} = 0$  is shown in blue. Unprepared  $^{13}\text{C}$  distribution from Fig. 4.3 is shown in black for comparison (shifted by 4.3 counts for clarity). **c.** Physics of conditional preparation via measurement. **d.** Amplitude of broad (blue) and narrow (red) distributions versus  $T_{\text{cond}}$  for NVb. The same dataset was used for each point while the length of the conditioning window was changed in post-processing. **e.** Width of measured  $^{13}\text{C}$  distribution with (blue) and without (red) conditional preparation versus  $A_1$  laser power for NVa. Solid lines are theoretical predictions for the readout linewidth  $\delta_0$  (blue) and CPT linewidth for the unprepared  $^{13}\text{C}$  distribution, same as in Fig. 4.1c (red).

*Chapter 4: Laser cooling and real-time measurement of nuclear spin environment of a solid-state qubit*

---

the instantaneous value of the Overhauser field through the two photon detuning  $\delta$  (Fig. 4.4c). The nuclear state probability distribution directly after preparation by conditioning upon obtaining zero counts is  $P(\delta|n=0)$ , which can be related to the conditional probability of a zero count event  $P(n=0|\delta)$  by  $P(\delta|n=0) = P(n=0|\delta)P(\delta)/P(n=0)$ , where  $P(n), P(\delta)$  are unconditional distributions. For a Poisson distributed random process of photon counts, we find that  $P(\delta|n=0) \sim \exp(-CT_{\text{cond}} \times \delta^2/(\delta_0^2 + \delta^2)) \times P(\delta)$ , where  $C$  is the fluorescence rate of the bright state and  $T_{\text{cond}}$  is the measurement time. As  $T_{\text{cond}}$  increases, the range of  $\delta$  for which we obtain  $n=0$  counts due to the existence of a dark state becomes small. At the same time, for large  $\delta$ , we expect the average number of counts to be high, while the probability of detecting  $n=0$  counts due to shot noise is small. This effectively reduces the width of the conditionally prepared nuclear spin distribution.

As illustrated in Fig. 4.4c, conditional measurement prepares an Overhauser field distribution that consists of the broad unconditioned distribution suppressed by  $\exp(-CT_{\text{cond}})$  and a narrow peak with a width  $\delta_c = \sqrt{\ln 2} \delta_0 / \sqrt{CT_{\text{cond}}}$ . The readout step itself has a “resolution” determined by the dark resonance linewidth  $\delta_0$ . The observed features represent a convolution of the dark resonance probe with the conditionally prepared distribution. For the conditional preparation to be effective, we require that  $CT_{\text{cond}} > 1$ , and therefore  $\delta_c < \delta_0$ , indicating that the measured CPT linewidth will be limited by the readout step. Experimentally, we find that our measured lineshapes can be well fitted with the combination of a narrow and a broad Lorentzian distribution whose width and position are mostly independent of photo-detection time  $T_{\text{cond}}$ . However, as  $T_{\text{cond}}$  is increased, the relative weight of the narrow

distribution increases (Figure 4.4d). This is consistent with the theoretical prediction that the readout-limited narrow resonance width does not depend on  $T_{\text{cond}}$ , while better discrimination in conditional measurements increases the probability that the nuclear spin state is in the narrow distribution.

Interestingly, we find that even without conditioning (red line Figure 4.4b), a narrow distribution of nuclear spin configurations around  $B_{\text{prep}}$  is prepared. This modification of the nuclear distribution is a result of CPT-based laser cooling of the  $^{13}\text{C}$  bath, consistent with the predictions of Reference [82]. The specific physical mechanism of such cooling likely involves electronic spin dependent evolution of the  $^{13}\text{C}$  nuclei, and will be discussed in detail in future studies. We emphasize this observation gives a clear indication that the magnetic environment is affected by the dynamics of the NV, providing direct evidence that the NV spin dynamics is dominated by the Overhauser field rather than external magnetic field fluctuations.

Figure 4.4e shows the dependence of the observed linewidth of the narrow feature on the CPT laser power. At low powers the observed width reaches a minimum value of  $104 \pm 49$  kHz. The limiting width results from the effects of strain splitting of the  $|\pm 1\rangle$  states on the readout process at zero magnetic field (see Section B.5 for a quantitative discussion of effects of strain) [89]. Due to this splitting, very small magnetic field changes do not shift the energies of  $|\pm 1\rangle$  to first order. Therefore our CPT readout signal becomes insensitive to Zeeman shifts on the order of twice the strain splitting (see Section B.5). In addition, a minimal linewidth of  $\sim 400$  kHz was obtained for measurements performed with a separate NV center (NVb) subject to higher strain.

## 4.6 Conclusions and outlook

The limit associated with strain splitting can be easily circumvented by using a large external magnetic field to split the  $|\pm 1\rangle$  spin states and two laser frequencies to address the NV center in a Raman configuration near zero two-photon detuning. As described in Section B.10, a modest increase in collection efficiency by an order of magnitude [90] would allow us to obtain quantum-limited narrowing of nuclear distribution  $\delta_c \sim 1/T_{\text{cond}}$ , which, in turn, can be on the order of the inverse lifetime of the given nuclear configuration [82].

The presented experiments open intriguing prospects for using coherent optical techniques to control nuclear spins surrounding quantum emitters. For instance, they can be used to study quantum many-body dynamics of so-called central-spin models in real time, either in isolation or in the presence of dissipation [91]. Specifically, nuclear field diffusion can be explored that, in the presence of CPT lasers, is expected to have very interesting statistical properties reminiscent of Levy flights in VSCPT [26]. Furthermore, the present approach allows for direct application of quantum feedback control to deterministically drive nuclear spins into a desired state. This may be used to prepare non-classical superposition states of the nuclear spins analogous to spin-squeezed states in atomic ensembles [92] and to “engineer” collective dissipation for nuclear spin ensembles useful for applications in quantum information science, such as long-term storage of quantum states [93]. Finally, our method allows for a new all-optical approach to magnetic sensing [75, 76] that may enable interesting applications in nanoscience [79, 80].

## Chapter 5

# Coherent optical transitions in implanted nitrogen vacancy centers

### 5.1 Introduction

In this chapter, we report the observation of stable optical transitions in NV centers created by ion implantation. Using a combination of high temperature annealing and subsequent surface treatment, we reproducibly create NV centers with zero-phonon lines (ZPL) exhibiting spectral diffusion that is close to the lifetime-limited optical linewidth. The residual spectral diffusion is further reduced by using resonant optical pumping to maintain the  $\text{NV}^-$  charge state. This approach allows for placement of NV centers with excellent optical coherence in a well-defined device layer, which is a crucial step in the development of diamond-based devices for quantum optics, nanophotonics, and quantum information science.

The negatively charged NV center in diamond is a solid state system that com-



*Chapter 5: Coherent optical transitions in implanted nitrogen vacancy centers*

---

bines excellent spin coherence with atomic-like optical transitions at cryogenic temperatures. Because of these properties, the NV center has emerged as a promising candidate for the realization of unique applications in the fields of quantum information, quantum optics, and metrology [25, 80, 94]. While many of these applications make use of coherent interactions between light and NV centers [81, 24, 23], the optical transitions of atom-like solid-state systems are generally imperfect because of the influence of the solid state environment. In particular, the energies of the NV center's optically excited states are highly sensitive to local electric fields. Therefore, fluctuations in the charge environment around the NV center cause fluctuations in the frequency of the optical transition. This phenomenon, which is referred to as spectral diffusion, is a generic effect associated with optical transitions in atom-like solid state systems [95, 96]. Techniques to suppress and eliminate spectral diffusion are currently being actively explored [54, 47, 24].

To investigate the optical properties of NV centers, photoluminescence excitation (PLE) studies are typically performed by repeatedly scanning a resonant excitation laser through the NV center's ZPL [44, 45, 52, 97, 54, 47, 98, 48]. A 532 nm laser is applied at the end of each scan to reverse potential photoionization of the NV center caused by the resonant laser. For a single PLE scan, one typically observes a narrow resonance. A nearly lifetime-limited single-scan linewidth of 16 MHz has been reported in a single diamond nanocrystal [44], and a lifetime-limited single-scan linewidth of 13 MHz was measured for a native NV center inside a natural diamond sample [45]. However, these measurements of the single-scan linewidth exclude the effects of spectral diffusion. It was observed that the narrow resonance jumps to a

---

*Chapter 5: Coherent optical transitions in implanted nitrogen vacancy centers*

---

different frequency for each successive PLE scan, indicative of local charge fluctuations caused by the repumping laser [44, 52, 97]. Previously, it has been shown that off-resonant excitation can photoionize localized defects inside and on the surface of the diamond crystal, leading to the observed spectral jumps [49, 54]. When the NV center is monitored over long timescales, such behavior results in an overall linewidth that can be much larger than the single-scan linewidth. This long-term, extrinsically broadened linewidth, rather than the single-scan linewidth, is the limiting factor for most applications requiring spectral stability. For example, remote entanglement of NV centers relies on interference of photons with well defined matching frequencies [24]. Efficient photonic devices such as single photon switches and transistors make use of strong NV-photon interactions and require that the emitters remain on resonance with the incident light [99]. Therefore, a number of different techniques have been explored to reduce the effects of spectral diffusion, including active stabilization and pre-selection of the transition frequency [47, 24]. However, all of these techniques increase the technical complexity and limit the repetition rate of the experiments. The “on demand” creation of emitters with inherently low spectral diffusion under repeated excitation over long timescales is an outstanding challenge in implementing scalable applications using quantum optics with atom-like systems.

Since one-of-a-kind natural diamond samples such as the one investigated in [45] cannot be used as reproducible starting materials for scalable systems, recent experiments have made use of NV centers incorporated into high quality synthetic diamond during the growth process [24, 47, 48]. In addition to imperfections in their optical coherence, NV centers introduced during the diamond growth process are limited in

their usefulness due to their low concentration and random locations. For example, in order to incorporate NV centers into nanophotonic or nanomechanical devices, it is necessary to develop a method to create a controllable concentration of emitters in a well defined device layer while maintaining their excellent optical properties.

The key idea of this work is to create NV centers in a surface layer that exhibit coherent optical transitions with nearly lifetime-limited linewidths even under the effects of spectral diffusion. We accomplish this by first introducing NV centers at a well defined and controllable depth using ion implantation [100]. We then demonstrate how to suppress the fundamental cause of spectral diffusion by creating a diamond environment that is nearly free of defects that contribute to charge fluctuations. This is achieved through a combination of annealing and surface treatments. Finally, we further improve the optical properties of the NV centers by combining our approach with a newly developed technique for preventing photoionization of the remaining charge traps [97].

## 5.2 Procedure for NV center creation

Fig. 5.1 summarizes the experimental procedure to create shallow implanted NV centers with narrow optical lines. As our starting material we use single crystal diamond from Element Six grown using microwave assisted chemical vapor deposition (CVD). The single crystal samples were homoepitaxial grown on specially prepared  $\langle 100 \rangle$  oriented synthetic diamond substrates, taking care to ensure that the surface quality of the substrates was as high as possible to reduce sources of dislocations. The CVD synthesis was performed using conditions as described in [101, 102]. The

---

*Chapter 5: Coherent optical transitions in implanted nitrogen vacancy centers*

---

resultant diamond material is measured using electron paramagnetic resonance (EPR) to have a nitrogen concentration of less than 5 parts per billion. The surface layer of these samples is generally damaged and highly strained because of mechanical polishing. Therefore, we first remove the top several micrometers of the sample using a 30 min Ar/Cl<sub>2</sub> etch followed by a 20 min O<sub>2</sub> etch in an UNAXIS Shuttleline inductively coupled plasma-reactive ion etcher. We then implant <sup>15</sup>N<sup>+</sup> ions at an energy of 85 keV at a variety of doses from 10<sup>9</sup>/cm<sup>2</sup> to 10<sup>12</sup>/cm<sup>2</sup>. According to simulations done using Stopping and Range of Ions in Matter (SRIM), this should result in a mean nitrogen stopping depth of  $\sim 100$  nm with a straggle of  $\sim 20$  nm [103]. Subsequently, we anneal the implanted samples under high vacuum ( $P < 10^{-6}$  Torr). Our standard annealing recipe consists of a 4 hour 400°C step, a 2 hour 800°C step, and a 2 hour 1200°C step, with a 1 hour ramp up to each temperature. The motivation behind these temperature steps will be explained later in the text. It is important that a good vacuum is maintained throughout the annealing process, since diamond etches and graphitizes under residual oxidizing gasses at such high temperatures [104]. Following the anneal, we remove graphitic carbon and other surface contaminants by cleaning the diamonds for one hour in a 1:1:1 refluxing mixture of sulfuric, nitric, and perchloric acids. Finally, we perform a 465°C anneal in an O<sub>2</sub> atmosphere in a rapid thermal processor (Modular Process Technology, RTP-600xp) in three 48 minute steps following the recipe used in [105]. This oxygen anneal is believed to remove  $sp^2$  hybridized carbon and result in a more perfect oxygen termination of the surface than acid cleaning alone. We have observed that it enhances charge stability in the NV<sup>-</sup> state and helps to reduce blinking and photobleaching.

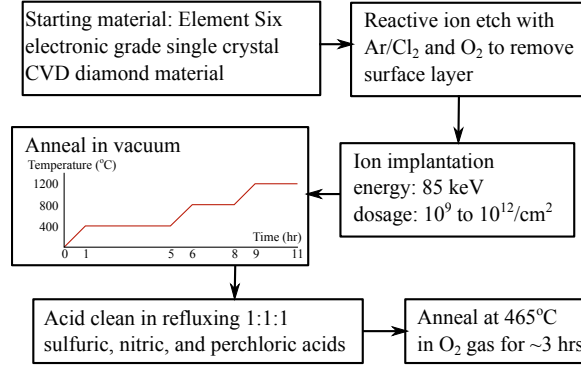


Figure 5.1: Procedure for creating spectrally stable NV centers through ion implantation, annealing, and surface treatment. The Ar/Cl<sub>2</sub> (O<sub>2</sub>) etch was done using an ICP power of 400 W (700 W), a RF power of 250 W (100 W), a DC bias of 423 V (170 V), a chamber pressure of 8 mTorr (10 mTorr), and a gas flow rate of 25/40 sccm (30 sccm). The sample temperature was set to 17°C.

### 5.3 Spectroscopy of implanted NV centers

We investigate the resulting NV centers using a low-temperature confocal microscopy setup, where the diamond samples are cooled to  $<10$  K in a helium flow cryostat (Janis ST-500). Fig. 5.2(a) shows confocal images taken with  $\sim 1$  mW 532 nm laser excitation for four different implantation doses. An implantation dose of  $10^9/\text{cm}^2$  results in a very low density of NV centers, comparable to the native NV concentration in some electronic grade samples. A dose of  $10^{12}/\text{cm}^2$  results in a high density layer of completely unresolvable NV centers. At an intermediate dose of  $10^{10}/\text{cm}^2$ , however, we obtain resolvable single NV centers with a density on the order of  $1 \text{ NV}/\mu\text{m}^2$ , implying a conversion efficiency of  $\sim 1\%$ . Comparing the fluorescence intensity to the single NV count rate, we can roughly estimate that, in the  $10^{11}/\text{cm}^2$  sample, there are  $\sim 10$  NV centers per focal spot, while in the  $10^{12}/\text{cm}^2$  sample, there are  $\sim 100$  NV centers per focal spot. We note that the conversion efficiency is

*Chapter 5: Coherent optical transitions in implanted nitrogen vacancy centers*

somewhat lower than previously reported values, which could result from differences in starting material, dose calibration, and annealing procedures [100].

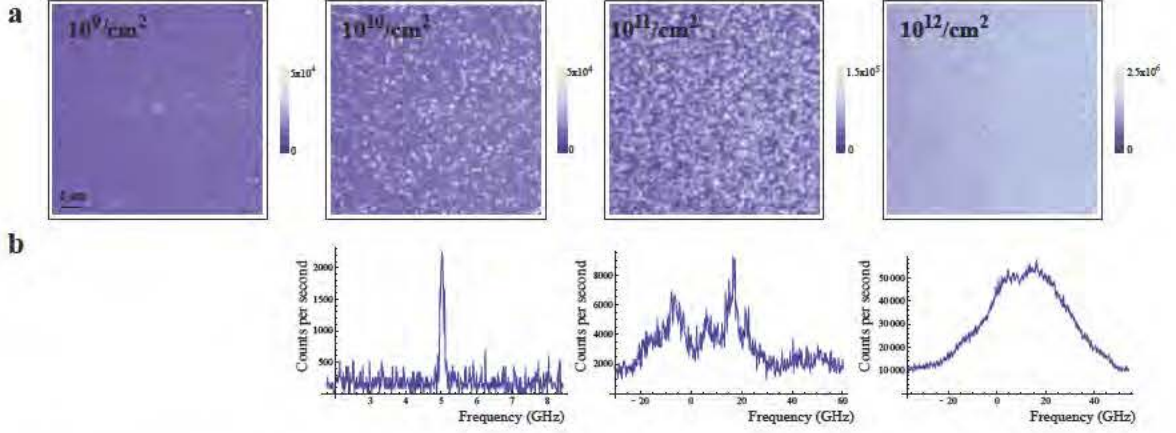


Figure 5.2: (a) Confocal images of the implanted layer of NV centers for four different nitrogen ion doses. (b) Corresponding PLE spectra for the three highest doses.

In Fig. 5.2(b), we present corresponding ZPL spectra of NV centers for the three highest implantation doses. The spectra were taken by scanning an external cavity diode laser around 637.2 nm while collecting fluorescence in the phonon-sideband (PSB). 532 nm excitation was performed at each point of the scan to alleviate the effects of photoionization during resonant excitation. We emphasize here that Fig. 5.2(b) and Fig. 5.3(b-d) present spectra that are averages of many successive laser scans taken over the course of minutes. Therefore, they are indicative of the spectral stability of NV centers over both short and long time scales and include all effects of spectral diffusion caused by the repumping laser. Beyond these timescales, longer-term drifts of the NV frequency can be easily compensated by electric fields or tuning the excitation frequency with minimal cost to the experimental repetition rate. At a dose of  $10^{10}/\text{cm}^2$ , most single NV centers exhibit narrow PLE lines. As the dose

*Chapter 5: Coherent optical transitions in implanted nitrogen vacancy centers*

---

increases to  $10^{11}/\text{cm}^2$ , the spectra show multiple features with several broader peaks. Finally, at  $10^{12}/\text{cm}^2$ , the spectrum is a mostly featureless peak several tens of GHz wide. We note here that the spectra for the two highest doses exhibit the effects of both increased single NV center linewidths and the presence of several NV centers in the focal spot. If the linewidths were comparable to the  $10^{10}/\text{cm}^2$  sample, we should be able to observe a collection of narrow resonances spread over the scan range. However, this is not the case, which is an indication that increased nitrogen concentration in the environment of the NV center leads to additional spectral diffusion. Indeed, the substitutional nitrogen defect has an ionization energy threshold of 2.2 eV and therefore can be photoionized with 532 nm light, which has an energy of 2.33 eV/photon [106].

From this point on, we focus on samples implanted with a dose of  $10^{10}/\text{cm}^2$ . Fig. 5.3(a) shows a histogram of linewidths for 50 NV centers in four such samples. While there is a range of linewidths, a majority of NV centers exhibit linewidths less than 500 MHz, which is comparable to naturally occurring NV centers deep inside electronic grade CVD diamond [24]. This is an indication that we have eliminated most impurities with fluctuating charge states in the vicinity of the NV centers, which may include both impurities on the nearby surface and defects inside the diamond introduced by the implantation process. In Fig. 5.3(b), we present an example spectrum of the narrowest linewidth we have observed, along with the results of twenty-one successive PLE scans to demonstrate the long-term stability of the transition line. Our measured linewidth of  $37 \pm 4.8$  MHz under conventional 532 nm repumping is, to the best of our knowledge, a record for the extrinsically broadened linewidth of NV

centers.

To further reduce residual spectral diffusion of the NV centers, we incorporate a technique recently demonstrated in [97]. Instead of using 532 nm light to repump the  $\text{NV}^0$  state into  $\text{NV}^-$ , we use a home-built tunable frequency doubled external cavity diode laser operating at 575 nm to resonantly excite the  $\text{NV}^0$  ZPL, which has been shown to efficiently convert the NV center back to the negatively charged state even at very low powers. The 575 nm laser was turned on and scanned across the  $\text{NV}^0$  ZPL between each frequency scan of the 637 nm spectroscopy laser. As was also demonstrated in [97], this method results in a drastic reduction of the spectral diffusion because of the lower incident intensity and energy per photon of the 575 nm excitation (2.16 eV/photon) compared to the conventional 532 nm excitation. For example, the NV shown in Fig. 5.3(c) has a  $\text{NV}^-$  ZPL linewidth of 161 MHz using 532 nm excitation. The linewidth was reduced to 27 MHz using the 575 nm repumping technique (Fig. 5.3(d)).

## 5.4 Mechanism for NV center creation

We now discuss our sample preparation process in more detail and propose a mechanism for the creation of optically stable NV centers through high temperature annealing. In general, annealing is required after ion implantation to mobilize vacancies such that they combine with the nitrogen atoms to form NV centers. In addition, the annealing process causes other defects to become mobile at particular temperatures and potentially migrate to the surface, effectively repairing any damage to the crystal caused by implantation. Earlier works have employed a range of



*Chapter 5: Coherent optical transitions in implanted nitrogen vacancy centers*

---

different annealing temperatures, typically in the range between 400°C and 1000°C. Several temperature steps in this range were shown to enable specific mechanisms important to the efficient formation of stable NV centers. In particular, at 400°C, earlier work has indicated that vacancies and interstitial nitrogen atoms introduced by implantation migrate and annihilate with each other [107]. At 800°C, vacancies become mobile and combine with nitrogen atoms on lattice sites to form NV centers, which then remain stable [108]. At temperatures much less than 800°C, this process is too slow to allow NV formation in a reasonable time period. At temperatures much higher than 800°C, the vacancies are highly mobile, but there is indication that the rate of NV formation is suppressed [109]. This could be because of the higher thermal energy in the diamond lattice, which causes the local strain field around the isolated nitrogen defects to become less efficient at trapping migrating vacancies.

At even higher temperatures, additional defects such as divacancies,  $sp^2$  type defects, and hydrogen become mobile and anneal out [110, 108, 111]. Recent work has demonstrated that annealing at a temperature of 1200°C significantly improved the coherence properties of implanted NV centers [112]. This indicates that some of the remaining defects after 800°C annealing are paramagnetic. The electronic and optical properties of these defects, such as the level structure and ionization energies, have generally not been well studied. However, we have briefly investigated the optical properties of samples annealed without the 1200°C step and found that, while a few NV centers had linewidths greater than several hundred MHz, most had PLE lines that were too broad to be discernible. These results provide evidence that annealing at high temperatures eliminates localized defects that can affect the optical properties

of NV centers. The exact structure and properties of these defect states remain to be determined through, for example, EPR measurements, optical spectroscopy, and ab initio calculations of energy level structures.

## 5.5 Conclusions

Our work shows that it is possible to create implanted NV centers with excellent optical coherence properties, opening up a large range of possibilities for future studies and applications. In addition to a better understanding of the material and defect properties that contribute to spectral diffusion, there are many other aspects and parameters of our technique that remain to be explored. For example, while we have not extensively studied the dependence of optical coherence on implantation depth, there is evidence that reasonably stable transitions are possible with much shallower NV centers. We have observed linewidths of a few hundred MHz from several NV centers in a diamond sample created by implantation with a nitrogen dose of  $10^{11}/\text{cm}^2$  at an energy of 6 keV, giving a nominal depth of 10 nm. Further systematic studies on the effect of implantation energy, dose, and annealing recipes are needed to explore the possibility of creating optically coherent NV centers in high densities or very close to the diamond surface for applications such as coupling of multiple NV centers and electric field sensing.

Another important application that has recently become the focus of much effort is the implementation of nanoscale photonic structures to tailor the interaction of light and NV centers [113]. Thus far, all previous demonstrations of diamond-based photonic structures have used diamond materials with a high density of native NV

*Chapter 5: Coherent optical transitions in implanted nitrogen vacancy centers*

---

centers, whose linewidths are generally many GHz or more [113, 114]. To realize quantum nanophotonic devices in deterministic, scalable fashion, it is important to begin with a bulk material that contains very high quality emitters in a well-defined device layer. For this reason, the ability to controllably create NV centers with inherently good optical coherence, which we have demonstrated in this work, is a crucial step for the practical development of many diamond-based quantum nanophotonic devices and scalable quantum technologies.

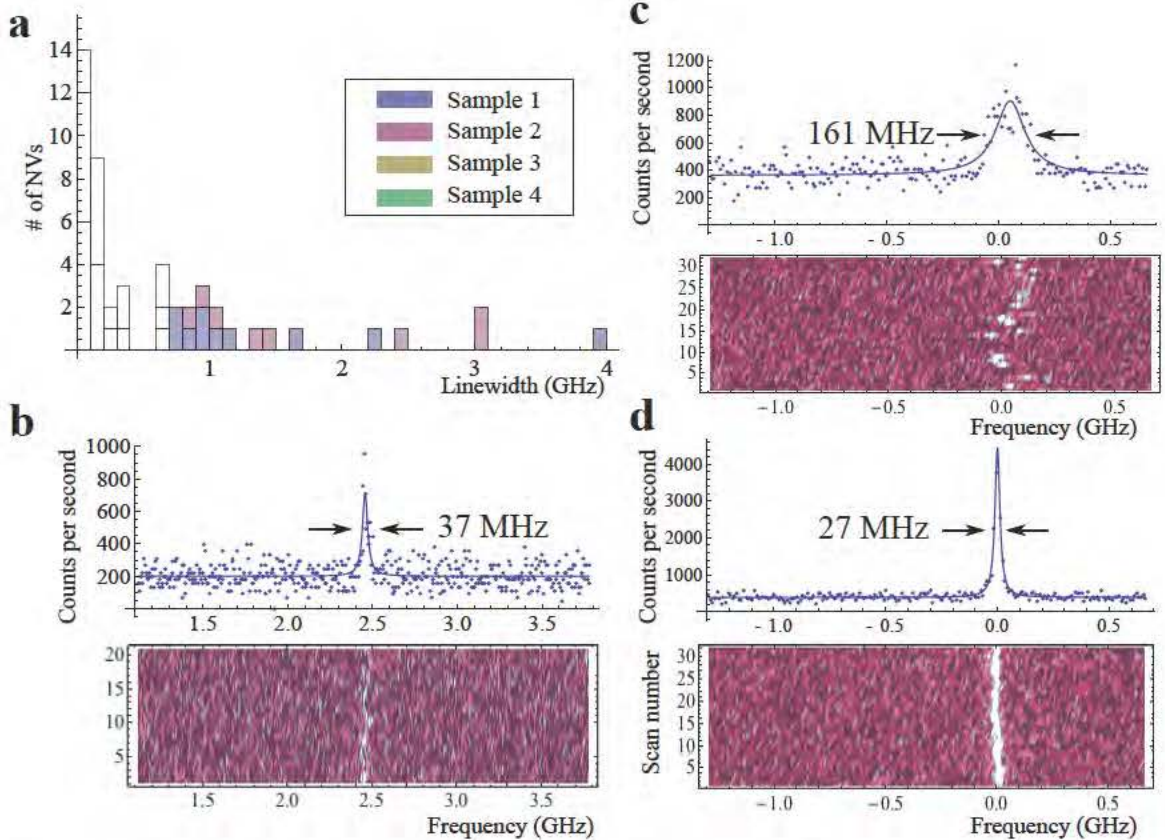


Figure 5.3: (a) Histogram of linewidths for NV centers in four samples implanted with a dose of  $10^{10}/\text{cm}^2$  using 532 nm excitation to repump the NV into the negative charge state. (b) Spectrum showing the narrowest linewidth from (a) (top) obtained by averaging twenty-one successive PLE scans (bottom). Each scan takes  $\sim 2$  seconds. (c) Spectrum of another NV taken using 532 nm repump (top). Corresponding single PLE scans illustrating spectral jumps due to repumping (bottom). (d) Spectrum of the same NV as in (c), taken using 575 nm resonant excitation of the  $\text{NV}^0$  state to repump back into  $\text{NV}^-$ .

# Chapter 6

## Diamond-based nanophotonic devices

### 6.1 Introduction

In chapters 2 to 4, we have demonstrated the potential of using the NV center's optical properties for a variety of different applications. However, the NV center is not a perfect optical emitter for several reasons. First, the Debye-Waller factor  $\xi$ , defined as the ratio of emission into the ZPL vs. the total emission, is only 3-5 %. This is dictated by the relatively large shift in nuclear coordinates between the NV center's ground and excited states, which, by the Franck-Condon principle, results in decay from the excited state into phonon-coupled higher vibrational levels of the ground state [115]. In addition to such intrinsic properties of the NV center, there are also external effects such as spectral diffusion that result in non-ideal optical properties. While we can eliminate these effects to a large degree, as demonstrated in Chapter

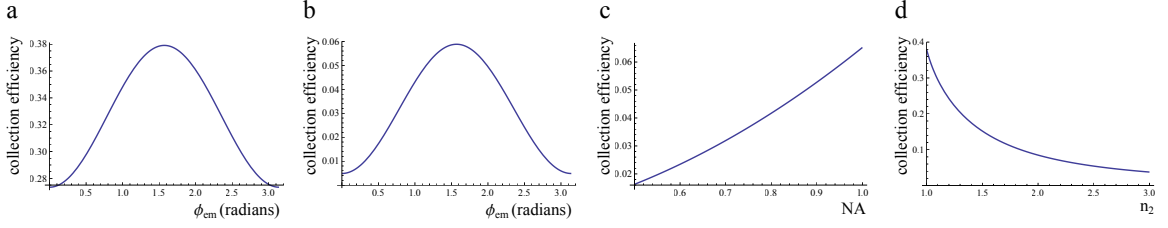


Figure 6.1: Collection efficiency of light from a dipole emitter. **a.** Collection efficiency vs. dipole orientation for NA=0.95 and  $n_2=1$ . **b.** Collection efficiency vs. dipole orientation for NA=0.95 and  $n_2=2.4$ . **c.** Collection efficiency vs. NA for  $\phi_{em} = \pi/2$  and  $n_2 = 2.4$ . **d.** Collection efficiency vs.  $n_2$  for  $\phi_{em} = \pi/2$  and NA=0.95.

5, some residual imperfections in spectral stability usually remain. Additional techniques to stabilize the transition frequency, such as feedback techniques with applied electric fields, reduce the repetition rate of the experiments. Finally, it is generally difficult to extract photons from bulk diamond material with high efficiency. Due to the high index of refraction, total internal reflection confines most of the light inside the diamond at an air interface. In general, as shown in [116], the collection efficiency of a lens or objective with numerical aperture NA in a medium with index  $n_1$  for light from a dipole source in index  $n_2$  is given by

$$C = \frac{1}{8} \left( 4 - 3\cos\theta_{max} - \cos^3\theta_{max} + 3(\cos^3\theta_{max} - \cos\theta_{max})\cos^2\phi_{em} \right), \quad (6.1)$$

where  $\phi_{em}$  is the angle of the dipole axis with the optical axis, and  $\theta_{max} = \sin^{-1}(NA * n_1/n_2)$  is the effective NA of the collection optics. For reference, the collection efficiency is plotted against several parameters in Figure 6.1. As can be seen, even for optimal dipole orientation and a 0.95 NA objective in air, only around 6% of the emitted photons are collected from a NV center in bulk diamond.

The combination of these factors result in a very low rate of indistinguishable, coherent photons from single NV centers. One promising path toward alleviating all of

these imperfections is incorporating NV centers with photonic structures. For example, optical cavities can be used to enhance the emission into the ZPL and overcome spectral diffusion, while coupling to waveguide structures can increase the efficiency of photon collection and detection. This chapter will explain the concept of using cavity quantum electrodynamics (cQED) to make the NV center a more perfect emitter and summarize some ongoing work to implement diamond-based nanophotonic devices.

## 6.2 Cavity QED with NV centers

Cavity QED has been used in a large variety of systems to enhance the interaction between an emitter and a mode of the electromagnetic field inside the cavity. These systems range from atoms and ions coupled to optical cavities to superconducting qubits coupled to microwave stripline resonators. One particularly successful example of cavity QED with solid state systems in the optical domain is quantum dots inside photonic crystal or Bragg structure cavities, where strong coupling between the emitter and cavity mode has been demonstrated [70, 117]. There has also been a large body of work on cavity QED with NV centers. Many of these demonstrations involve diamond nanocrystals, which can be relatively easily incorporated into separate resonator structures, such as Fabry-Perot cavities, ring resonators, and photonic crystal cavities [118, 119, 120]. This approach has the advantage that it allows for flexibility in the cavity design and material. However, in these hybrid systems, the position of the NV center does not usually overlap well with the mode of the cavity. In addition, the optical properties of NV centers are generally quite poor, and no optical transitions with long-term stability have been reported. Our work focuses instead on

fabricating nanoscale photonic structures out of the diamond material itself directly around NV centers. There has also been much progress in this field [114, 121]. However, the goal of combining optical coherent NV centers with nanoscale structures has yet to be achieved.

The idea of using cavity QED to improve the emission properties of a NV center is as follows: When a NV center is placed inside the an optical cavity, its emission into the cavity mode is enhanced. By tuning the cavity mode to the NV center's ZPL, the ZPL emission is therefore enhanced relative to the PSB emission. When this enhancement becomes larger than the Debye-Waller factor, the ZPL becomes the dominant emission channel of the NV center. This enhancement of the emission also means that the lifetime of the NV center is decreased and the lifetime-limited linewidth of the ZPL is increased. When the lifetime-limited linewidth becomes much larger than the spectral diffusion, the NV center can be viewed as a perfect emitter of indistinguishable photons. In other words, the energy uncertainty of the excited state caused by fast decay into the cavity mode is large enough that the energy uncertainty introduced by spectral jumps is negligible.

We can calculate the lifetime of a NV center coupled to the cavity ( $\tau$ ) compared to one that is decoupled from the cavity ( $\tau_0$ ). They are related through a quantity called the Purcell factor, given by

$$\begin{aligned} P &= \frac{3}{4\pi^2} \left( \frac{\lambda_0}{n} \right)^3 \frac{Q |\vec{E}_{NV} \cdot \vec{\mu}_{ZPL}|^2}{V |\vec{E}_{max}|^2 |\vec{\mu}_{NV}|^2} \\ &= \frac{\tau_0}{\tau} - 1 \end{aligned} \tag{6.2}$$

where  $\lambda_0/n$  is the wavelength of the resonant mode inside the cavity and  $Q$  is the quality factor of the cavity.  $\vec{E}_{NV}$  and  $\vec{E}_{max}$  are the electric fields at the NV and



maximum field inside the cavity, respectively. The mode volume of the cavity is defined as

$$V = \frac{\int |\vec{E}(\vec{x})|^2 dV}{|\vec{E}_{max}|^2} \quad (6.3)$$

Finally,  $\vec{\mu}_{ZPL}$  is the effective dipole moment of the ZPL transition, which is the only part coupled to the cavity, while  $\vec{\mu}_{NV}$  is the total dipole moment of the NV center. The Debye-Waller factor is then given by  $\xi = |\vec{\mu}_{ZPL}|^2/|\vec{\mu}_{NV}|^2$ . The Purcell factor gives the enhancement of emission into the cavity mode over the emission when the NV is decoupled from the cavity. Here, we define “decoupled” as an NV that is still spatially located in the cavity, but detuned from the cavity mode in frequency, as is the case in our experiments. This means that  $n$  in the expression above is the effective index including all possible modes of the structure. Although this quantity can be difficult to estimate, it is somewhere between 1 and 2.4, the index of bulk diamond.

While the Purcell factor expresses the relevant enhancement of emission in terms of experimentally relevant quantities, it is equivalent to the cooperativity, which gives more physical intuition as simply the ratio between the coupling strength of the emitter to the cavity and the decay rates of the system. The Purcell factor or cooperativity can also be written as

$$P = \frac{2g^2}{\kappa\gamma} \quad (6.4)$$

where  $\kappa = \omega/Q$  is the decay rate from the cavity, with  $\omega$  being the cavity frequency.  $\gamma$  is the decay rate of the NV center into modes other than the resonant cavity mode, and is given by

$$\gamma = \frac{\omega^3 |\mu_{NV}|^2}{3\pi\epsilon\hbar c^3} = \frac{8\pi^2 |\mu_{NV}|^2}{3\epsilon\hbar} \left(\frac{n}{\lambda_0}\right)^3. \quad (6.5)$$

The single-photon Rabi frequency  $g$  is given by  $g = \vec{E}_{NV} \cdot \vec{\mu}_{ZPL}/\hbar$ . We emphasize

*Chapter 6: Diamond-based nanophotonic devices*

---

here that since the cavity mode only couples to the ZPL, we use the effective dipole moment of that transition only. Inserting these expressions into Equation 6.4 and using the fact that  $\epsilon \int |\vec{E}(\vec{x})|^2 dV = \hbar\omega$ , we recover the expression for the Purcell factor given in Equation 6.2.

We note here that there are several alternative definitions of the Purcell factor that might also be relevant here. One can also consider the lifetime change relative to emission into bulk diamond or free space, in which case the index  $n$  in Equation 6.2 should be 2.4 or 1, respectively. Another quantity is the enhancement of the ZPL emission into the cavity relative to the ZPL emission when the NV is decoupled from the cavity. This is given by  $P' = P/\xi$ , and a useful quantity when comparing the Purcell enhancement to other cavity QED systems where the emitter has a single decay channel. In other words, it gives a better comparison for the quality of the emitter-cavity coupling without factoring in the internal imperfections of the emitter itself, and is the quantity usually quoted in the literature. It is also the relevant quantity for estimating the enhancement of the ZPL photon rate from the cavity compared to, say, bulk diamond.

As explained above, in order to radiatively broaden the NV center through Purcell enhancement to overcome spectral diffusion, we require that  $P \gg \frac{\Gamma}{\gamma}$ , or  $P' \gg \frac{1}{\xi} \frac{\Gamma}{\gamma}$ , where  $\Gamma$  is the extrinsically broadened linewidth. From Equation 6.2, we see that to obtain a large Purcell factor, we need a large  $Q$  and a small mode volume. This can be achieved using photonic crystal cavities, where the mode volume can be designed to be  $\sim (\lambda/n)^3$ . Then, for a NV center with  $\Gamma \sim 100$  MHz, a cavity with a  $Q$  of  $\sim 3000$  is required. We now discuss some directions for the physical implementation

of such cavities in diamond.

### 6.3 Diamond-based nanophotonic devices

Over the past several decades, a large range of techniques have been developed for the fabrication of nanoscale devices in semiconductor materials ranging from silicon-based materials to III-V compounds such as gallium arsenide [70, 122]. While many of these techniques can be transferred to the fabrication of diamond, one major difference between diamond and most semiconductor materials presents a significant challenge to the fabrication of nanoscale devices for confining light. Because of the large lattice mismatch of diamond with most other crystalline materials, it is not possible to grow high quality thin films of single crystal diamond on top of a different substrate. This means that we cannot take advantage of the index mismatch between the device and substrate to confine light through total internal reflection. Here, we will briefly describe two methods for creating diamond-based nanophotonic devices by either creating a thin film that is placed on a substrate, or directly fabricating suspended structures on the surface of a bulk diamond sample.

While the methods described below can be used to make a variety of structures for different applications ranging from optomechanics to frequency comb generation, we focus here on the implementation of 1D waveguides and photonic crystals. These structures have been studied extensively and there exists a large body of work on their operating principles and design [123, 124, 125], so we will not go into detail on this topic here. Briefly, a photonic crystal cavity in a 1D waveguide geometry consists of a periodic structure along part of a waveguide with some perturbation or defect that

leads to localization of light. A completely regular and periodic lattice defines a Bragg structure with a gap in the band structure such that light with frequency within that gap cannot propagate. By tapering some parameter along the waveguide, such as the lattice constant or the dimensions of the structure inside each unit cell, we define a defect within the Bragg structure. With the proper design parameters, we can obtain a photonic crystal cavity with large  $Q$  and mode volume on the order of  $(\lambda/n)^3$ . We note here that the  $Q$  in this case depends on the design, fabrication, and material imperfections of the device. The design of the structure determines, for example, how much light from the cavity is either scattered or leaked into the waveguide. While light with well defined wavevectors can propagate without loss in a perfectly periodic structure, the introduction of a perturbation generally couples modes with different wavevectors, leading to scattering into free-space and other modes of the structure. At the same time, if the cavity mode extends to the ends of the Bragg structure, it can also leak out into the waveguide. Both of these mechanisms decrease the  $Q$  of the cavity. While we generally try to minimize scattering by introducing a gradual tapering, leakage into the waveguide can ultimately be desirable for collecting light from the cavity. Of course, fabrication imperfections can introduce deviations from the intended design, both by modifying the dimensions of the structure and introducing surface roughness.

The first method for fabricating diamond-based photonic crystal cavities begins with a bulk diamond membrane that has been mechanically polished to 10-30  $\mu\text{m}$  in thickness that is placed on a Si substrate. The membrane is thinned down using a deep reactive ion etch (RIE) in an inductively coupled plasma (ICP) of oxygen to the

device thickness, which is on the order of a few hundred nm. Devices are then defined on these thin films by e-beam lithography (EBL) using hydrogen silsesquioxane (HSQ) resist, which forms a mask that is transferred into the diamond film during another RIE etching step. Finally, the diamond structures are suspended by an isotropic RIE step that undercuts the Si substrate beneath the devices. Using such devices, we have observed enhancement of the ZPL fluorescence by a factor of 7. This work is described in detail in [126], and similar techniques have been used to create 2D diamond photonic crystal structures in [121].

The method described above has the drawback that, since the membranes are mechanically polished, there is often a gradient in the thickness, which transfers to the thin film. This means that only a small region of the devices that are made using the film has the desired thickness and wavelength. In addition, the thin films are difficult to handle and post-process. We have developed a second technique for scalable fabrication of nanophotonic structures that involves undercut structures suspended above the surface of bulk diamond. This is achieved using a technique described in [127], where the diamond is placed inside a faraday cage during RIE so that the ions are redirected and impinge on the surface at an angle. As a result, instead of etching the diamond in the direction perpendicular to the surface, it undercuts the material beneath the mask from two directions, resulting in suspended structures with a triangular cross-section that are suspended from or supported by anchors, as shown in Figure 6.2b. As shown in [127], we can make a variety of devices ranging from ring resonators to cantilevers using this method. We have fabricated 1D photonic crystal cavities using this method by etching an array of holes with tapered aspect ratios

along the waveguide, again using HSQ as an EBL defined mask, as shown in Figure 6.2. We can characterize these cavities using by coupling a broadband light source into the waveguide through a notch at one end and collecting the transmitted light that is scattered from a notch at the other end. An example of such a transmission spectrum is shown in Figure 6.2. Cavity resonances can be seen near the dielectric band edge with Q's of more than 3000.

One challenge of using such monolithic cavity designs is alignment of the NV center position with the cavity field. Thus far, our suspended devices have been made from a surface containing a layer of randomly positioned NV centers introduced by implantation, as described in Chapter 5. Therefore, we cannot precisely control the position of NV centers in the structure, and must rely on finding a device with an appropriately positioned NV center by chance. Eventually, more deterministic methods of introducing NV centers, such as implantation through a mask or AFM tip [128, 129], can be used to increase the yield of usable devices. However, for now, we increase the probability of optimally positioning NV centers in devices using another design that involves hybrid structures where the cavity is created separately from the diamond waveguide. Starting with a bulk diamond sample that has been implanted with a surface layer of NV centers, we define 1D waveguide structures using EBL with PMMA as a resist. After developing the resist, the mask pattern is transferred to alumina using a sputtering and liftoff process. The alumina-masked sample is then etched using the angled RIE technique described above, resulting in solid, suspended 1D waveguides with a triangular cross section, suspended  $\sim 1 \mu\text{m}$  above the etched diamond surface. The sample is then re-annealed to repair damage

Chapter 6: Diamond-based nanophotonic devices

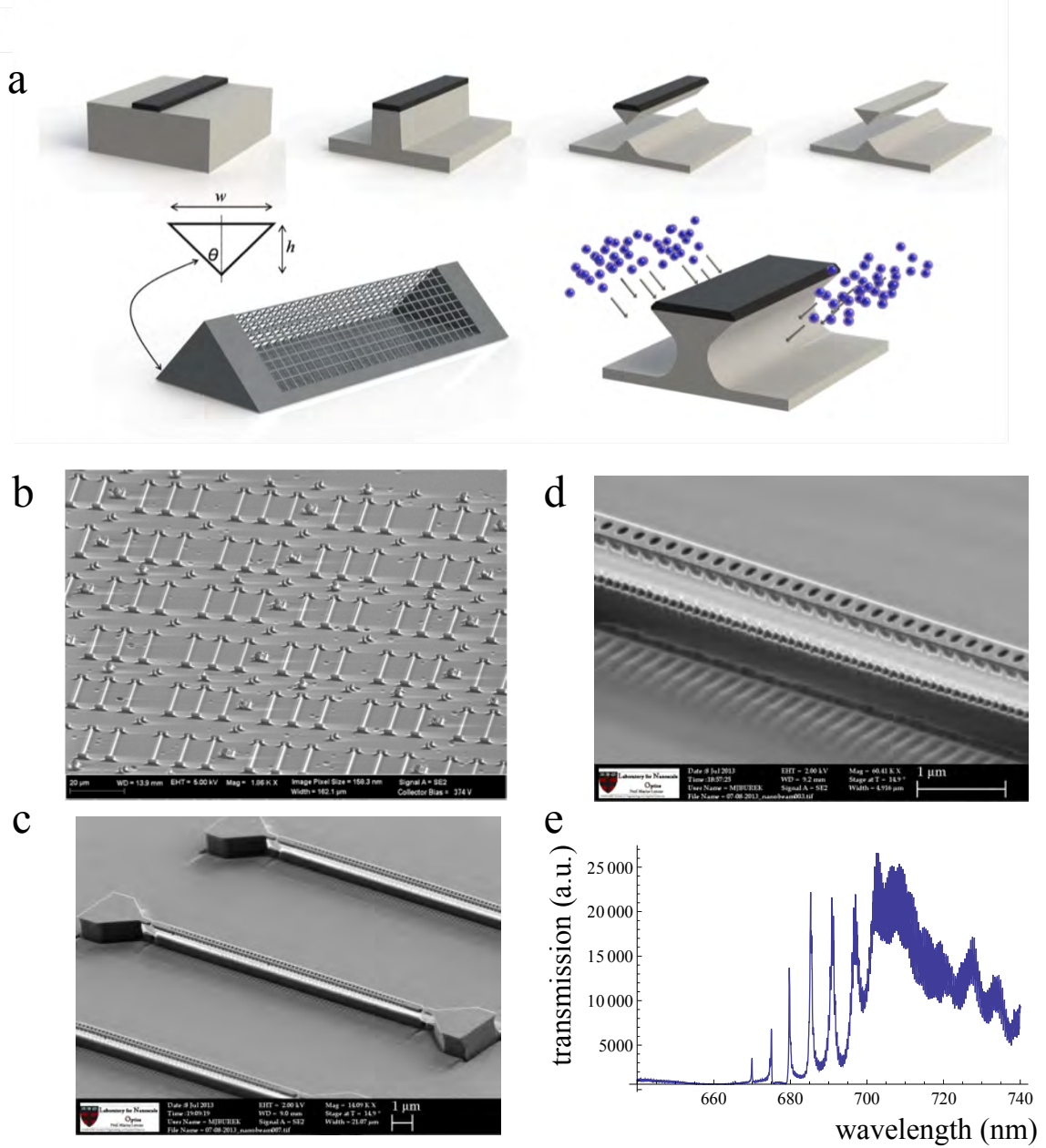


Figure 6.2: Suspended diamond-based nanophotonic structures. **a.** Procedure for angled RIE etching. A mask is defined using EBL on the surface of the diamond. A top-down etching step performed, followed by an angle-etching step where the diamond is placed in the center of a machined aluminum faraday cage shown on the bottom left. The mask is removed, leaving a suspended structure attached at both ends to anchors (not shown) **b.** SEM image of a large array of  $\sim 1000$  angle-etched waveguides. **c-d.** SEM images of photonic crystal cavities formed in 1D waveguides. **e.** Transmission spectrum of one such device.

introduced during the etching process, as described in the next section. We then characterize the randomly positioned NV centers inside the waveguides and take note of their position relative to alignment markers also etched onto the surface. We then spin a 2  $\mu\text{m}$  thick layer of PMMA to cover the structures on the surface and use EBL to define perpendicular slabs along the waveguide. By tapering the lattice constant of this Bragg structure composed of PMMA slabs, we can define a cavity with simulated Q's of up to  $5 \times 10^4$ . Q's of several thousand have been demonstrated in fabricated structures, which are shown in Figure 6.3. Since these cavities can be made anywhere along the waveguide, we can center them around the position of the previously identified NV centers. This is the main advantage of these hybrid PMMA-diamond structures. One drawback of these devices is that they are somewhat more fragile compared to all-diamond structures, and the PMMA slabs can be easily destroyed in during SEM imaging or if there is a sudden pressure change, for example while pumping out the cryostat for low-temperature characterization.

## 6.4 Spectral properties of NV centers inside nanoscale structures

In Chapter 5, we demonstrated the creation of optically coherent NV centers in a surface layer through implantation. This is the starting material used for hybrid cavity devices. However, we find that the NV centers inside the nanoscale devices are generally less spectrally stable than those inside bulk diamond. The narrowest extrinsically broadened linewidths are on the order of a few GHz, while the single



scan linewidths can be less than 100 MHz. In addition, our 1D waveguides have to be re-annealed following a similar recipe as Figure 5.1, without which the NVs are generally not photostable. There is also indication that the photostability and spectral stability are improved by smoother etched surfaces or additional cleaning and termination steps such as soaking the samples in a piranha solution. All of these effects point toward surface states as the source of charge fluctuations in the environment that lead to spectral diffusion. There is ongoing work to identify the potential chemical composition and structure of the etched surfaces. However, this is generally quite challenging given the small dimensions of our structures, which limit the surface area from which signal can be collected.

## 6.5 Purcell enhancement from a coupled NV-cavity system

While many improvements to our devices remain to be made, we present here a preliminary measurement demonstrating the Purcell enhancement of a NV center's ZPL emission by a nanoscale cavity. These measurements were made on a NV center with a 3 GHz linewidth inside a hybrid cavity with a Q of  $\sim 600$ .

In addition to spatial alignment of the NV center to the cavity, it must also spectrally overlap with the cavity mode. Here, we note that the NV center linewidth, even with a spectral diffusion of several GHz, is much less than the cavity linewidth, which is on the order of 100 GHz. In other words, we operate in the bad cavity regime, where  $\kappa \gg g \gg \Gamma$ . However, due to variations in the fabrication process,

the cavity can still be far detuned from the NV center. Therefore, to estimate the Purcell enhancement based on the lifetime difference when the NV is on and off-resonance with the cavity, we need to be able to tune the cavity mode frequency. To do this, we use a combination of two techniques. The first method uses a  $O_2$  plasma etcher (Technics, Model 220) to remove a layer of material from the structure [126]. This tunes the cavity resonance to lower wavelengths because more of the cavity field resides in air than before and therefore has a higher energy. We have been able to achieve a wavelength shift of  $\sim 15$  nm without significant degradation in the Q factor using this method. Complementary to this blue tuning process, we can also red tune the cavity resonance by depositing neon gas on the structure when it has been cooled down inside the cryostat [130]. We note here that gas deposition is a common method for tuning photonic crystal cavities, and a tuning range of  $\sim 23$  nm was observed in [126]. However, it is somewhat less effective for our hybrid structures since the high aspect ratio of the PMMA slabs prevent the diffusion of gas onto the diamond waveguide, where the field is concentrated. Despite this, we have occasionally been able to obtain tuning ranges of  $\sim 6$  nm.

To measure the change in lifetime when the NV center becomes coupled with the cavity, we first tune the cavity resonance using plasma etching until it is to the blue of the NV center's ZPL. We then gradually red tune the cavity onto resonance with the ZPL while measuring the lifetime using a filtered supercontinuum laser (NKT photonics, SuperK EXTREME) as a pulsed laser source around 532 nm. As shown in Figure 6.3, the lifetime decreases from 18.5 ns when the cavity is completely off resonant to 11.6 ns when the cavity is tuned to the ZPL. This gives a Purcell factor of

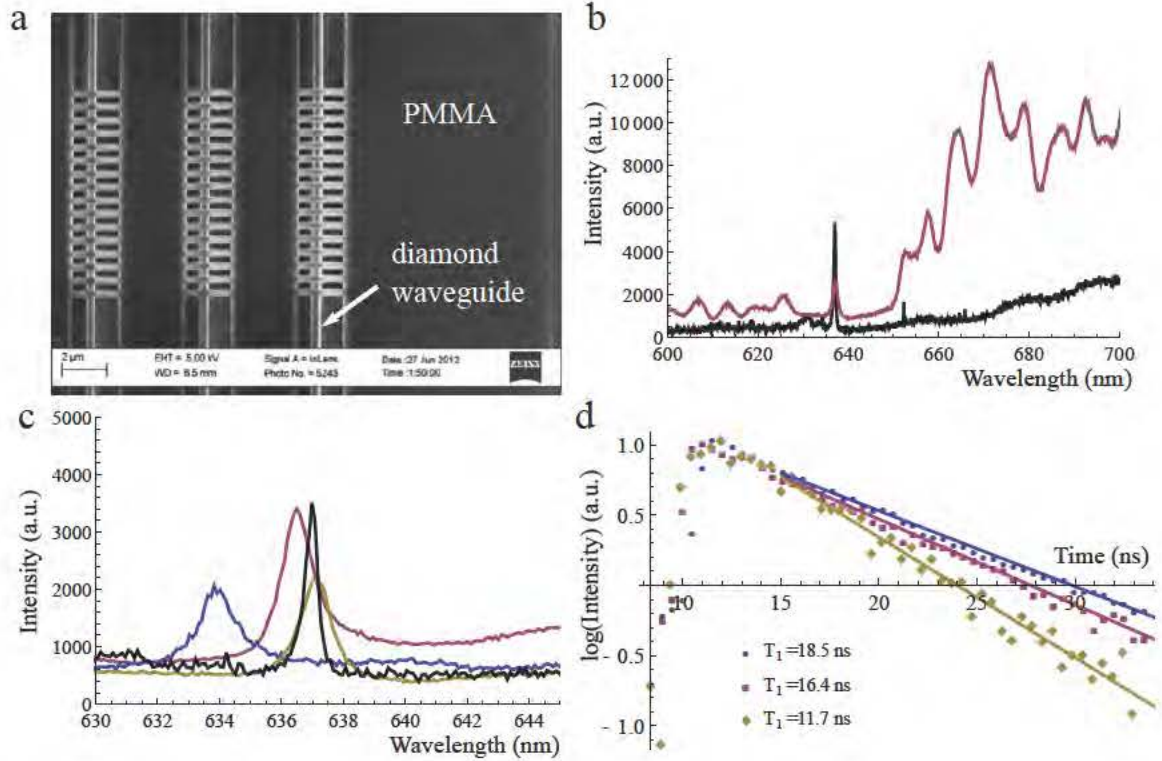


Figure 6.3: Purcell enhancement of the NV center ZPL emission using hybrid photonic crystal cavities. **a.** SEM image of hybrid diamond-PMMA cavities. Visible are the top surface of the suspended triangular beams, the top of the the PMMA layer and slabs, along with the exposed diamond surface underneath. **b.** Transmission spectrum of hybrid cavity (magenta) and emission spectrum of NV center (black). The spectra have been scaled relative to each other to fit on the same scale. **c.** Zoomed in spectra showing ZPL of NV center (black) and cavity resonance tuned to three different frequencies (blue, magenta, and yellow). **d.** Lifetime measurements corresponding to the detunings in c., taken by exciting the NV center with a pulsed laser and collecting the PSB emission.

$P = 0.59$ , or a ZPL enhancement of  $P' = 20$  for  $\xi = 0.03$ . We emphasize here that this enhancement factor implies that the ZPL emission is now  $\sim 40\%$  of the total emission from the NV center. However, the lifetime limited linewidth is almost unchanged, and a much larger Purcell factor is needed to overcome the spectral diffusion, which in this case is a factor of  $\Gamma/\gamma \sim 200$ .

## Chapter 7

# Conclusions and outlook

Finding an ideal system for implementing robust, scalable technologies that make use of quantum mechanics is an exciting challenging. Such a system must satisfy a set of seemingly contradictory requirements. On the one hand, it must be complex enough such that there are enough degrees of freedom for us to store and manipulate a large amount of quantum information. On the other hand, more complexity means that it becomes harder to understand and control the system. Related to this idea, the system must be sufficiently isolated from the environment to be able to store quantum information for long periods of time, but must also interact with certain aspects of the outside world so that it can be controlled, measured, and interfaced with other systems. Generally, in order to develop useful quantum technologies, we need to understand the complexities of the system we are interested in, turn as many of them as possible into useful resources, and suppress any detrimental effects that remain.

The work presented in this thesis illustrates our efforts to achieve this goal with the

NV center system. While the NV center at room temperature is already a promising system for metrology and quantum information, we take advantage of the additional degrees of freedom offered by its coherent optical properties. This allows us to expand the NV center beyond a local quantum register by interfacing it with photons and other remote qubits. Of course, this requires a new level of understanding and control of the optical transitions, which we presented in Chapter 2. As another example, the nuclear spin bath surrounding the NV center is a complex system that affects the spin coherence of the NV center through the hyperfine interaction. However, it has been shown in many experiments that the nuclear spins can also be used as a powerful resource [65, 131]. Therefore, efforts to better understand and control the nuclear spin bath, such as the one described in Chapter 4, are important to fully take advantage of complexity in the NV center spin system. In addition, while the NV center's spin degree of freedom is affected by the magnetic environment, its orbital degree of freedom interacts with the equally complex electronic environment. This is evident in the spectral diffusion of the excited states, which is an effect that we work to understand and suppress in Chapter 5.

Initiated by the work presented in Chapter 3, there has been tremendous progress in using optical photons to connect remote NV centers. Future work will explore the possibility of combining the few-qubit local spin register with the resource of remote entanglement through, for example, teleportation of quantum information between remote, long-lived nuclear spin memories. Distribution of quantum information by teleportation has been demonstrated in several different physical systems [132, 16, 133]. However, remote teleportation over long distances is an outstanding

challenge with solid state systems, which, in the long run, offers the possibility of implementing more scalable local quantum nodes. In particular, one major factor in determining the ultimate bandwidth and fidelity of a remote quantum channel is the efficiency with which single photons can be made to interact with the stationary qubits and then extracted into, for example, an optical fiber. Current photon collection efficiencies and entanglement rates may be sufficient for proof-of-principle experiments, but certainly must be greatly improved for the implementation of practical quantum networks. The work described in Chapters 5 and 6 begins to address this issue. The spectral stability of NV centers is an important factor in determining the repetition rate of experiments requiring indistinguishable optical photons, such as remote entanglement and teleportation. The availability of NV centers with lifetime-limited linewidths would eliminate the need for active stabilization and post-selection of the transition frequency in future experiments. Cavity QED has been used to enhance the interaction of photons with atomic systems and improve their collection efficiency, leading to demonstrations of quantum teleportation with high fidelity and success rates [132]. Diamond-based nanophotonics offers the possibility of achieving efficient photonic quantum devices in a solid state system.

The work described in this thesis can also be extended for use with a variety of other systems. For example, a number of alternative defects in solid state materials are being explored, with many of them showing great promise and potential improvements over the NV center in certain aspects. One such system is the silicon-vacancy (SiV) in diamond, where an impressive degree of spectral stability has been observed in the optical transitions [134, 135]. The theoretical description of the SiV system has

many parallels with that of the NV center, as presented in Section 2.2. While it is not yet clear whether or not the SiV center has spin properties that are useful for metrology or quantum information, it shows great promise in other applications such as single-photon sources, whose efficiency could benefit greatly from incorporation with nanophotonic structures such as those described in Chapter 6.

Finally, future quantum technologies will most likely be implemented with a combination of several types of physical systems, each with its own strengths and weaknesses. There are already many theoretical proposals and experimental demonstrations of interfacing NV centers with other quantum devices [136, 137]. Most of these demonstrations make use of the NV center’s unique spin properties, effectively turning its interaction with the magnetic environment from a detriment into a resource. Analogous to this, an potential direction for future exploration would be to take advantage of the NV center’s optical transitions to interface it with other systems. Thus far, we have treated the strain and electric field sensitivity of the NV center’s excited states as a detrimental effect. However, these properties can also be used to, for example, couple multiple nearby NV centers for the purpose of investigating interesting collective effects or scaling up the local quantum register. In addition, they allow for interactions between the NV center and other structures that can modify its local strain or electric field, such as mechanical oscillators and superconducting circuits. The strength of these interactions can potentially be much stronger than the magnetic coupling using the ground state of the NV center. Combined with the ability to communicate information with remote systems through optical photons, the NV center becomes a quantum system that not only has uniquely attractive proper-



*Chapter 7: Conclusions and outlook*

---

ties as an isolated system, but can also be made to interact with other systems in a controlled manner. Therefore, the ideas and techniques developed in this thesis will enable us to use the optical properties of the NV center as a powerful resource for building complex and useful quantum technologies.

# Appendix A

## Supporting material for Chapter 3

### A.1 Calculation of entanglement fidelity

To estimate the entanglement fidelity, we first use the conditional measurement shown in Figure 3.4a,b to determine diagonal elements of the spin-photon density matrix in the  $|\sigma_{\pm}\rangle, |\pm 1\rangle$  basis. Since  $\sigma_{\pm}$  photons are emitted with equal probability (see SI), we find  $\rho_{\sigma_+ -1, \sigma_+ -1} = \frac{1}{2}p_{-1|\sigma_+} = \frac{1}{2}(0.96 \pm 0.12)$ ,  $\rho_{\sigma_+ +1, \sigma_+ +1} = \frac{1}{2}(0.07 \pm 0.04)$ ,  $\rho_{\sigma_- -1, \sigma_- -1} = \frac{1}{2}(0.10 \pm 0.05)$ , and  $\rho_{\sigma_- +1, \sigma_- +1} = \frac{1}{2}(0.87 \pm 0.14)$ . To evaluate the off-diagonal elements, we rotate the measurement basis by projecting the photon to the  $|H\rangle$  or  $|V\rangle$  states and measuring the conditional probability of being in state  $|M\rangle$ , which is equal to  $|\pm\rangle$  for particular choices of  $\alpha$  (e.g.  $|+\rangle = |M\rangle|_{\alpha=0}$ ). The required diagonal matrix elements in the  $|H\rangle, |V\rangle, |\pm\rangle$  basis are then given by  $\rho_{V+, V+} = \frac{1}{2}p_{M|V}(\alpha = 0)$ , and similarly for  $\rho_{H+, H+}$ ,  $\rho_{H-, H-}$ , and  $\rho_{V-, V-}$ . We model the experimentally measured conditional probabilities with the forms  $p_{M|H} = (b_H + a_H \cos \alpha) / 2$  and  $p_{M|V} = (b_V - a_V \cos \alpha) / 2$ , where  $b_{H,V}$  are the offsets of the oscillations and

## Appendix A: Supporting material for Chapter 3

---

$a_{H,V}$  are their amplitudes. Using a simultaneous fit to the data in Figure 3.4c, d that constrains the frequency to be the Zeeman splitting, we obtain the values  $\rho_{V+,V+} - \rho_{V-,V-} = a_V/2 = \frac{1}{2}(0.53 \pm 0.16)$ ,  $\rho_{H-,H-} - \rho_{H+,H+} = a_H/2 = \frac{1}{2}(0.58 \pm 0.10)$ . The information obtained is sufficient to provide a lower bound for the entanglement fidelity. Using the analysis in [22]:

$$F \geq \frac{1}{2}(\rho_{\sigma_+ -1, \sigma_+ -1} + \rho_{\sigma_- +1, \sigma_- +1} - 2\sqrt{\rho_{\sigma_+ +1, \sigma_+ +1} \rho_{\sigma_- -1, \sigma_- -1}} + \rho_{V+,V+} - \rho_{V-,V-} + \rho_{H-,H-} - \rho_{H+,H+})$$

we find  $F \geq 0.69 \pm 0.068$ . This analysis agrees with the results of an independent maximum likelihood analysis described in the SI, which yields a near Gaussian probability distribution for a lower bound on the fidelity with  $F \geq 0.70 \pm 0.070$ .

## A.2 Experimental details

### A.2.1 Overview of experimental setup

The experiments in Chapter 3 are performed using a natural bulk diamond sample kept below 7 K in a Janis ST-500 Cryostat. Resonant excitation of the readout and entanglement generation transitions are done using two external cavity diode lasers. To overcome the main experimental challenge of ensuring sufficient signal to noise of the detected ZPL emission, we eliminate background from laser light reflected off the diamond surface by creating an isolated excitation  $\pi$  pulse using two cascaded waveguide modulators. This excitation pulse is sent through a quarter-wave plate that is fixed during all experimental runs to produce the circular polarization that most efficiently excites the NV to the  $|A_2\rangle$  state. We note that, since our measurements are

*Appendix A: Supporting material for Chapter 3*

---

conditioned on the detection of an emitted photon, optical  $\pi$  pulse imperfections only affect the efficiency of the entanglement generation and not the measured fidelity. In the collection path, the ZPL is sent to a polarization analysis setup consisting of a half-wave plate and a polarizing beamsplitter for photon state selection. It then passes through a narrow frequency filter before being detected by a low dark count APD. We use a waveguide based electro-optical modulator before the APD to further reduce reflections of the excitation pulse and suppress detector afterpulsing. Special care is taken to minimize reflections during the measurement window to around the dark count level of the detector.

Addressing of the  $|0\rangle \leftrightarrow |\pm 1\rangle$  microwave transitions is carried out using a 15  $\mu\text{m}$  copper wire attached to the diamond. For simultaneous addressing, two microwave fields generated by mixing the difference frequency of the two transitions with their average frequency are separated using bandpass filters, individually attenuated, and recombined to balance their power. Low shot-to-shot noise in the microwave fields' relative phase is crucial. This is achieved by triggering all timing-sensitive channels from one output event of a controller device that produces the entanglement generation and conditioned readout sequences. Timing information of both ZPL and PSB photons are collected by combining them at the input of a time-tagged-single-photon-counting device.

Given an experiment repetition rate of  $\sim 100$  kHz and an entanglement generation success probability of  $p \sim 10^{-6}$ , we then detect on average one signal photon every few seconds. Since the microwave  $\pi$  pulses used for population transfer to the  $|0\rangle$  state are nearly perfect and about 100 repetitions are required for reliable spin

### *Appendix A: Supporting material for Chapter 3*

---

state determination, roughly 24 hours of data taking were required for each of the four photon polarizations measured. Overall, characterization, calibration, and data acquisition for a given NV center were performed over a roughly two month period. The overall measurement time for each individual NV center is limited by the long term mechanical stability of the setup.

#### **A.2.2 Optical setup**

Optical access to individual NV centers is facilitated with a Nikon 0.95 NA Plan-Apo microscope objective that is held inside vacuum with a bellow structure that allows the objective to be moved relative to the sample. Our microscope contains two excitation channels and two collection channels. The NV is off-resonantly excited and spin polarized using a doubled YAG laser (532 nm Coherent Compass 315M-100) modulated with an acousto-optical modulator (Isomet 1250C-848). Resonant optical pumping is carried out with two external cavity grating lasers. A New Focus Velocity TLB 6304 laser operating at 637.199 nm and locked to a Fabry-Perot cavity (Atrix Management S A CC - 3.0GHz - 200) is used for the readout transitions ( $\sim 4 \mu\text{W}$  before objective), while a second laser (Atrix Management S A ECLD-0638-022) operating at 637.189 nm is used for resonant optical pumping of the entanglement generation transition ( $\sim 100 \mu\text{W}$  before objective). Both lasers are modulated with acousto-optical modulators (Crystal Tech 3080-122). In addition, a high fidelity excitation pulse (2 ns 3dB width and  $> 50$  dB extinction in 4 ns from peak) is generated from the 637.189 nm laser using two waveguide modulators in cascade (Guided Color Technologies), each controlled by an 800 MHz arbitrary waveform generator (Ana-

### *Appendix A: Supporting material for Chapter 3*

---

logic Polynomial Waveform Synthesizer 2045). Extinction of the excitation pulse is critical because we use the relatively long lifetime of the NV center to separate the emission from the shorter (2ns) laser reflection photons.

Phonon-sideband emission from the NV is separated by dichroic filters from the 532 nm excitation path (Semrock LPD01-532RS-25) and ZPL path (Semrock Di01-R635-25x35) before being filtered to remove any leakage or dominant raman lines (2x Semrock NF01-633U-25, Semrock LP01-633RS-25). It is then coupled into a single mode fiber and sent to a high quantum efficiency APD (SPCM ARQ-15-FC). The ZPL collection path is separated from the resonant excitation path by a non-polarizing beam splitter, and emission from the NV is sent to a polarization analysis setup consisting of a HWP and a PBS. The emission is filtered by two narrow frequency filters (custom Andover 1 nm bandpass around 638 nm, Semrock FF01-640/14-25) and detected by a low-dark count APD (Micro-Photon-Devices, PDM Series). We use a third waveguide based E-O modulator (EOSpace, driven by Stanford Research Systems DG645 delay generator) before the detector to reduce the number of reflected photons from the excitation pulse and suppress afterpulsing of the detector.

#### **A.2.3 Microwave control**

The two microwave transitions are addressed individually by separate oscillators: a HP 8350B sweep oscillator with 83525A RF plugin tuned to 2.9387 GHz and an Agilent 83732B synthesizer tuned to 2.8174 GHz. For simultaneous addressing, a 60.85 MHz waveform generated by a high speed Tek 710 AWG is mixed using a Minicircuits ZFM-15 mixer with the RF field generated from the Agilent synthesizer at 2.87875

*Appendix A: Supporting material for Chapter 3*

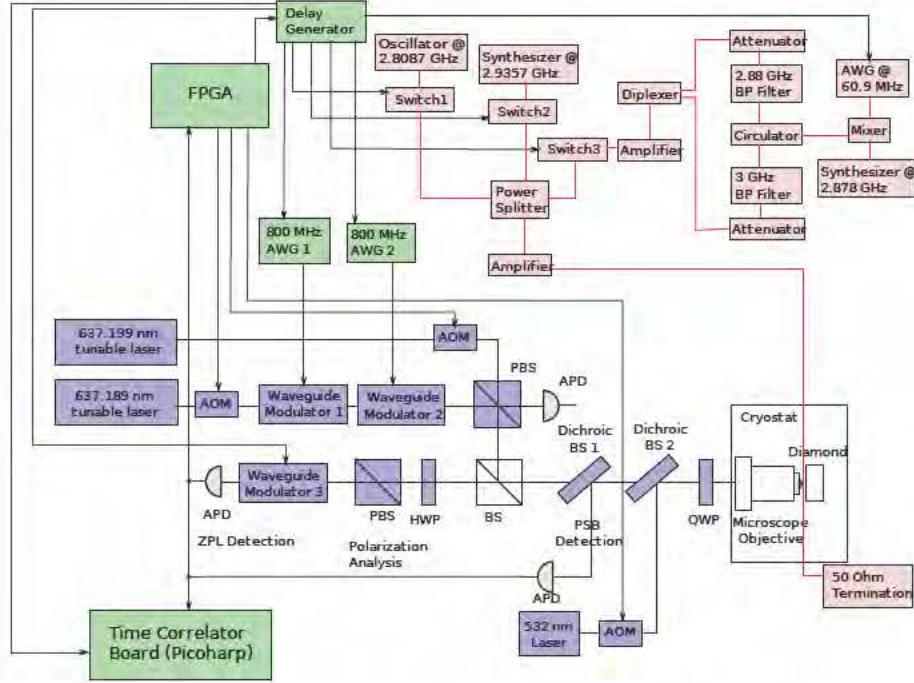


**Figure A.1: Experimental Setup.** The setup is shown in three functional groups. The optical setup is shown in blue and gray. In green are the control electronics and the electrical pulses that are generated. A green arrowed line indicates a pulse being generated by the source device and sent to the entity indicated by the arrow. For example the FPGA generates the pulse that drives the AOM for 637.199 nm readout laser. The microwave components and their connections are shown in red.

GHz. To balance the power of the two microwave frequencies of the simultaneous field, they are first separated using two bandpass filters with 120 MHz bandwidth around 2.8 GHz and 3.0 GHz (Reactel 5C7-2800-120S11 and 5C7-3000-120S11). They are then recombined using a diplexer around the same frequencies (Reactel 2DP7-2800/3000-X120S11) after being individually attenuated (Minicircuits ZX76-15R5-PP-S+) and re-amplified (Minicircuits ZX-60-6013E+). The measured variance in the relative phase between two frequencies of the simultaneous field is below 0.19 radians. Fast microwave switches (Minicircuits ZASWA-2-50DR+, Custom Microwave Components

S0947A-C2) are used for time shaping of microwave pulses. All separate channels are combined and sent to a 10 W solid state amplifier (Ophir 530324-002) before the copper wire.

### **A.2.4 Experiment control and data acquisition**

Experimental flow is controlled by a NI-7833R FPGA based intelligent DAQ device programmed to run the entanglement generation sequence and switch to the readout sequence within three clock cycles (75ns) upon the detection of a ZPL photon. Time of arrival information of photons on both PSB and ZPL channels are collected by passively combining the output of the two APDs to the input of a time-tagged-single-photon-counting device (PicoHarp 300). The device is configured to record the time of arrival of all detection events relative to a trigger event marking the beginning of the experimental sequence. Further processing of the data is done after each experimental run to determine the number of relevant ZPL and readout events. All channels / events that are timing-sensitive (e.g. trigger to the AWG or trigger to the timing board) are generated from a single output event of the FPGA device that triggers the Stanford DG645 signal generators running in burst mode, which have low channel-to-channel and low trigger-to-output jitter.

An additional multi- function DAQ device from NI is used to find and characterize the NVs. It is also used to record a second electronic copy of the photon arrival event on the PSB channel to track the position and frequency drift of the NV/ cryostat/laser system while the entanglement experiment is running.

Finally, we point out that the overall time required for finding and characterizing



### *Appendix A: Supporting material for Chapter 3*

---

a low-strain NV is several weeks. Combined with the four day-long data acquisition runs for entanglement verification, the amount of data we are able to take for the same NV becomes limited by the long term stability of our setup. Further improving the robustness of the setup and our ability to locate particular NV's over long time periods will be crucial for future experiments.

## **A.3 Spin readout**

Spin readout is achieved through resonant laser excitation tuned to the  $|0\rangle \leftrightarrow |E_y\rangle$  transition [40]. As the  $|0\rangle \leftrightarrow |E_y\rangle$  transition is cycling for low strain and is isolated in frequency from other transitions the fluorescence collected in the presence of the resonant laser field should be proportional to the population in the  $|0\rangle$  state. However, the fluorescence levels measured for different spin states may depend on the complex dynamics associated with the singlet state, imperfections of the cycling transition, photoionization, and spatial stability of the measurement setup. In order to accurately calibrate our spin measurements, we use a procedure that involves the conditional preparation of spin states. In the following section, we first describe the conventional spin measurement procedure and then compare it to our conditional readout scheme.

Figure A.3(a) shows microwave Rabi oscillations detected using the conventional resonant readout scheme. Following a polarization step carried out with a green laser, a microwave pulse of varying length and resonant to the  $|0\rangle \leftrightarrow |1\rangle$  transition is applied and the resulting state is read out using the resonant excitation. In an ideal preparation and readout scenario, the  $|0\rangle$  state would be bright while the  $|\pm 1\rangle$  states would be completely dark. The high level of fluorescence achieved for the  $|0\rangle$  state is

*Appendix A: Supporting material for Chapter 3*

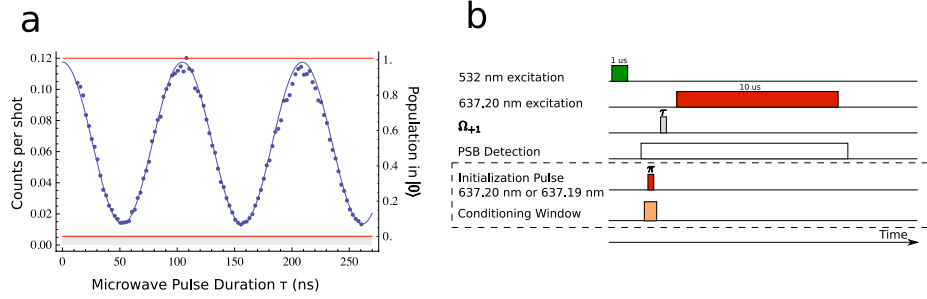


**Figure A.2: Spin readout via resonant excitation** **a** Microwave Rabi oscillations (in blue) recorded using the pulse sequence given in (b) without conditioning. Left vertical axis shows the average number of counts received for a particular length of microwave pulse duration ( $\tau$ ). Right vertical axis shows the normalized population in the  $|0\rangle$  state for the same pulse duration. The red lines are maximum and minimum readout levels obtained using the conditioned readout technique shown in (b) and described in the text. **b** Pulse sequence used for part (a). In the unconditioned case, 532 nm light is turned on for 1  $\mu$ s to polarize the electronic spin to  $|0\rangle$  state. After 6  $\mu$ s, a microwave pulse resonant to the  $|0\rangle \leftrightarrow |+1\rangle$  of varying duration is applied. Finally a 10  $\mu$ s light pulse resonant to the  $|0\rangle \leftrightarrow |E_y\rangle$  transition is turned on 1  $\mu$ s after the microwave pulse and counts in the PSB are recorded in this interval. Additional pulses used for conditioned readout are boxed, including a resonant optical  $\pi$  pulse tuned to the  $|0\rangle \leftrightarrow |E_y\rangle$  or  $|\pm\rangle \leftrightarrow |A_2\rangle$  transition. Only events where a PSB photon is received within a 20 ns window around this pulse are kept, thus conditioning the readout procedure on a fluorescent decay from the NV.

limited by the branching ratio between the  $|E_y\rangle \rightarrow |0\rangle$  and  $|E_y\rangle \rightarrow |\pm 1\rangle$  transitions ( $\sim 99\%$  as measured below) and the collection efficiency to about 0.11 counts per shot. Thus multiple repetitions of the experiment are needed to build up enough statistics for an accurate estimation of the initial state. When the NV center is nominally prepared in the  $|+1\rangle$  state, we observe counts above the background level, which may be due to imperfect spin polarization or additional fluorescence from the  $|+1\rangle$  state.

To characterize these effects further, we record time traces of the fluorescence during the resonant readout stage where the state is initialized either in  $|0\rangle$  or  $|1\rangle$  in the same way as the Rabi experiment (Figure A.3(b)). These are then compared to a

Appendix A: Supporting material for Chapter 3

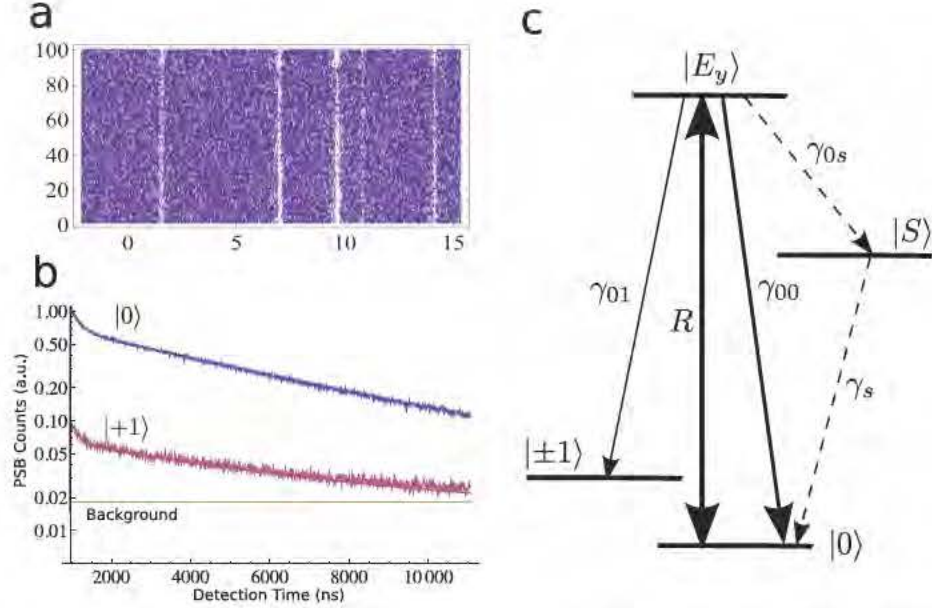


Figure A.3: **Stability and dynamics of optical transitions** a One hundred successive scans of the NV spectrum shown in Figure 3.2(b) of the main text. Each scan taken over  $\sim 10$  seconds, demonstrating the spectral stability of the NV center over long time scales. Spectral lines shown here and in Figure 3.2b of the main text have widths larger than 100 MHz due to power broadening. b Histograms showing time traces of fluorescence as recorded in the PSB following spin initialization to either the  $|0\rangle$  (red) or  $|1\rangle$  (blue) state. Solid lines show simulated fluorescence from the NV using the model shown in (c) and described in the text. Two other similar data sets at different laser powers were used to determine the branching ratio of  $|E_y\rangle$  to  $|\pm 1\rangle$  and the spin polarization. c Model used to simulate the dynamics of optical transitions leading to fluorescence time traces shown in (b).  $R$  gives the optical pumping rate of the readout transition.  $\gamma_{00}$  and  $\gamma_{01}$  are decay rates to the  $|0\rangle$  and  $|\pm 1\rangle$  states, respectively.  $\gamma_{0s}$  and  $\gamma_s$  are the non-radiative decay rates into and out of the metastable singlet state  $|S\rangle$ .

model of the NV center dynamics similar to the one discussed in [39] and illustrated in Figure A.3(c). The model involves the  $|0\rangle$  and  $|\pm 1\rangle$  ground states, the  $|E_y\rangle$  state, and a metastable singlet state  $|S\rangle$ . The branching ratios from  $|E_y\rangle$  state to  $|0\rangle$ ,  $|\pm 1\rangle$ , and  $|S\rangle$  are related to the decay rates  $\gamma_{00} = 1/12\text{ns}$ ,  $\gamma_{01}$ , and  $\gamma_{0s}$ , respectively.  $\gamma_{00}$  is determined by lifetime measurements, and the singlet decay rate to  $|0\rangle$  is set to

### *Appendix A: Supporting material for Chapter 3*

---

$\gamma_s = \gamma_{00}/33$ , as given in [39]. We then simulate the evolution of the system under a continuous optical pumping of the  $|0\rangle \rightarrow |E_y\rangle$  transition at a rate  $R$ , starting with some initial spin population for the two cases of initialization in  $|0\rangle$  or  $|1\rangle$ . To estimate the values of  $\gamma_{01}$ ,  $\gamma_{0s}$ ,  $R$ , and the spin polarization, these parameters are varied to fit the simulation to the data by eye. This was done for three different laser powers, and the data and simulation results for the medium power are shown in Figure A.3(b), which corresponds to conditions under which the Rabi curve in Figure A.3(a) were taken. Using this method, we estimate the branching ratio out of the system of  $m_s = 0$  states to be  $0.92 \pm 0.16\%$ , and the imperfection in spin preparation to be  $7.2 \pm 1.8\%$ . This imperfection could be either due to incomplete spin polarization or imperfect microwave pulses. The pulse error associated with a square pulse of finite Rabi frequency (around 10 MHz) is estimated to be about 3 %. The error is mostly due to the presence of the hyperfine interaction with the nuclear spin of  $^{14}\text{N}$  associated with the NV center[138]. We thus estimate the spin polarization after the green excitation to be  $96 \pm 1.9\%$ .

To directly calibrate our spin readout results and confirm that it is the imperfect spin preparation stage which reduces the contrast of the Rabi experiment, we perform two experiments in which we polarize the NV center by measurement and perform conditional spin readout. In the first experiment, a  $\pi$  pulse (initialization pulse) resonant to the  $|0\rangle \leftrightarrow |E_y\rangle$  transition is applied many lifetimes prior to microwave manipulation. By only analyzing events in which a photon has been detected in the PSB during the initialization pulse, we ensure that a photon has decayed from the  $|E_y\rangle$  state prior to microwave manipulation. The state should decay to the  $|0\rangle$  state with

*Appendix A: Supporting material for Chapter 3*

---

99 % probability, and given that the signal / noise of the trigger photon is roughly 280:1, the state should be prepared in  $|0\rangle$  with 99 % probability prior to microwave pulses. Subsequent measurement of the spin by a separate laser tuned to the same transition reveals  $0.13 \pm 0.025$  counts /shot if no microwave manipulation is carried out and  $0.0092 \pm 0.00054$  counts/shot if a microwave  $\pi$  pulse is applied resonant to the  $|0\rangle \leftrightarrow | +1\rangle$  transition. The ratio of the counts after subtracting the background of  $0.0057 \pm 0.0010$  counts/shot is accounted for by the expected pulse error. A second experiment was carried out where the initialization pulse was tuned resonant to the  $| +1\rangle \leftrightarrow |A_2\rangle$  transition. The detection of a photon in the PSB indicates that the state has been prepared in the  $|\pm 1\rangle$  manifold, and a subsequent readout process without any microwave manipulation yields the background level. We then conditionally measure the populations in the  $|\pm 1\rangle$  states by individually transferring their population back to  $|0\rangle$  state. We find that their population levels are roughly equal ( $0.059 \pm 0.0013$  counts/shot and  $0.061 \pm 0.0014$  counts/shot). Assuming that the PSB emission does not change the spin projection, this data indicates that the  $|A_2\rangle$  state decays with roughly equal probability to  $|\pm 1\rangle$  states.

We note that the readout levels achieved by the conditioned measurement procedure could in principle be different from the values obtained without conditioning. Although the difference is small for the NV center used in the current experiment, we have observed a significant difference for other NV centers. One possible source for this difference is photoionization of the  $NV^-$  to  $NV^0$ , in which case the NV center effectively goes dark. The detection of a PSB photon during the conditional calibration procedure described above ensures that the center is in the  $NV^-$  state for

### *Appendix A: Supporting material for Chapter 3*

---

that particular repetition of the experiment. The readout levels obtained using this procedure are then relevant for normalization of our entanglement verification data, which are similarly conditioned on the detection of a ZPL photon. On the other hand, if no such conditioning was performed, the calibration levels obtained would be reduced by the probability of ionizing the NV, and would not accurately correspond to our entanglement data. In addition, there are many other sources of noise that would have a similar effect, for example spectral instabilities of the laser - NV center system and mechanical vibrations that quickly misalign the system. These effects are slow compared to the repetition rate of our experiment, but short compared to the total data acquisition time and could generate a difference in the two spin readout methods. The NV center we work with has good long term spectral stability within a linewidth of  $\sim 100$  MHz (Figure A.3(a)), and we actively track the position of the NV by maximizing the fluorescence counts during the experiment. However, to completely eliminate the effect of possible instabilities, we normalize our measurements to the conditional calibration values. The population  $P$  in state  $|0\rangle$  for a given number of counts per repetition ( $C$ ) is then  $P = (C - c_B) / (C_M - c_B)$ , where  $c_B = 0.0057 \pm 0.0010$  counts/shot and  $c_M = 0.11 \pm 0.0022$  counts / shot correspond to the background and maximum calibration values, respectively.

In summary, we find that resonant excitation in combination with conditioning-based spin preparation is an exceptionally useful tool for spin readout of the NV center. Not only can we use it to extract information about populations in relatively few repetitions, but it allows us to fully characterize various procedures related to the spin properties of the NV center, for example spin polarization achieved or pulse

errors, with very few assumptions. In addition, the conditioned readout technique may be useful in probing other properties of the NV center such as blinking and spectral stability.

## A.4 Verification of polarization selection rules for $|A_2\rangle$ state

Figure 3.2c in Chapter 3 text verifies that transitions from  $|\pm 1\rangle$  states to the  $|A_2\rangle$  state have mutually orthogonal circular polarizations. Here we explain the observation shown in the figure and describe how we can extract the polarization imperfections of our system.

To obtain Figure 3.2c, the NV center is prepared in the  $|+1\rangle$  ( $|-1\rangle$ ) state with a  $1\ \mu\text{s}$  polarization step of off-resonant green excitation followed by a microwave  $\pi$  pulse resonant to the  $|0\rangle \leftrightarrow |+1\rangle$  ( $|0\rangle \leftrightarrow |-1\rangle$ ) transition. This transfer of population is followed by a short (2 ns) resonant optical excitation pulse tuned to the  $|+1\rangle \leftrightarrow |A_2\rangle$  ( $|-1\rangle \leftrightarrow |A_2\rangle$ ) transition. The fluorescence intensity recorded in the PSB in the presence of this excitation pulse is plotted as function of quarter wave plate (QWP) angle. The wave plate rotates the incident linearly polarized light into a well defined superposition of circular polarizations dependent on the angle. The length and intensity of the pulse is chosen such that it is close to an optical  $\pi$  pulse for the appropriate QWP angle that maximizes the fluorescence for the selected transition.

The electric field projections to  $\sigma_+$  and  $\sigma_-$  after the linearly polarized excitation beam passes the QWP at an angle  $\theta$  are  $\frac{1}{2}(i + e^{-2i\theta})$  for  $\sigma_+$  and  $\frac{1}{2}(i + e^{2i\theta})$  for  $\sigma_-$ ,



*Appendix A: Supporting material for Chapter 3*

so that the intensities in  $\sigma_+$  and  $\sigma_-$  oscillate out of phase as functions of  $2\theta$ .

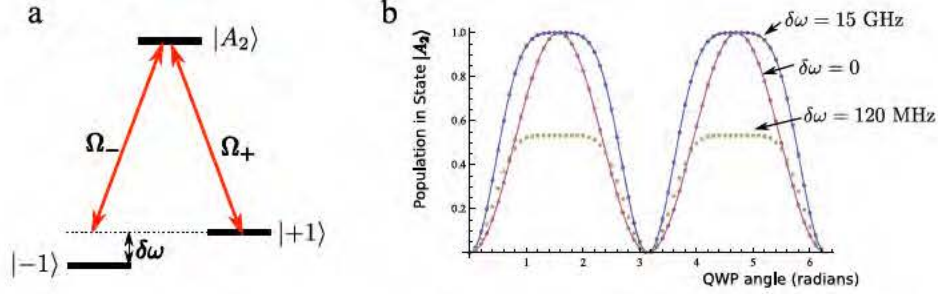


Figure A.4: Model and simulations for verification of circular polarization. **a** Simplified model used to explain the non-sinusoidal behavior. The excited state  $|A_2\rangle$  is coupled to the ground states  $|\pm 1\rangle$  with optical Rabi frequency  $\Omega_{\pm}$ . These Rabi frequencies are determined by the particular QWP angle  $\theta$ . The state prepared with microwave excitation is on-resonance with the optical field while the other is detuned by  $\delta\omega$  in the presence of the Zeeman splitting ( $2\pi \times 120$  MHz). **b** Calculated excited state populations for  $\Omega = \sqrt{\Omega_+^2 + \Omega_-^2} = 2\pi \times 250$  MHz. The pulse is on for 2 ns for the blue and red dots and 3.5 ns for the yellow dots. The detuning is assumed to be 0 for the red dots, 15 GHz for the blue dots and 120 MHz for the yellow dots. Solid lines are plots of expressions for the population in the two limits explained in the text.

Dynamics of the NV center under excitation by polarized light may be extracted from the simple model shown in Figure A.4. As our excitation beam is tuned to a particular transition, say  $|+1\rangle \leftrightarrow |A_2\rangle$ , the other transition from  $|-1\rangle$  is detuned by the Zeeman splitting  $\delta\omega$ . The optical Rabi frequencies associated with each transition are QWP angle dependent:  $\Omega_+ = \frac{\Omega}{2} (i + e^{-2i\theta})$  and  $\Omega_- = \frac{\Omega}{2} (i + e^{2i\theta})$ . We neglect spontaneous decay for simplicity since the optical excitation is relatively short. Our measured signal then corresponds to the population in the  $|A_2\rangle$  state after 2 ns ( $t = \pi/\Omega$ ) of evolution under optical excitation from the initial  $|+1\rangle$  or  $|-1\rangle$  state.

We first consider the limit  $\Omega \gg \delta\omega$ , where the natural basis is the “bright” and “dark” states defined by  $|b\rangle = \frac{\Omega_+|+1\rangle + \Omega_-|-1\rangle}{\Omega}$  and  $|d\rangle = \frac{\Omega_+|+1\rangle - \Omega_-|-1\rangle}{\Omega}$ . The applied



---

*Appendix A: Supporting material for Chapter 3*

---

excitation always acts as an optical  $\pi$  pulse that transfers the population from  $|b\rangle$  to  $|A_2\rangle$ . As the QWP rotates, our signal varies with the overlap between the prepared state  $|\pm 1\rangle$  and the bright state:  $|\langle \pm 1 | b \rangle|^2 = \frac{1 \pm \sin 2\theta}{2}$ . The expected angular dependence is sinusoidal, as demonstrated in Figure A.4

In the opposite limit where  $\Omega \ll \delta\omega$ , the detuned state is mostly off resonant, and the natural basis is again  $|+1\rangle$  and  $|-1\rangle$ . In this case we may neglect the off resonant level and consider two-level Rabi oscillations between the prepared state and  $|A_2\rangle$ . The population in the excited state for this case is given by  $\sin^2(\Omega_{\pm}t/2) = \sin^2\left(\frac{\pi\sqrt{(1 \pm \sin 2\theta)}}{2\sqrt{2}}\right)$ . As illustrated in Figure A.4, the population curve has a flattened top compared to a simple sinusoid.

For the NV center considered in the main text,  $\Omega \sim 2\pi \times 250$  MHz and  $\delta\omega \sim 2\pi \times 122$  MHz. We are thus in the intermediate regime between the two limits. As the QWP is rotated, both the Rabi frequency and the overlap with the bright state change, leading to more complex behavior. The yellow dots in Figure A.4b shows that if  $t$  is picked to be slightly longer than a  $\pi$  pulse, the  $|A_2\rangle$  population is nearly independent of angle near circular polarization. As the angle deviates from the  $\theta = \pi/2$ , the Rabi frequency decreases so that the population transferred to the  $|A_2\rangle$  state increases. On the other hand, the overlap of the prepared state with the bright state decreases. The combination of these two effects give rise to an extended flat-top behavior.

In addition, Figure 3.2c in the main text shows that the  $|+1\rangle$  and  $|-1\rangle$  cases give rise to differently shaped curves. We attribute this to different overlap of the confocal spot with the NV for the two measurements, which also explains the slightly different

### *Appendix A: Supporting material for Chapter 3*

---

collection efficiencies assumed for the two cases to fit the observed data. The fits used in the figure also include decay from the excited state, which decreases the population transferred to the excited state, but has no other significant effect.

The finite contrast observed in Figure 3.2c could be due to imperfect selection rules between the  $|A_2\rangle$  and ground states or imperfect circular polarization of the optical excitation. With Figure 3.2c alone it is not possible to distinguish between the two cases. Given the above discussion of the excited states, we estimate the mixing between the  $|A_2\rangle$  states and other excited states to be about 1 %. From these considerations we deduce that the selection rules are nearly perfect as described before, but that the imperfect optical system creates a slightly elliptical electric field vector  $0.94|\sigma_+\rangle + 0.34|\sigma_-\rangle$ . This ellipticity is expected to decrease the observed fidelity by 12 %.

## **A.5 Effects of magnetic environment, detunings, and echo**

The entangled state given in Eq. 1 of the main text is susceptible to fluctuations from the magnetic environment. In this section we show that these fluctuations and unaccounted detunings between the microwave fields and NV center transitions would lead to a decreased contrast of the observed oscillations. We then describe the echo technique used to improve the contrast.

We note that these imperfections, in the current context, mainly affect measurements in the  $H, V$  basis. Their effect on the  $\sigma_{\pm}$  basis is limited to inefficiencies in

population transfer to  $|0\rangle$  state and are thus accounted for by pulse errors, which are treated separately.

### A.5.1 Effect of finite detuning

We generalize the description given in the main text by introducing the rotating frame associated with the microwave fields:

$$|\pm\tilde{1}\rangle_t = e^{i\phi_{\pm}} e^{-i(\omega_{\pm} \mp \Delta)t} |\pm 1\rangle,$$

where we have added a particular detuning  $\Delta$  that covers the effect of hyperfine coupling to  $^{14}\text{N}$  nuclear spin and AC Stark shifts from non-resonant microwave fields. For the NV center used in this study there are no nearby  $^{13}\text{C}$  nuclear spins, hence their effect may be neglected. We estimate the static detuning of our microwave field from the relevant NV transition frequencies to be less than 500 kHz. The two microwave frequencies are well separated by  $\delta \sim 120$  MHz, so the presence of the non-resonant field mainly creates an AC Stark shift. For our Rabi frequency of 8 MHz the shift is estimated to be  $\Omega^2/\delta \sim 0.5$  MHz. For the idling times considered ( $\sim 500$  ns), the effect of the  $^{13}\text{C}$  nuclear bath is relatively small.

Under these assumptions, the state right before detection of the photon may then be written as:

$$|\Psi(t_d)\rangle = \frac{1}{\sqrt{2}} \left( e^{-i\phi_+} e^{i(\omega_+ - \Delta)t_d} |\sigma_+\rangle |\tilde{1}\rangle_{t_d} + e^{-i\phi_-} e^{i(\omega_- + \Delta)t_d} |\sigma_-\rangle |+\tilde{1}\rangle_{t_d} \right).$$

Following the detection and idling time  $t_i$ , the state becomes:

$$|\Psi(t_d)\rangle_{t_i} = \frac{1}{\sqrt{2}} \left( e^{-i\phi_+} e^{i(\omega_+ - \Delta)t_d - \Delta t_i} |\tilde{1}\rangle_{t_i} \pm e^{-i\phi_-} e^{i(\omega_- + \Delta)t_d + \Delta t_i} |+\tilde{1}\rangle_{t_i} \right)$$

### Appendix A: Supporting material for Chapter 3

---

where  $+$  ( $-$ ) corresponds to detection of a photon in  $H$  ( $V$ ) states. The idling time effects the signal we observe through (re-defining  $\alpha$  from the main text):

$$\alpha = (\omega_+ - \omega_- - 2\Delta)t_d + 2\Delta t_i - \Delta\phi$$

For example, the presence of  $^{14}\text{N}$  nuclear spin introduces a fixed detuning that is static for the duration of an experimental run, but from run to run changes between  $\Delta = 0, \pm 2.2$  MHz [138]. For  $t_i$  of order 200 ns the detuning may decrease the observed contrast significantly. While this effect can be reduced by simply waiting for an appropriate rephasing time for the  $^{14}\text{N}$ , there is still residual decoherence due to the  $^{13}\text{C}$  spin bath. To best eliminate all these effects and extend the memory time of the spin state, we add an echo sequence prior to spin measurement.

#### A.5.2 Spin echo sequence

The echo is easiest to describe in the  $|M\rangle = (|+\tilde{1}\rangle + |-\tilde{1}\rangle)/\sqrt{2}$  and  $|D\rangle = (|+\tilde{1}\rangle - |-\tilde{1}\rangle)/\sqrt{2}$  basis. We apply a  $t_i - 2\pi - t_i$  sequence with microwave pulses that drive the  $|M\rangle \leftrightarrow |0\rangle$  transition. This sequence is in spirit similar to the Bang-Bang decoupling technique[139]. For an arbitrary superposition  $|\psi\rangle$  of the orthogonal states  $|M\rangle$  and  $|D\rangle$ , evolution of time  $t_i$  under the detuning of the form given above leads to coherent oscillations between the states  $|D\rangle$  and  $|M\rangle$  and results in the state  $e^{-i2\Delta t_i \sigma_x} |\psi\rangle$ , where  $\sigma_i$  is the appropriate Pauli matrix in the  $|M\rangle, |D\rangle$  basis. If the magnetic field fluctuates from shot to shot this leads to decoherence. A fast  $2\pi$  pulse effectively switches the sign of the  $|M\rangle$  state ( $\sigma_z e^{-i2\Delta t_i \sigma_x} |\psi\rangle$ ). The subsequent evolution then creates the state  $e^{-i2\Delta t_i \sigma_x} \sigma_z e^{-i2\Delta t_i \sigma_x} |\psi\rangle = \sigma_z |\psi\rangle$ , which differs from the original state only by a relative phase that is independent of  $\Delta t_i$ .

### Appendix A: Supporting material for Chapter 3

In the context of section A.5.1, the procedure above results in the following state after the echo sequence in the  $|\pm\tilde{1}\rangle$  basis:  $\frac{1}{\sqrt{2}} \left( e^{-i\phi_+} e^{i(\omega_+ - \Delta)t_d} |\tilde{1}\rangle \pm e^{i\phi_-} e^{i(\omega_- + \Delta)t_d} |-\tilde{1}\rangle \right)$ . Hence our signal is only affected by the random arrival time of the photon  $t_d$  and not the idling time. For detunings on the order of 5 MHz, the frequency shift is about 4 % of the center frequency of the oscillations (120 MHz) and may be neglected within our current signal to noise.

We note that for a finite length of the  $2\pi$  pulse (around 110 ns), the echo is expected to be imperfect, as the magnetic field continues to rotate the states in the  $|M\rangle, |D\rangle$  basis while the pulse is being applied. By timing the echo sequence correctly, we can compensate for this imperfection.

To find the optimal timing of  $t_i$  for our experiment, we carry out a simple echo experiment illustrated in Figure A.5. Given Figure A.5b we pick  $t_i = 170$  ns for optimum compensation such that an almost perfect echo is performed.

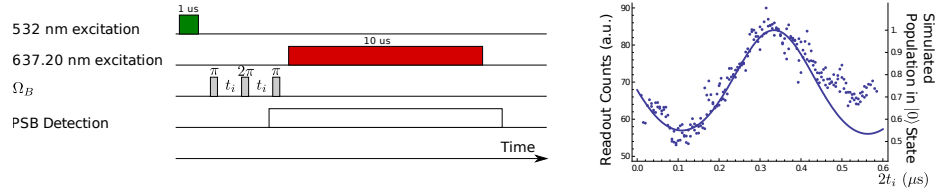


Figure A.5: Echo technique used. **a.** Pulse sequence implemented to test the echo technique. The system is initialized to the  $|0\rangle$  state followed by  $5\ \mu\text{s}$  of waiting time. A  $\pi$  pulse is applied to create a bright superposition  $|M\rangle$  of  $|\pm 1\rangle$  states. The state is allowed to evolve for time  $t_i$  before a  $2\pi$  refocusing pulse is applied, after which the state evolves for time  $t_i$  again. A  $\pi$  pulse then maps the state back to  $|0\rangle$  and is followed by a resonant readout pulse. **b.** Result of the sequence described in part (a). Solid line is a theory fit where only the effect of  $^{14}\text{N}$  has been taken into account.

## A.6 Fidelity estimates

We would like to determine the lower bound for the entanglement fidelity[22]:

$$F \geq (F_1 + F_2)/2 \quad (\text{A.1})$$

where

$$F_1 = \rho_{\sigma_+ -1, \sigma_+ -1} + \rho_{\sigma_- +1, \sigma_- +1} - 2\sqrt{\rho_{\sigma_+ +1, \sigma_+ +1} \rho_{\sigma_- -1, \sigma_- -1}} \quad (\text{A.2})$$

$$F_2 = \rho_{H+, H+} - \rho_{H-, H-} + \rho_{V-, V-} - \rho_{V+, V+}. \quad (\text{A.3})$$

We obtain  $F_1 = 0.83 \pm 0.10$  by measuring the quantities  $\rho_{\sigma_+ -1, \sigma_+ -1}$ ,  $\rho_{\sigma_- +1, \sigma_- +1}$ ,  $\rho_{\sigma_+ +1, \sigma_+ +1}$ , and  $\rho_{\sigma_- -1, \sigma_- -1}$  in the original basis of the photon and spin.  $F_2$  is related to the oscillation amplitudes  $a_H/2 = \rho_{H-, H-} - \rho_{H+, H+}$  and  $a_V/2 = \rho_{V+, V+} - \rho_{V-, V-}$ , measured in the rotated basis.

### A.6.1 Time bin optimization

One approach to obtaining the amplitudes  $a_H$  and  $a_V$  is by directly fitting to the oscillations in the conditional probability, as shown in Figure 3.4c of Chapter 4. The resolution of our time-tagged-single-photon-counting device is 4 ps. However, due to our low count rates, only a fraction of the 4 ps time bins register a photon in the signal region during the entire experimental run. Therefore, to obtain the conditional probability, we group the ZPL counts and their corresponding readout results into larger time bins. One commonly used method is to optimize the goodness of the fit of a particular model to the data by varying size of the bins so that the error of the fit is minimized [140]. However, such a method involves computationally intensive

### *Appendix A: Supporting material for Chapter 3*

---

procedures. Therefore we have used a simplified version of this method, motivated by the fact that our count rates decrease exponentially as a function of  $t_d$ . In essence, the time bins are determined one at a time starting from the beginning of the decay by minimizing the fit error while varying each successive time bin between 900 ps and 2 ns, which is longer than the timing resolution of our photon detectors ( $\sim 300$  ps) and shorter than the period of the expected oscillations. Since the count rate is highest at the beginning of the decay and should therefore be amenable to the smallest time bins, we start by fixing the first three time bins to 900 ps. We then add the next time bin, vary its length, and perform a fit to the data in these first four bins. The length of the fourth bin is then chosen to minimize the mean squared error of the fit. This optimization process is repeated for each successive time bin until 15 ns of data are used. Such an optimization of the bin sizes is done separately for the H and V polarizations.

We emphasize that the time bins are chosen to optimize the error of the resulting fits, not the amplitude of the fitted oscillations. As shown in Figure 3.4c, the time-binned data exhibit clear oscillations and allows us to extract a fidelity above the classical limit using the fit.

#### **A.6.2 Maximum likelihood estimate**

Any time binning method, while necessary to present the data in a reasonable fashion, introduces errors by changing the timing information of the raw data. In order to ensure that such errors do not lead to an incorrect estimate of the fidelity, we also extract the fidelity directly from the raw data using a maximum likelihood

*Appendix A: Supporting material for Chapter 3*

---

method. In addition, we calculate the probability distribution for the fidelity, which not only indicates a high probability of entanglement demonstration, but, by virtue of being nearly a perfect Gaussian, justifies minimization of the mean squared error used in the optimization procedure above.

We first derive the formula for the joint probability distribution function of detecting a photon at time  $t$  and measuring the spin state  $|M\rangle$ . Due to the single exponential decay of the optical excited state, the probability distribution for detection of a  $|H\rangle$  or  $|V\rangle$  photon at time  $t$  is

$$p_{H,V}(t) = \frac{1}{\tau} e^{-t/\tau}, \quad (\text{A.4})$$

where  $\tau = 12$  ns is the lifetime of the excited states. For a perfect spin-photon entangled state, upon detection of a  $|H\rangle$  or  $|V\rangle$  photon at time  $t$ , the conditional probability of measuring the spin state  $|M\rangle$  is  $p_{M|H,V}(t) = \frac{1}{2}(1 \pm \cos \alpha(t))$  with  $\alpha(t) = (\omega_+ - \omega_-)t + (\phi_+ - \phi_-)$ . For an imperfect spin photon entangled state, the conditional probability has a reduced oscillation amplitude:

$$p_{M|H,V}(t) = \frac{1}{2}(1 \pm a_{H,V} \cos \alpha(t)). \quad (\text{A.5})$$

Thus, the joint probability is

$$p_{M;H,V}(t) = p_{M|H,V}(t) p_{H,V}(t) \quad (\text{A.6})$$

$$= \frac{1}{2\tau} e^{-t/\tau} (1 \pm a_{H,V} \cos \alpha(t)). \quad (\text{A.7})$$

Motivated by these considerations we aim to model the experimental data using the following fitting functions:

$$f_H(t) = \frac{c_H}{2} (1 + a_H \cos(2\pi t/T + \phi)) e^{-t/\tau} + b_0, \quad (\text{A.8})$$

$$f_V(t) = \frac{c_V}{2} (1 - a_V \cos(2\pi t/T + \phi)) e^{-t/\tau} + b_0, \quad (\text{A.9})$$



*Appendix A: Supporting material for Chapter 3*

---

with fitting parameters  $\{c_H, c_V, a_H, a_V, T, \phi, b_0\}$ . Here  $c_H$  and  $c_V$  are proportional to duration of the experiment and  $b_0$  is the background.

We denote the number of conditional readout events within each  $\Delta t = 4$  ps detection time bin  $[t, t + \Delta t]$  as  $n_{H,t}$  and  $n_{V,t}$  for the two photon polarizations, and obtain the data sets  $\{n_{H,t}\}$  and  $\{n_{V,t}\}$  with  $t = t_0, t_0 + \Delta t, t_0 + 2\Delta t, \dots$ . For a given set of data and underlying probability model, a maximum likelihood estimate (MLE) picks the values of the model parameters that maximize the *likelihood function* for the data, compared to other choices of parameters. Given no prior knowledge of the fitting parameters, we may assume an uniform distribution for the fitting parameters. Then the likelihood function will be proportional to the probability distribution function. In the following, we use the MLE to fit the theoretical model with experimental data and obtain the oscillation amplitudes  $a_H$  and  $a_V$ .

The expected average number of events for the time bin  $[t, t + \Delta t]$  are given by equations A.8 & A.9 above. However, the number of recorded events for each time bin has fluctuations characterized by the Poisson distribution

$$p_\lambda(n) = \frac{\lambda^n}{n!} e^{-\lambda}, \quad (\text{A.10})$$

where  $\lambda$  is the average number of events. Thus, the *likelihood* for recording  $n_{H,t}$  events of detecting an  $|H\rangle$  photon at time  $t$  and measuring the NV center in spin state  $|M\rangle$  is

$$L_H(n_{H,t}, t) = p_\lambda(n_{H,t})|_{\lambda=f_H(t)} \quad (\text{A.11})$$

$$= \frac{f_H(t)^{n_{H,t}}}{n_{H,t}!} e^{-f_H(t)}. \quad (\text{A.12})$$

*Appendix A: Supporting material for Chapter 3*

---

The likelihood for getting the list  $\{n_{H,t}\}$  is

$$L_H(\{n_{H,t}\}) = \prod_t L_H(n_{H,t}, t). \quad (\text{A.13})$$

Similarly, the likelihood for the list  $\{n_{V,t}\}$  is

$$L_V(\{n_{V,t}\}) = \prod_t L_V(n_{V,t}, t), \quad (\text{A.14})$$

where

$$L_V(n_{V,t}, t) = \frac{f_V(t)^{n_{V,t}}}{n_{V,t}!} e^{-f_V(t)}. \quad (\text{A.15})$$

We numerically maximize the following likelihood function for both lists  $\{n_{H,t}\}$  and  $\{n_{V,t}\}$ :

$$L(\{n_{H,t}\}, \{n_{V,t}\}) = L_H(\{n_{H,t}\}) L_V(\{n_{V,t}\}). \quad (\text{A.16})$$

We use the generic gradient ascend algorithm to maximize the likelihood function with the optimal choice of parameters as listed in Table A.1. We verify that it is also a global maximum by sampling throughout the entire parameter space numerically.

Table A.1: Optimal choice of parameters from the MLE.

Parameter	$a_H$	$a_V$	$c_H$	$c_V$	$T$ (ns)	$\phi$	$b_0$
value	0.65	0.55	0.083	0.090	8.2	-4.04	0.000

In Figure A.6.2a, we plot the contour of likelihood as a function of  $a_H$  and  $a_V$ . Since we have no prior knowledge about the parameters  $a_H$  and  $a_V$ , we can use an uniform prior probability distribution for  $a_H$  and  $a_V$ . Then the 2D likelihood plot is proportional to the 2D probability distribution  $P_{a_H, a_V}$  joint with the observed data.

The marginal probability distribution  $P_{a_H+a_V}$  associated with  $a_H + a_V$  is the projection of the full distribution to the  $+45^\circ$  direction. The marginal probability distribution can be obtained by integrating the 2D probability  $P_{a_H, a_V}$  along the  $-45^\circ$

Appendix A: Supporting material for Chapter 3

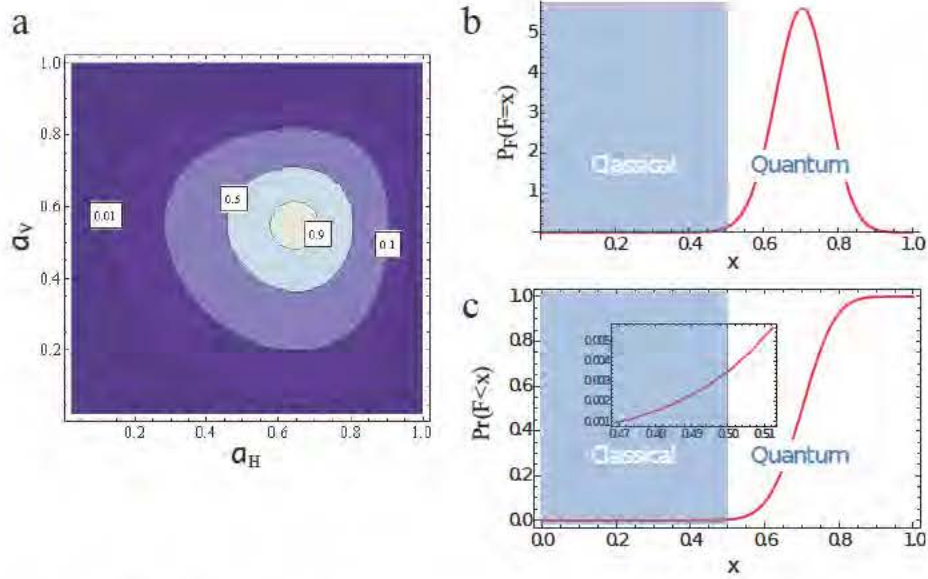


Figure A.6: Results of maximum likelihood estimate. **a.** Contour plot of likelihood as a function of  $a_H$  and  $a_V$ . The contour lines represent relative likelihood of 90%, 50%, 10%, 1% from inside out. With no prior knowledge of  $a_H$  and  $a_V$ , the likelihood is proportional to the probability distribution. **b.** The probability distribution for the lower bound on the entanglement fidelity  $F$ . **c.** The cumulative probability distribution for the entanglement fidelity  $F$ . Inset: A zoomed plot around  $F = 0.5$ , showing the cumulative probability is only 0.35%.

direction:

$$P_{a_H+a_V}(u) \propto \int dv P_{a_H,a_V}\left(\frac{u+v}{2}, \frac{u-v}{2}\right). \quad (\text{A.17})$$

Because  $F_2 = (a_H + a_V)/2$ , we obtain the probability distribution for  $F_2$ :

$$P_{F_2}(x_1) \propto P_{a_H+a_V}(2x_1). \quad (\text{A.18})$$

The probability distribution for the lower bound on the fidelity is a convolution of  $P_{F_1}(x)$  and  $P_{F_2}(x)$ :

$$P_F(F=x) = \int_{-\infty}^{+\infty} dx_1 P_{F_1}(x_1) P_{F_2}(x-x_1), \quad (\text{A.19})$$

where  $P_{F_1}$  is assumed to be a Gaussian probability distribution for  $F_1$  with mean 0.83

*Appendix A: Supporting material for Chapter 3*

---

and standard deviation 0.10. We find that the distribution  $P_F(x)$  in Figure A.6.2b is nearly Gaussian and obtain an entanglement fidelity of  $F \geq 0.70 \pm 0.070$ . The cumulative probability distribution

$$\Pr(F < x) = \int_{-\infty}^x dx' P_F(x') \quad (\text{A.20})$$

is shown in Figure A.6.2c and indicates that the probability that the entanglement fidelity is above the quantum threshold of 0.5 is

$$\Pr(F > 0.5) = 99.7\%. \quad (\text{A.21})$$

These results confirm that our experiment provides a reliable observation of spin-photon entanglement.

# Appendix B

## Supporting material for Chapter 4

### B.1 Experimental details

#### B.1.1 Sample description

The diamond sample used in the experiments described in Chapter 4 was a natural, high purity, type IIa diamond with a  $\langle 111 \rangle$  cut kept at  $\sim 7$  K. Within this sample, we used three separate NV centers for the data presented in Chapter 4 and this appendix. A first NV center (NVa) is subject to a relatively low strain and has a narrow distribution of  $^{13}\text{C}$  states. A second, higher strain NV center (NVb) has a broader distribution of  $^{13}\text{C}$  states. All experiments on optical cooling and conditional preparation were repeated with both of these NV centers with consistent results. Figures 4.1, 4.2 and 4.4e and Fig. B.3 present measurements for NVa. The remaining figures in Chapter 4 and this appendix excluding Fig. B.5 present measurements on NVb. An additional NV (NVc) was used for ESR measurements in Section B.5 ,

## *Appendix B: Supporting material for Chapter 4*

---

which was used to calibrate the ground state strain for other NV centers by assuming that it is proportional to the strain measured in the excited state [89].

### **B.1.2 Experimental setup**

Our experimental setup is similar to that described earlier [81], with several modifications. First, the three excitation lasers addressing the  $|A_1\rangle$ ,  $|A_2\rangle$ , and  $|E_y\rangle$  states are kept within a “rough” beatnote lock (3 dB width  $\sim 5$  MHz) relative to each other. The master laser, driving the  $|A_1\rangle$  transition, is allowed to “float” freely. Its frequency relative to the NV is monitored through fluorescence counts and adjusted manually every few minutes. The beatnote lock is achieved by feeding the beatnote of the relevant pair of lasers to a commercial PLL board (Analog Devices ADF4007) which converts the beatnote to an error signal. This signal is fed into a commercial FPGA based reconfigurable data acquisition board (National Instruments NI-7833R). The FPGA is programmed to act as a PI controller, and its outputs are fed into the current and cavity inputs of the lasers.

To apply an external magnetic field along the  $\langle 111 \rangle$  direction a solenoid was placed outside our cryostat. The cryostat significantly alters the magnetic field at the location of the NV from the applied field. We compensate for this effect of the solenoid – cryostat system by characterizing its frequency response using the NV electron spin as a local magnetometer. We then apply the magnetic field waveform that compensates for the linear response of the setup, so that the desired time varying magnetic field is generated at the NV.

### **B.1.3 Effects of ionization and other forms of spectral drift**

We have already touched upon the effects of ionization in Chapter 4. Here we provide the details of the experimental sequence used to obtain the data presented in Chapter 4.

Under continuous resonant excitation the NV center ionizes with a timescale that depends on the laser power [84]. For example, with 50 nW of power on the  $A_1$  laser and  $1\mu\text{W}$  of power on the  $E_y$  laser, we measure an ionization timescale of  $\sim 29$  ms (Fig. B.1). The ionization feature is present regardless of whether the data is taken within or outside a CPT dip. This effect complicates comparison of data taken with different laser power or durations, decreases the observed contrast of CPT resonances, prevents the accurate extraction of other timescales, etc. To eliminate the influence of this effect, we perform all of our measurements except those shown in Figure 4.1 with a step at the end of each run of the sequence to verify that the NV has not ionized. To do this we turn on the  $A_1, A_2$  and  $E_y$  lasers simultaneously for  $\sim 1$  ms. With all three lasers present there is no dark state, and the NV should produce a large number of counts if it is not ionized, and zero photons if it is. We then discard data from runs that do not pass a threshold for the number of collected verification photons. The effect of this post-selection process is shown in Fig. B.1. We note that this process not only selects for unionized cases, but also for accurate positioning of the NV and tuning of the laser frequency. This could lead to the slight rise in counts seen in the post-selected cases, where the NV is relatively dark at the beginning and becomes brighter by the time of the verification step.

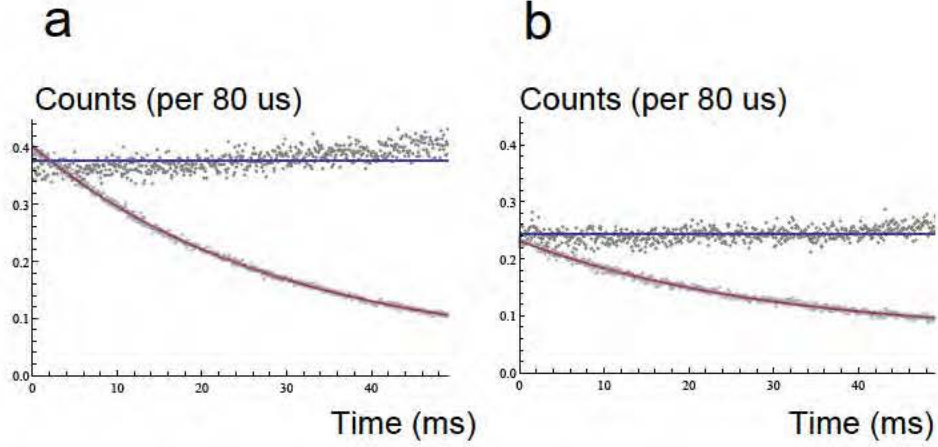


Figure B.1: Average count rates under continuous  $A_1$  and  $E_y$  excitation at two different fixed magnetic field with (blue) and without (red) post-selection for ionization. (a) Out of CPT resonance, decay timescale is  $29.1 \pm 0.3$  ms without verification. (b) In CPT resonance, decay timescale is  $29.4 \pm 0.6$  ms without verification.

## B.2 Multilevel description of the NV center

In order to understand the dynamics of our system including the effects of the recycling transition, we model its behavior using a full master equation approach. For simplicity, we neglect the  $|E_x\rangle$  and  $|E_{1,2}\rangle$  states as they are detuned from all driving fields. The resulting level structure and transitions are shown in Figure B.2.

In addition to all processes shown in the diagram, we include pure dephasing in the excited state at a rate  $\Gamma$ . For resonant excitation of, say, the  $|A_1\rangle$  state, the off-resonant excitation of the  $|A_2\rangle$  state does not play a significant role most of the time as it is far detuned. We will neglect the effects of far detuned states for the current discussion. We will find, though, that for understanding the  $^{14}\text{N}$  polarization behavior these off-resonant excitations play a crucial role and its effects will be included in Section B.4 describing the  $^{14}\text{N}$  polarization. As described in section B.5,



Appendix B: Supporting material for Chapter 4

---

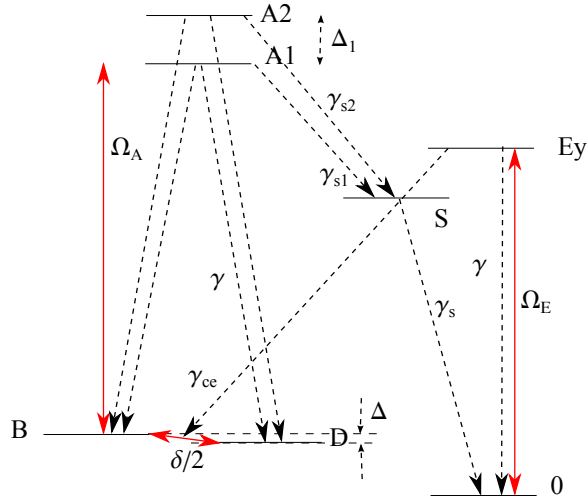


Figure B.2: Simplified level structure of NV center.  $|B\rangle$  and  $|D\rangle$  are the bright and dark states for a laser  $\Omega_A$  coupled resonantly to either the  $|A_1\rangle$  or  $|A_2\rangle$  state.  $\delta$  is the Zeeman splitting between  $|\pm 1\rangle$  states, such that  $\delta/2$  is the effective Rabi frequency between  $|B\rangle$  and  $|D\rangle$ .  $\Delta$  is the strain splitting in the ground state, and  $\Delta_1$  is the energy splitting between  $|A_1\rangle$  and  $|A_2\rangle$  states. The  $|E_y\rangle$  state is addressed by a laser  $\Omega_E$  and decays into the  $|\pm 1\rangle$  states with a total rate  $\gamma_{ce}$ , while the direct decay rate back to the  $|0\rangle$  state is  $\gamma$ . The  $|A_1\rangle$  ( $|A_2\rangle$ ) state decays to the singlet  $|S\rangle$  with rate  $\gamma_{s1}$  ( $\gamma_{s2}$ ), which then decays to  $|0\rangle$  with rate  $\gamma_s$ .

### Appendix B: Supporting material for Chapter 4

---

we will assume an appropriate alignment of the  $A_{1,2}$  laser polarization relative to the strain axis. We construct equations describing the evolution of the density matrix elements  $d\vec{\rho}/dt = M\vec{\rho}$ , where  $M$  is the evolution matrix including the Liouvillian operators for various decay and dephasing processes (defined in Figure B.2) as well as Hamiltonian operators. Below we describe results showing the steady state of the system of equations.

Since the  $|A_1\rangle$  state corresponds to an open  $\Lambda$  system with  $\gamma_{ce} \ll \gamma_{s1}$ , we expect essentially all of the excited state population to be in (and all the fluorescence to be from) the  $E_y$  state. We can obtain an analytical solution for this population in the following form:

$$P_{E_y} = \rho_{E_y, E_y} = \frac{c_0 \delta^2}{c_1 \delta^4 + c_2 \delta^2 + c_3} \quad (\text{B.1})$$

where

$$\begin{aligned} c_0 &= 2\gamma_s \gamma_{s1} (\gamma + 2\Gamma) \Omega_A^2 \Omega_E^2, \\ c_1 &= \gamma \gamma_{ce} \gamma_s \Omega_E^2, \\ c_2 &= \frac{1}{2} \gamma \gamma_s \gamma_{s1} (\gamma + 2\Gamma)^2 \Omega_A^2 + \gamma \gamma_s \gamma_{ce} (\gamma + 2\Gamma)^2 \Omega_E^2 + 2\gamma \gamma_s \gamma_{ce} \Delta^2 \Omega_E^2 + \\ &\quad 2[4\gamma_s \gamma_{ce} \Gamma + \gamma_{ce} (\gamma_s + \gamma_{s1}) (\gamma + 2\Gamma) + 2\gamma_s \gamma_{s1} (\gamma + 2\Gamma)] \Omega_A^2 \Omega_E^2 \\ c_3 &= \gamma \gamma_s \gamma_{ce} [(\gamma + 2\Gamma)^2 \Delta^2 \Omega_E^2 + \Delta^4 \Omega_E^2 + 4\Delta^2 \Omega_A^2 \Omega_E^2 + 4\Omega_A^4 \Omega_E^2] \end{aligned}$$

Assuming  $\delta, \Delta$ , and  $\Omega_A \ll \gamma + 2\Gamma$ , we can drop the second and third terms in  $c_3$ , the third term in  $c_2$ , and ignore the fourth order term in  $\delta$ . In addition, since  $\gamma_{ce} \ll \gamma_{s1}$ , the last term in  $c_2$  is approximately just  $4\gamma_s \gamma_{s1} (\gamma + 2\Gamma) \Omega_A^2 \Omega_E^2$ . As a result we find

$$P_{E_y} = A \frac{\delta^2}{\delta^2 + \delta_0^2} \quad (\text{B.2})$$

*Appendix B: Supporting material for Chapter 4*

---

where the amplitude is given by

$$A = \frac{1}{2 + \frac{\gamma(\gamma+2\Gamma)}{4\Omega_E^2} + \frac{\gamma(\gamma+2\Gamma)}{4\Omega_A^2} \frac{2\gamma_{ce}}{\gamma_{s1}}} = \frac{1}{2 + \frac{\gamma}{R_{Ey}} + \eta \frac{\gamma}{R_{A1}}} \quad (\text{B.3})$$

and the width (HWHM) is given by

$$\delta_0^2 = \frac{\Delta^2 + \frac{4\Omega_A^4}{(\gamma+2\Gamma)^2}}{1 + \frac{\gamma_{s1}\Omega_A^2}{2\gamma_{ce}\Omega_E^2} + \frac{4\gamma_{s1}\Omega_A^2}{\gamma_{ce}\gamma(\gamma+2\Gamma)}} = \frac{\Delta^2 + (R_{A1}/2)^2}{1 + \frac{1}{\eta} \left( \frac{R_{A1}}{R_{Ey}} + \frac{2R_{A1}}{\gamma} \right)} \quad (\text{B.4})$$

Here  $R_{Ey} = \frac{4\Omega_E^2}{\gamma+2\Gamma}$ ,  $R_{A1} = \frac{4\Omega_A^2}{\gamma+2\Gamma}$  are the optical pumping rates for lasers tuned to  $|A_1\rangle$  and  $|E_y\rangle$ , and  $\eta = \frac{2\gamma_{ce}}{\gamma_{s1}}$ .

For the case of the  $|A_2\rangle$  state, equation B.4 is inaccurate because  $\gamma_{ce}$  is on the same order as  $\gamma_{s1}$ . In this case the main difference is that we cannot simplify the last term of  $c_2$ , and we use instead the full expression for the width given by

$$\delta_0^2 = \frac{\Delta^2 + (R_{A2}/2)^2}{1 + \frac{R_{A2}}{\eta R_{Ey}} + \left( \frac{2\Gamma}{\gamma+2\Gamma} + \frac{\gamma_s + \gamma_{s2}}{2\gamma_s} + \frac{2}{\eta} \right) \frac{R_{A2}}{\gamma}} \quad (\text{B.5})$$

In addition to  $\delta_0$  we can now express other relevant experimental parameters in terms of results of the above model. The following set of equations lists the commonly used parameters in the Chapter 4 and this appendix relevant for  $A_1$  CPT excitation:

$$C = A\epsilon\gamma = \frac{R_A\epsilon/\eta}{\frac{1}{\eta} \left( \frac{2R_A}{\gamma} + \frac{R_A}{R_E} \right) + 1} \quad (\text{B.6})$$

$$\delta_0 = \sqrt{\frac{\Delta^2 + (R_A/2)^2}{1 + \frac{1}{\eta} \left( \frac{R_A}{R_E} + \frac{2R_A}{\gamma} \right)}} \quad (\text{B.7})$$

$$\delta_c = \sqrt{\ln 2} \sqrt{\frac{\delta_0^2}{CT_{\text{cond}}}} = \sqrt{\ln 2} \sqrt{\frac{\eta}{\epsilon} \frac{\Delta^2 + (R_A/2)^2}{R_A T_{\text{cond}}}} \quad (\text{B.8})$$

where  $\epsilon$  is the collection efficiency roughly  $5 \times 10^{-4}$  for our setup.

We note that  $\delta_0$  approaches  $\Delta$  as  $R_A$  goes to 0 and has a minimum at  $R_A = \frac{-R_E\gamma\eta + \sqrt{4(2R_E+\gamma)^2\Delta^2 + R_E^2\gamma^2 + \eta^2}}{2R_E+\gamma}$ . For a certain range of experimental parameters the minimum value of  $\delta_0$  can be significantly less than  $\Delta$ .

## Appendix B: Supporting material for Chapter 4

---

For example, to compare these results with the CPT width using the  $|A_1\rangle$  state shown in Figure 4.1, we convolve the Lorentzian CPT lineshape with a Gaussian  $^{13}\text{C}$  distribution with FWHM given by  $w_0$ . The resulting Voigt profile [141] has a FWHM of  $w' \approx 0.5346(2\delta_0) + \sqrt{w_0^2 + 0.2166(2\delta_0)^2}$ . Similarly, the CPT width using the  $|A_2\rangle$  was determined using Eq. B.5. Note that the only fitting parameters used for both sets of data are  $w_0$  and the conversion factor between optical power and optical pumping rate. We determine all relevant decay rates through an independent measurement described in the next section.

### B.3 Measurement of branching ratios

As shown in the previous section, the behavior of our CPT system depends on the branching ratios between various states of the NV center. In order to apply our model to experimental results, we carefully measure these branching ratios for the relevant excited states using the method described in Chapter 2. To do this we apply a magnetic field such that the NV is not in a CPT resonance and there is a finite precession rate between the dark and bright states. We then prepare the NV center in either the  $|\pm 1\rangle$  or  $|0\rangle$  state via optical pumping, and excite the  $|\pm 1\rangle \leftrightarrow |A_{1,2}\rangle$  or  $|0\rangle \leftrightarrow |E_y\rangle$  transitions individually while collecting fluorescence as a function of time. Figure B.3 shows double-exponential fits to data from NVa for all three transitions. The branching ratios are directly linked to these observed timescales.

For the  $|A_2\rangle$  state, the short timescale correspond directly to the timescale of optical pumping to the electronic dark state of the  $|\pm 1\rangle$  states, and is governed by the optical excited state lifetime  $\gamma$ . Given a finite  $\delta$ , this process should lead to a

*Appendix B: Supporting material for Chapter 4*

---

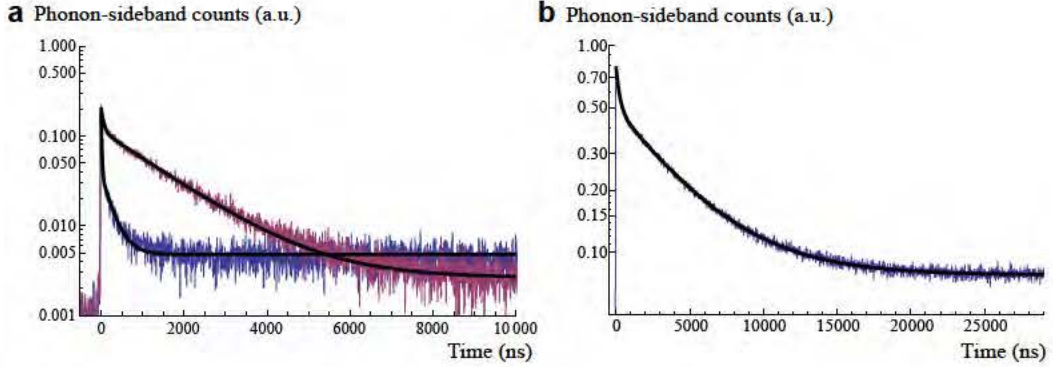


Figure B.3: Fluorescence decay of (a)  $|A_1\rangle$  (blue),  $|A_2\rangle$  (red), and (b)  $|E_y\rangle$  states with fits to double exponential decays (black lines).

steady state fluorescence rate. The presence of a second long timescale then indicates a decay out of the three level system into the singlet and subsequently the  $m_s = 0$  manifold. For the  $|A_1\rangle$  state, we expect the fast decay into  $|0\rangle$  to give rise to a short timescale. Following this fast process, the remaining population in the electronic dark states escape due to  $\delta$  and gives rise to another longer time scale. Therefore, we find the decay rates into  $|0\rangle$  to be  $\gamma_{s1} \sim 1.6\gamma$  and  $\gamma_{s2} \sim 130\gamma$ , where  $\gamma$  is the direct decay rate back into the ground state. For the  $|E_y\rangle$  state, there is also a finite branching ratio into the singlet, which then decays back into  $|0\rangle$ . Combined with the cross transition into the  $|\pm 1\rangle$  states, this effect gives rise to a double exponential decay. Using rate equations for the dynamics between  $|0\rangle, |S\rangle, |E_y\rangle$ , and  $|\pm 1\rangle$ , we can determine the cross transition rate in terms of the measured timescales, which correspond to the eigenvalues of the system evolution. Using this method, we find that  $\gamma/\gamma_{ce} \sim 105$ .

## B.4 $^{14}\text{N}$ polarization via optical pumping and measurement based preparation

### B.4.1 Optical Pumping

We now use our description of the open CPT system to model optical cooling of the  $^{14}\text{N}$  nuclear states. The nuclear spin dynamics of interest are governed by the flip-flop interaction between the nuclear and the electronic spin in the electronic excited state [41, 142]. We note that this rate is slow compared to electronic dynamics, therefore we will assume the electronic state reaches steady state instantaneously within the nuclear diffusion time. For our model we will take the transition rates between different nuclear spin states to be proportional to the steady state excited state population of the electron spin for the corresponding Overhauser field created by the  $^{14}\text{N}$  and the externally applied field. In accordance with our experiment (Figure 4.2), we will set the applied magnetic field to the center of the three  $^{14}\text{N}$  CPT resonances such that the  $m_I = 0$  state forms the dark (or trapping) state. The excitation rate out of the dark state is expected to be small compared to the rate in from other nuclear states. The final polarization that can be reached will be determined by the steady-state solution to the nuclear state populations.

First, note that we work with  $R_{Ey}$  near saturation, so equation B.2 can be simplified as

$$P_{Ey}(\delta) = \frac{\delta^2}{(2 + \frac{\eta\gamma}{R_{A1}})(\delta^2 + \frac{\Delta^2 + (R_{A1}/2)^2}{(1 + \frac{2R}{\eta\gamma})})} = \frac{R'(\delta)}{2R'(\delta) + \eta\gamma} \quad (\text{B.9})$$

where  $R'(\delta) = \delta^2 R_{A1}/(\delta^2 + \Delta^2 + R_{A1}^2/4)$  is the effective rate out of the dark state and

*Appendix B: Supporting material for Chapter 4*

---

into  $|A_1\rangle$ .

When the  $^{14}\text{N}$  spin is in the  $m_I = \pm 1$  states, the nuclear spin flip-flop rate, or the rate into  $m_I = 0$ , is given by  $R_{in} = A_{ex}P_{E_y}(\delta_N)$ , where  $A_{ex}$  is the hyperfine coupling in the excited state, and  $\delta_N=4.4$  MHz is the hyperfine splitting in the ground state. On the other hand, there are two contributions to the rate out of the  $m_I = 0$  state. The first is due to  $\delta_{T_2^*}$ , which we define as the average two photon detuning due to interactions with the  $^{13}\text{C}$  bath. The second process is off-resonant excitation of the  $|A_2\rangle$  state at a rate  $\xi R_{A1}$ , where  $\xi = (\gamma/2 + \Gamma)^2/\Delta_1^2$  with  $\Delta_1$  being the detuning between  $|A_1\rangle$  and  $|A_2\rangle$ . For the NV center used in our optical pumping experiments,  $\gamma/2 + \Gamma \sim 100$  MHz and  $\Delta_1 \sim 3$  GHz. For small  $R_{A1}$ , this off-resonant process contributes as an additional incoherent decay rate out of the dark state given by  $\xi R_{A1}/2$ , since the  $|A_2\rangle$  state decays with probability 1/2 into the bright state, where it is then excited with rate  $R_{A1}$ . Note that we are neglecting direct decay out of  $|A_2\rangle$  into the  $m_s = 0$  states, since  $\eta_{A2} \gg \eta_{A1}$ . As a result, the modified rate into  $|A_1\rangle$  from the dark state for the  $m_I = 0$  state is  $R'(\delta_{T_2^*}) + \xi R_{A1}/2$ , and the rate out of the  $m_I = 0$  state is given by

$$R_{out} = A_{ex} \frac{R'(\delta_{T_2^*}) + \xi R_{A1}/2}{2(R'(\delta_{T_2^*}) + \xi R_{A1}/2) + \eta\gamma} \quad (\text{B.10})$$

Finally, the steady state population in  $m_I = 0$  is given by  $P_0 = R_{in}/(2R_{out} + R_{in})$ . We show this result with the experimental data in Figure 4.2d where no fitting parameter has been used.



## Appendix B: Supporting material for Chapter 4

### B.4.2 Details of measurement based preparation

The dynamics associated with the  $^{14}\text{N}$  pumping mechanism determines the pulse sequence used for measurement based preparation of the  $^{14}\text{N}$  state. Measurement based preparation is carried out via post-selection of events in which zero counts are detected during preparation photon counting time window ( $\tau_{\text{prep}}$  in Fig B.4a). We note that we want to maximize the polarization that is achieved and minimize the experimental run-time needed to verify the obtained polarization.

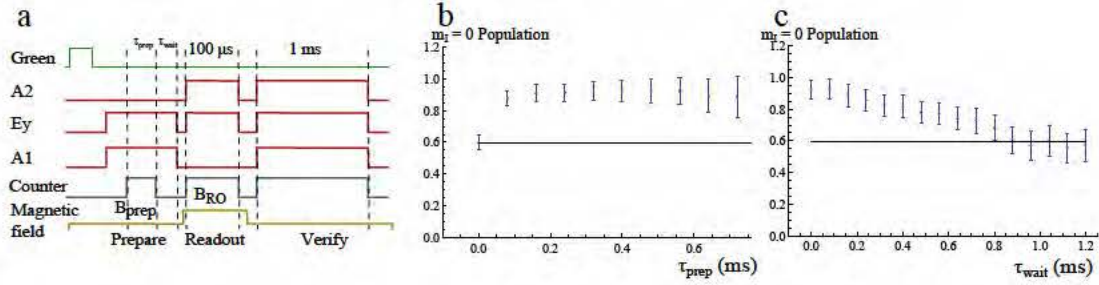


Figure B.4: Measurement based preparation of  $^{14}\text{N}$  spin. (a) Pulse sequence used in the Chapter 4 where duration of the photon counting window used for preparation ( $\tau_{\text{prep}}$ ) and time between the preparation counting window and the end of the preparation laser pulse ( $\tau_{\text{wait}}$ ) are indicated. (b) Change in prepared population as a function of  $\tau_{\text{prep}}$  for the data presented in Figure 4.2c (red and yellow),  $\tau_{\text{wait}} = 0$ . Black line indicates the polarization achieved with optical pumping, and no measurement based polarization. All data presented in this figure post-selects for events where zero counts are detected during  $\tau_{\text{prep}}$ . (c) Population of  $m_I = 0$  as a function of  $\tau_{\text{wait}}$  for  $\tau_{\text{prep}} = 480 \mu\text{s}$ . Again black line indicates polarization achieved with only with optical pumping.

In presence of photon detection shot noise, increasing the duration of the preparation time window increases the confidence in our estimate of the  $^{14}\text{N}$  state and therefore improves the measured spin polarization (see also the discussion for  $^{13}\text{C}$  environment in Section 4.5). At the same time for measurement based preparation to be successful, the nuclear state should remain in the dark state during the preparation window.



## *Appendix B: Supporting material for Chapter 4*

---

When the NV is optically excited the  $^{14}\text{N}$  is being driven to a steady state with finite polarization. As a result the success probability of post-selection decreases if the preparation time window becomes too long. Both of these effects are illustrated in Figure B.4 b: as the conditioning time increases ( $\tau_{\text{prep}}$ ), the observed polarization increases while the decrease in success probability results in larger errorbars. We experimentally found that the 500  $\mu\text{s}$  window used in the Chapter 4 gives the maximum polarization while still maintaining an acceptable signal to noise.

To determine the result of measurement based preparation we record the counts in a time interval at the end of the preparation step. This ensures that the preceding optical cooling does not affect the prepared state and also increases the success probability for finding the  $^{14}\text{N}$  in the desired state. By using counts from the last 500  $\mu\text{s}$  of the preparation laser pulse, measurement based preparation of the  $^{14}\text{N}$  state yields higher polarization compared to the optical cooling method. This is because we can detect the  $^{14}\text{N}$  state faster than the timescale for its evolution under optical excitation ( $\tau_1 \sim 350\mu\text{s}$ ). This is further illustrated by Figure B.4c. It shows that optical excitation after initializing the state with measurement based preparation decreases the achieved polarization, and brings it to its steady state value.

## **B.5 Strain dependence of CPT width**

In the absence of a DC magnetic field, the ground state spin properties of the NV center is significantly altered by strain or electric fields around the NV [143, 89]. For example, the zero magnetic field ESR spectrum around  $m_I = 0$  shown in Figure B.5 clearly shows a doublet where a single peak with a width of  $1/T_2^*$  would be expected.

### Appendix B: Supporting material for Chapter 4

---

This observed effect has been explained by the presence of strain terms in the ground state Hamiltonian (following the notation in [89]):

$$H_{\text{gs}} = \left( hD_{\text{gs}} + d_{\text{gs}}^{\parallel} \Pi_z \right) S_z^2 + g\mu_b S_z B_z + d_{\text{gs}}^{\perp} \left[ \Pi_x (S_x S_y + S_y S_x) + \Pi_y (S_x^2 - S_y^2) \right]$$

where  $d_{\text{gs}}^{\perp}/h = 17 \pm 3 \text{ Hz cm V}^{-1}$   $\Pi_x$  and  $\Pi_y$  are the components of the strain/electric field vector perpendicular to the NV axis along the molecular axes of the N-V center [143],  $S_i$  are the corresponding spin 1 angular momentum operators and  $h$  is the Planck's constant,  $hD_{\text{gs}}$  is the 2.878 GHz zero field splitting and an external magnetic field in the  $z$  direction has been assumed, where  $z$  direction is parallel to the NV axis. The  $z$  component of strain changes the zero field splitting of the NV center and is inconsequential to this work. With  $\frac{\Delta}{2} = \sqrt{\Pi_x^2 + \Pi_y^2} d_{\text{gs}}^{\perp}$  and  $\frac{\Delta}{2} \cos \theta = \Pi_x d_{\text{gs}}^{\perp}$  and  $\frac{\Delta}{2} \sin \theta = \Pi_y d_{\text{gs}}^{\perp}$ , we can re-write the effective Hamiltonian for the  $|\pm 1\rangle$  states in a very simple form:

$$H_{\text{eff}} = \frac{1}{2} \left( \delta | +1 \rangle \langle +1 | - \delta | -1 \rangle \langle -1 | - \Delta i e^{+i\theta} | +1 \rangle \langle -1 | + \Delta i e^{-i\theta} | -1 \rangle \langle +1 | \right)$$

where  $\delta$  is the two photon detuning as in Section B.2 ( $\delta = 2g\mu_b B_z$ ). For  $\delta = 0$ , strain fixes the eigenstates to particular superpositions of  $|+1\rangle$  and  $|-1\rangle$  states, and these eigenstates are split in energy by  $\Delta$ . As Figure B.5 indicates  $\Delta = 170 \text{ kHz}$  for an excited state splitting of 6 GHz (corresponding to NVc). We use this value to calibrate the ground state strain splitting for other NVs [89]. We measured an  $|E_x\rangle$  -  $|E_y\rangle$  splitting of 3.5 GHz for NVa and 7.5 GHz for NVb corresponding to ground state strain splittings of 100 kHz and 210 kHz respectively.

Since a careful analysis has already been carried out in Section B.2 describing the effects of other levels, here we will concentrate on quantifying the effects of strain on

Appendix B: Supporting material for Chapter 4

---

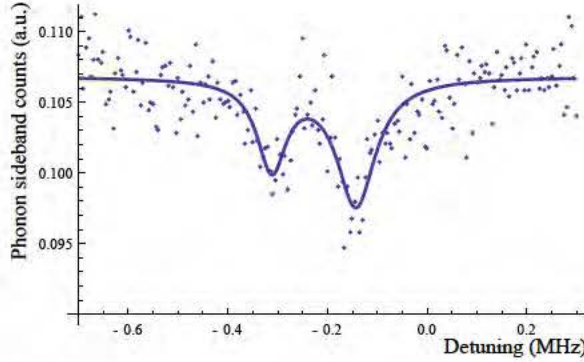


Figure B.5: Measured ESR spectrum for  $B \sim 0$  for an NV with an excited state  $E_x$  and  $E_y$  splitting around 6 GHz. Spectra is measured by first pumping all of the population to the  $|0\rangle$  state and then applying a resonant weak microwave pulse of duration  $35 \mu\text{s}$  whose frequency is tuned. The population in the  $|0\rangle$  state is measured afterwards using the  $|0\rangle$  to  $|E_y\rangle$  transition and integrating the counts for a  $10 \mu\text{s}$  window. The zero of the scan range corresponds to 2.878 GHz. The two peaks (fitted with Lorentzians) are separated by  $170 \pm 6 \text{ kHz}$  and their FWHM widths are  $70 \pm 14 \text{ kHz}$  (center around -312 kHz) and  $94 \pm 14 \text{ kHz}$  (center around -142 kHz)

the CPT experiment using a simple model based on the above effective Hamiltonian. The CPT phenomenon can easily be explained in the context of the bright and dark states, so we will use them as the basis states in our model. We optically pump the system into the dark state let it evolve according to the ground state Hamiltonian for time  $T$ , followed by a measurement of the population in the bright state. The linear polarization of the CPT laser used for this measurement determines the angle  $\phi$  as the phase between the two circularly polarized components. This phase in turn sets the particular superpositions that form the dark state  $|D\rangle = \frac{1}{\sqrt{2}} (e^{i\phi} |+1\rangle - e^{-i\phi} |-1\rangle)$  and bright state  $|B\rangle = \frac{1}{\sqrt{2}} (e^{i\phi} |+1\rangle + e^{-i\phi} |-1\rangle)$ .

Within this model the population in the bright state can be easily calculated:

$$\left| \langle B | e^{-iT H_{\text{eff}}} | D \rangle \right|^2 = \frac{1}{2} \frac{\delta^2 + \Delta^2 \cos^2(\theta + 2\phi)}{\frac{R^2}{4} + \Delta^2 + \delta^2}$$

## Appendix B: Supporting material for Chapter 4

---

Where  $\langle \dots \rangle_T$  refers to the average over the classical random variable  $T$ <sup>1</sup>. This indicates that the HWHM of the CPT dip is determined by  $\sqrt{R^2/4 + \Delta^2}$ , as discussed in Chapter 4. The contrast of the CPT dip is determined by the polarization dependent quantity  $\frac{\Delta^2 \cos^2(\theta+2\phi)}{\frac{R^2}{4} + \Delta^2}$ . For  $R \gg 2\Delta$  good contrast is expected regardless of the polarization of light. For  $R \ll 2\Delta$ , the polarization of light relative to the strain axis determines the visibility of the CPT dip. This fact is very easy to interpret in two limits. First if  $\theta + 2\phi = 0$ , no CPT dip is visible at low pumping rates. This special case corresponds to the bright / dark states defined by the light field being equal superpositions of the eigenstates defined by strain. Any prepared dark state quickly precesses in to an equal superposition of dark / bright states before the measurement by the optical field; under these conditions (regardless of the applied magnetic field), no CPT dip is visible. The other extremal case, when  $\theta + 2\phi = \pi/2$ , corresponds to the bright/states matching the eigenstates defined by strain and therefore having an energy splitting of  $\Delta$ . In this case a dark state clearly exists for  $\delta \ll \Delta$  as there is negligible precession rate out of the dark state.

We re-emphasize that all of the CPT datasets shown have been taken with an optimal linear polarization that maximizes the CPT contrast observed at low powers. Thus in Section B.2 it is assumed that the bright/dark states defined by the light field matches the eigenstates defined by strain.

---

<sup>1</sup>The average time  $T$  is linked to optical pumping rate by:  $\langle T \rangle_T = 1/R$ , where  $T$  is assumed to be an exponentially distributed random variable.

## B.6 Autocorrelation measurements and spectral density of signal

Here we present an additional analysis of the autocorrelation results shown in the Chapter 4. To confirm that the observed timescales are indeed due to nuclear dynamics, we performed a control experiment where the fixed magnetic detuning is tuned 4 MHz away from the  $m_I = +1$  state. As Figure B.6a illustrates, there is a clear difference in the amplitudes of the features observed between the case when the fixed magnetic field is located at a CPT dip or away from a CPT dip. However the timescales extracted using fits to double exponential decays are quite similar:  $350 \pm 30 \mu\text{s}$  and  $8400 \pm 200 \mu\text{s}$  for the dataset in a CPT dip and  $760 \pm 200 \mu\text{s}$  and  $10700 \pm 800 \mu\text{s}$  for the datasets where  $B$  is tuned away from the CPT dip. To be able to compare the two datasets easily we have normalized both autocorrelation spectra such that the 0 time delay points are at 1. The 0 time delay point is not shown in the plots because they are purely due to the shot-noise in our detector and the low mean count rate per bin  $80 \mu\text{s}^2$ .

The oscillations observed in the autocorrelation data can be ascribed to harmonics of 60 Hz that is caused by experimental noise. To clearly demonstrate this we show the power spectrum of the two datasets for which the autocorrelations have been

---

<sup>2</sup>Our signal can be approximated by a random variable that gives us the counts obtained per bin  $c_n$  where  $n$  is the index of the bin. If shot noise is the only process that determines  $c_n$ , then  $c_n$  become independent Poissonian random variables with a mean  $\lambda$  determined by the time-bin size, collection efficiency, and the mean excited state population. The zero delay autocorrelation value is given by  $\langle \sum_n c_n c_n \rangle = \sum_n \langle c_n^2 \rangle = \sum_n (\lambda^2 + \lambda)$  while for any other delay  $j$  the autocorrelation is given by  $\langle \sum_n c_n c_{n-j} \rangle = \sum_n \langle c_n \rangle \langle c_{n-j} \rangle = \sum_n \lambda^2$ . Since our count rate is relatively low such that  $\lambda \leq 1$ , the zero-delay point in autocorrelation is significantly higher compared to the rest of the values.

*Appendix B: Supporting material for Chapter 4*

---

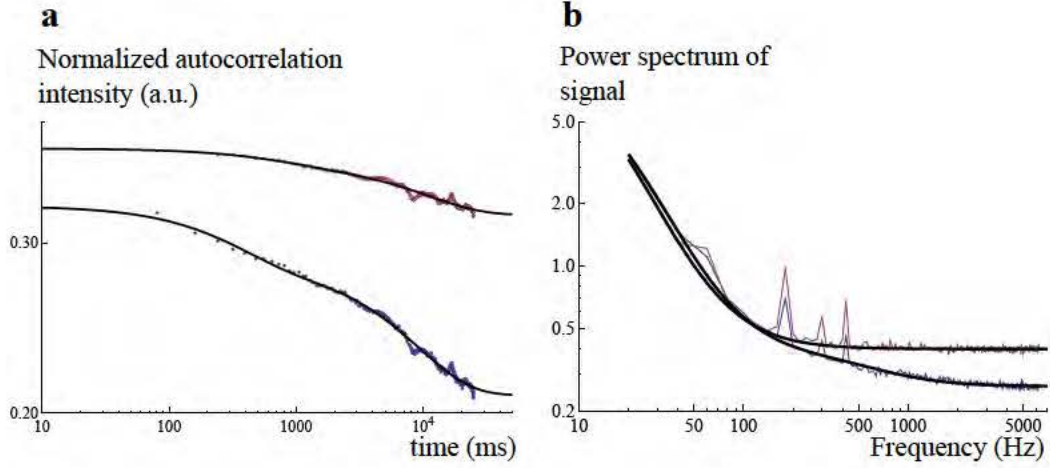


Figure B.6: Spectral and statistical properties of the observed CPT signal at a constant external magnetic field. (a) Autocorrelation of the intensity for two constant magnetic fields in a log-log scale when the external magnetic field is tuned away from CPT resonance (red) and when the external field is tuned to be 0.3 MHz away from the center of the  $m_I = +1$  resonance (blue), as explained in Chapter 4. (b) Power spectrum of the same signal in a log-log scale clearly showing the harmonics of 60 Hz lines and the difference of the off-resonance (red) and on-resonance (blue) for both low frequencies and for high frequencies.

shown. As Figure B.6b illustrates, there are clear peaks at odd harmonics of the AC line frequency of 60 Hz (180 Hz, 300 Hz, 420 Hz), and these features are present for both datasets regardless of whether or not the external magnetic field is tuned to be within a CPT dip. This clearly shows that the observed 60 Hz is not magnetic in character, hence our results are not affected by the magnetic environment of the room (which is dominated by 60 Hz noise).

We note that the power-spectrum within the CPT resonance is well described by a sum of two lorentzians (with timescales given by  $350 \pm 30 \mu\text{s}$  and  $8.4 \pm 0.2 \text{ ms}$ ). Since the power spectrum of the noise and autocorrelation functions are linked by Fourier transform, this justifies the use of double exponential decays as a model for



the autocorrelation function.

The two timescales associated with the CPT dip are tentatively ascribed to processes associated with the nuclear spin environment. The fast time-scale corresponds well with the  $^{14}\text{N}$  diffusion timescale (see Section 4.3), and we assign the slower timescale to light induced changes in the  $^{13}\text{C}$  nuclear environment. The presence of the two timescales in both datasets, although with very different amplitudes, may be qualitatively explained by the slight sensitivity of our CPT signal to magnetic field fluctuations even away from the CPT resonance.

Even though the 8 ms timescale is long compared to most of our experiments, this value determines the timescale in which a prepared distribution of the Overhauser field remains unchanged under optical illumination and hence is an important factor in determining the utility of the narrowed distribution (see section 10 for an application to magnetic field sensing). We have carried out experiments to verify that this slow timescale is due to reconfiguration of the  $^{13}\text{C}$  environment. The results are presented in the next section, where we outline measurements in which the magnetic field is changed quickly under continuous optical illumination.

## **B.7 Nuclear configuration measurements using fast magnetic field ramps**

We examine here in more detail the experiments presented in Figure 4.3b and c where the magnetic field was swept across one of the  $^{14}\text{N}$  resonances within a relatively short time period. We now show the complete experimental sequence where

*Appendix B: Supporting material for Chapter 4*

a (forward) rising sweep proceeds the falling sweep that has already been discussed in the Chapter 4. Using both directions of the magnetic field scan, we can extract additional information about the dynamics of the  $^{13}\text{C}$  spin bath.

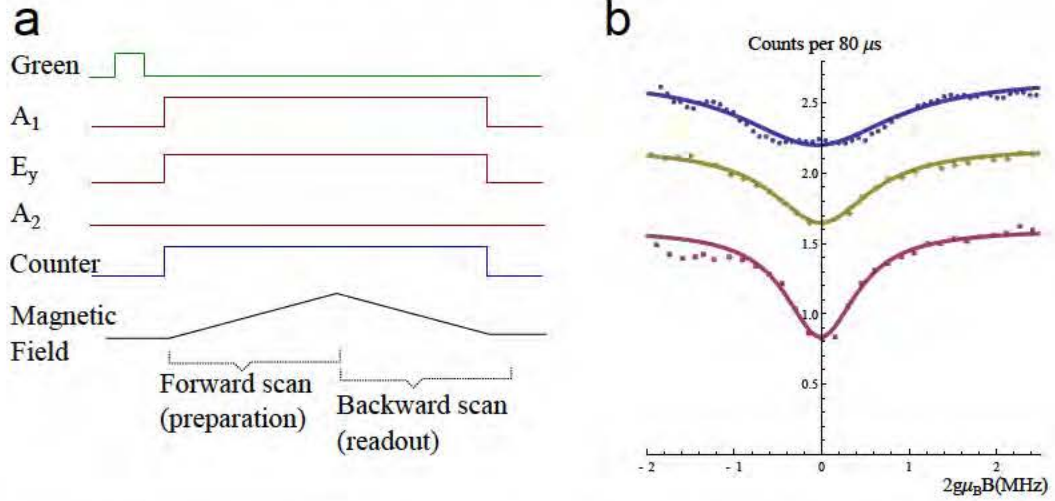


Figure B.7: Observation of the instantaneous configuration of the  $^{13}\text{C}$  spin bath. (a) Complete pulse sequence for real-time measurement of the  $^{13}\text{C}$  nuclear configuration. Counts are recorded in  $80\ \mu\text{s}$  time bins. (b) Blue: Average of  $\sim 15000$  forward scans that passed verification, showing full width of  $^{14}\text{N}$  line given by  $1/T_2^*$ . Red: Average of the same forward scans after shifting each individual run by the center position of their fitted CPT lines. Yellow: Average of the backward scans after shifting each run by the fitted CPT line position of its corresponding forward scan. Blue, and yellow curves have been shifted up for clarity by 1 and 0.5 counts respectively.

First, we can compare the values of our estimate of the Overhauser field between the forward and the backward scans. Figure B.7 shows in blue the average counts obtained during the forward scan. We perform Lorentzian fits to individual forward scans, and consider the fit successful if the parameters for the fitted distribution falls within the averaged CPT line. Specifically if the fitted width is between 20 kHz (frequency sampling interval), and 2 MHz (overall width of the unconditioned CPT width), and the center of the width is within 1.4 MHz of the center of the



*Appendix B: Supporting material for Chapter 4*

---

unconditioned with the fit considered to be succesful. The red curve is obtained by shifting (or re-centering) individual forward scans by its corresponding fitted center of the CPT dip if the fit succeeds. Clearly the red curve is a factor of  $\sim 2$  narrower compared to the average scan. We can further verify that the environment remains in this measured configuration by shifting the backward scan based on the value of the Overhauser field estimated using the preceding forward scan. This then produces the yellow curve which is again a factor of  $\sim 1.4$  narrower compared to the un-shifted curve. This shows that we are indeed observing instantaneous configurations of the magnetic field environment with a lifetime greater than the single-direction ramp time of 5 ms.

The results of the preceding analysis motivates a method of measuring the timescale of  $^{13}\text{C}$  spin bath dynamics by changing the the time of the field ramps and looking at correlations between the position of the CPT resonance on the forward and backward scans. To prepare a particular nuclear spin configuration during the forward scan, we select runs in which the number of counts is zero for two successive time bins corresponding to a particular value of the magnetic field  $B_0$ . For the graphs and discussion shown in this section we pick  $B_0$  so the state is prepared at the center of the  $^{13}\text{C}$  distribution. The resulting distribution of counts is shown in Figure B.8a. Plotting the averaged counts during the backward scan for these selected runs reveals a narrowed distribution around  $B_0$ . By repeating this measurement for increasing ramp times, we see that the features in the post-selected data begins to broaden, indicating decreasing correlations between the Overhauser field during the forward and backward scans as they become further separated in time. We find that the timescale

## Appendix B: Supporting material for Chapter 4

of this  $^{13}\text{C}$  spin bath reconfiguration to be on the order of five milliseconds, consistent with the results of the autocorrelation data in the previous section.

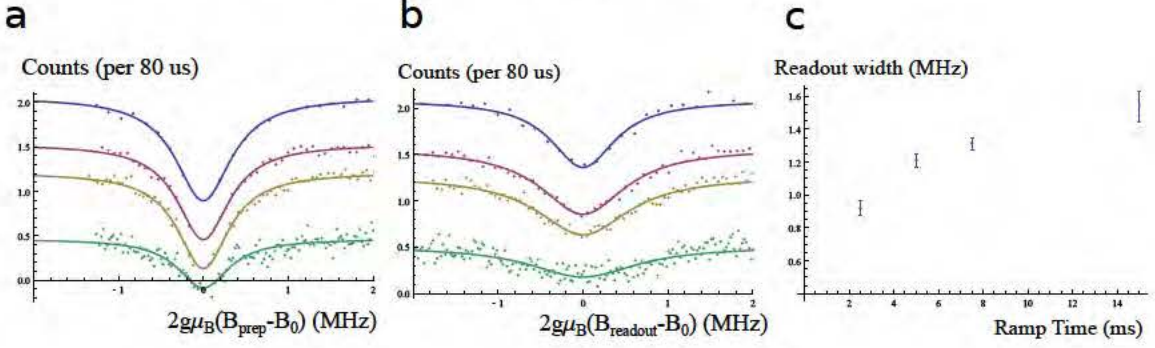


Figure B.8: Analysis of forward and backward scans using the forward scan as preparation and backward scan as readout. (a) Distribution of counts in the forward scan if we post-select those runs who have two successive 0 counts around  $B_{\text{prep}} = B_0$ . The selected points (artificially zero) have been dropped from the figure. The times for each ramp direction are 2.5 ms (blue), 5 ms (red), 7.5 ms (yellow) and 15 ms (green). The widths of the fits are roughly the same for all timescales. Blue, red, yellow and green curves have been shifted vertically by 0.2, -0.05, -0.3, -0.55 counts respectively for clarity. (b) The corresponding plot of the selected backward scans with the same vertical shifts as in (a). (c) Extracted width as a function of the ramp time.

## B.8 $B_{\text{prep}}$ dependence of the observed width

In this section we will demonstrate that a narrow conditional distribution can be prepared for any value of the two photon detuning that remains within the  $^{13}\text{C}$  distribution. However we show that the minimal value of the narrowed width occurs away from the center of the distribution.

To explore this effect we carry out a similar experiment to the one described in Figure 4.4 of the Chapter 4 (and the pulse-sequence reproduced in Figure B.10), where we now vary the external magnetic field  $B_{\text{prep}}$  during the preparation step

*Appendix B: Supporting material for Chapter 4*

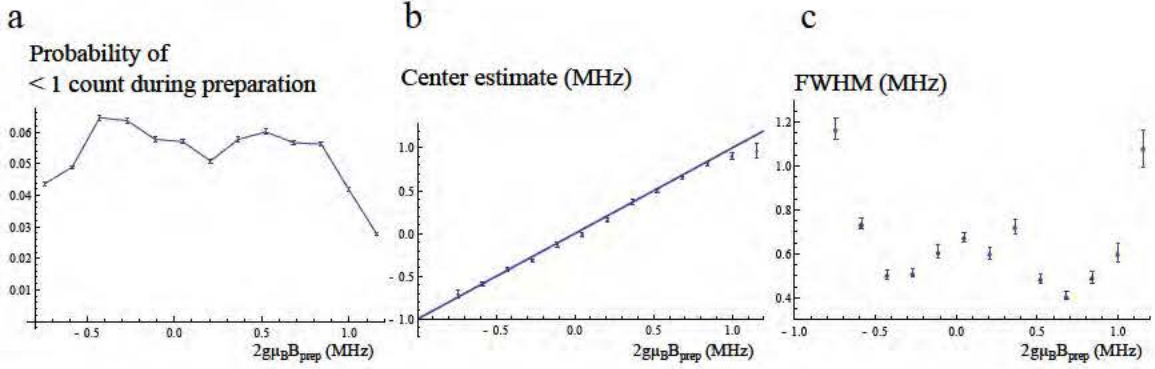


Figure B.9: Dependence of the conditional CPT dip as a function of  $B_{\text{prep}}$  for NVb. (a) Change in the probability of detecting less than 1 count as a function of  $B_{\text{prep}}$ . (b) Center estimate of the conditional distribution as obtained from a single Lorentzian fit. (c) Estimate of the width of the conditional distribution as a obtained from a single Lorentzian fit.

and obtain narrowing data for different  $B_{\text{prep}}$ . The data showing the properties of the narrowed CPT dip is summarized in Figure B.9 for NVb. While  $B_{\text{prep}}$  remains within the  $^{13}\text{C}$  distribution, we are able to prepare a relatively narrow CPT dip. As Figure B.9b illustrates, the center of the narrowed CPT dip follows  $B_{\text{prep}}$  exactly. As one moves further away from the center of the  $^{13}\text{C}$  distribution the probability of being able to prepare the narrowed CPT dip changes. Specifically, far away from the center of the distribution the probability decreases significantly (this is partially illustrated in Figure B.9a), but never decreases to zero. The width of the narrowed distribution also changes as  $B_{\text{prep}}$  moves away from the center of the  $^{13}\text{C}$  distribution. In fact the narrowest feature is found away from the center. Similar results were obtained for another center (NVa).

In our discussions so far we have treated the nuclear environment as a collective system which can be characterized by a density of states. The fact that the center

### *Appendix B: Supporting material for Chapter 4*

---

estimate of the narrowed distribution follows  $B_{\text{prep}}$  value supports this argument. The variation of the narrowed width as well as the probability of successful state preparation as a function of  $B_{\text{prep}}$  indicates that a varying density of states may be playing a role in these experiments.

Qualitatively we expect the lifetime of the nuclear environment to be proportional to the density of available states that yield that particular magnetic field value. As the number of ways of escaping from the particular configuration is given by the possible ways in which the nuclear spins can flip-flop between each-other the higher density configurations should have a higher rate of escape. The associated density distribution for the nuclear state of the carbon bath is expected to be peaked at the center, hence we expect the smallest lifetime to be given at the center. With a small lifetime, the prepared state can possibly change before or during the readout stage, yielding a width that is wider compared to the case where the magnetic environment does not change. Even though the lifetime should get longer as we move towards the edge of the  $B$  distribution, the probability of finding the system in those configurations is also lower. In the presence of false events that produce 0 counts during preparation, the lower probability of finding the environment in the desired state would imply that one should obtain the unprepared distribution for these cases and the width should increase. Based on these qualitative arguments we expect the width to be given by the shape observed in Figure B.9c. We note that this argument could be further studied using the experiment described in Section B.6. Further exploration is needed to determine the exact mechanism of diffusion between different nuclear spin states and its effect on nuclear state preparation.



## Appendix B: Supporting material for Chapter 4

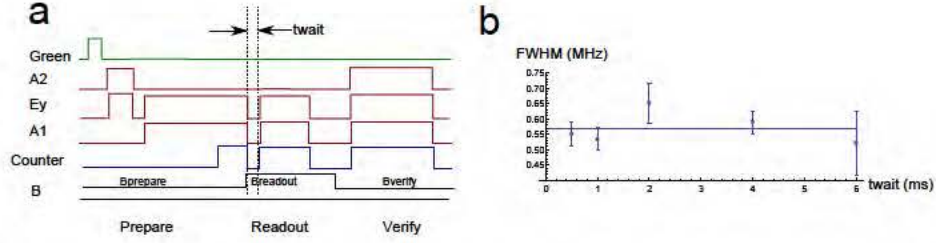


Figure B.10: Change of the conditional CPT width as a function of dark wait time. (a) Pulse sequence describing the experiment. The wait time (between the preparation step and the readout step) is varied and a different CPT spectrum is obtained for each point similar to Figure 4.4 in the Chapter 4. Verification step is shown for completeness. (b) A plot of the extracted width as a function of the wait time  $t_{\text{wait}}$  showing no significant change up to 6 ms.

## B.9 Lifetime in the absence of optical fields

In our discussions of nuclear dynamics we have neglected any evolution in the absence of optical light fields. We now present data that suggests that lifetime associated with prepared Overhauser field distribution in the dark is much longer than 6 ms.

To probe the effects of evolution in the dark, we repeat the experiment illustrated in Figure 4.4 where we now change the wait time  $t_{\text{wait}}$  between the preparation and readout. A change in the nuclear environment within this time would affect a change in the width of the CPT signal that we observe in the readout step.

Figure B.10 illustrates the widths of the readout observed as a function of the wait time  $t_{\text{wait}}$ . No noticeable change in the width occurs within 6 ms of  $t_{\text{wait}}$ , indicating that if any change occurs within this time its effect on the Overhauser field distribution is negligible for the results that we are reporting.

## B.10 Discussion

In this section we apply the results of the model developed in Section B.2 to estimate the limits of measurement-based narrowing of Overhauser distribution and discuss possible application of these techniques for magnetometry. In the following  $R_E \gg \gamma$  is assumed.

To explore the limits on narrowing given by  $\delta_c$  we will consider two separate cases. In the first case, applicable to current experimental realization, we assume that preparation is limited by finite strain. The minimum  $\delta_c$  is achieved by setting  $R_A = 4\Delta$  (equation B.8). For this optimal value we find that

$$\delta_c = \sqrt{\frac{2 \ln 2 \Delta \eta / \epsilon}{T_{\text{cond}}}}. \quad (\text{B.11})$$

For the current experimental parameters, and  $T_{\text{cond}} \sim 8$  ms, we estimate that Overhauser distribution as narrow as 23 kHz and 40 kHz could be prepared for NVa and NVb, respectively. Note that preparation of such a narrow distribution can not verified directly via dark-resonance measurement near zero magnetic field since the readout linewidth itself is limited by strain.

The limit associated with strain could be circumvented by using two-frequency dark resonance excitation in a Raman configuration at high magnetic field ( $g_B B \gg \Delta$ ). In the case of slowly evolving nuclei,  $R_A$  and  $T_{\text{cond}}$  are then the only parameters that define the width of prepared distribution  $\delta_c$ . To decrease the CPT linewidth,  $R_A$  can be made very small, at the cost of reduced number of counts. To ensure that a sufficient number of counts is obtained to differentiate the dark state we require that  $CT_{\text{cond}} > 1$ , which gives a minimal  $R_A$ . Using this minimal  $R_A$ , and assuming that

*Appendix B: Supporting material for Chapter 4*

---

$T_{\text{cond}}\gamma\epsilon \gg 1$ , we find

$$\delta_c^{\text{min}} \simeq \frac{\sqrt{\ln 2}\eta/\epsilon}{2T_{\text{cond}}}. \quad (\text{B.12})$$

This analysis thus indicates the present method should allow us to reach Heisenberg limited narrowing  $\delta_c^{\text{min}} \simeq \frac{1}{T_{\text{cond}}}$  with a modest improvement in collection efficiency (from the current  $\epsilon = 5 \times 10^{-4}$  to  $\epsilon = 10^{-2}$ ). This appears to be well within the reach of current experiments using e.g. solid immersion lenses (SILs) [90]. Note that  $T_{\text{cond}}$ , and correspondingly the narrowing, is eventually limited by the lifetime of prepared nuclear configuration  $T_1^{\text{nuc}}$  [82].

Finally, we outline how the techniques described in this work can be used for sensing external magnetic fields. As compared with conventional methods involving microwave manipulation and readout with an off-resonant green laser [144], our method can improve the magnetic sensitivity in a number of ways. First of all, we note that use of the presented CPT-based method with a recycling transition results in an improved readout mechanism (gain in sensitivity  $\times 6$ ), along with a gain in sensitivity by employing both  $|+1\rangle$  and  $|-1\rangle$  states for magnetic field detection (gain in sensitivity  $\times \sqrt{2}$ ). Note that, by improving the collection efficiency by a factor of 10, the increase in the number of counts could boost the sensitivity by an additional factor of three.

Further improvement can be obtained via conditional preparation of nuclear environment demonstrated here. Specifically, reduction of the uncertainty in the Overhauser field by setting it to a well-defined value via e.g. feedback control significantly improves the sensitivity to low-frequency magnetic fields. For example, if one operates at high bias fields such that the method is limited by the dynamical evolution of the

*Appendix B: Supporting material for Chapter 4*

---

nuclear environment, the resultant resonance narrowing could be as much as  $1 \text{ ms}/1\mu\text{s} \sim 10^3$ . When combined with improved readout, the sensitivity to low frequency (DC) magnetic fields could then be potentially improved from about  $\mu\text{T Hz}^{-1/2}$  [144] to  $\text{nT Hz}^{-1/2}$ .



# Bibliography

- [1] C. W. Chou, D. B. Hume, J. C. J. Koelemeij, D. J. Wineland, and T. Rosenband. Frequency comparison of two high-accuracy  $\text{al}^+$  optical clocks. *Phys. Rev. Lett.*, 104:070802, Feb 2010.
- [2] T. L. Nicholson, M. J. Martin, J. R. Williams, B. J. Bloom, M. Bishof, M. D. Swallows, S. L. Campbell, and J. Ye. Comparison of two independent sr optical clocks with  $1 \times 10^{-17}$  stability at  $10^3$  s. *Phys. Rev. Lett.*, 109:230801, Dec 2012.
- [3] C. Benko, A. Ruehl, M. J. Martin, K. S. E. Eikema, M. E. Fermann, I. Hartl, and J. Ye. Full phase stabilization of a yb:fiber femtosecond frequency comb via high-bandwidth transducers. *Opt. Lett.*, 37(12):2196–2198, Jun 2012.
- [4] T. Kessler, C. Hagemann, C. Grebing, T. Legero, U. Sterr, F. Riehle, M. J. Martin, L. Chen, and J. Ye. A sub-40-mhz-linewidth laser based on a silicon single-crystal optical cavity. *Nature Photonics*, (10):687–692, 2012.
- [5] P. Shor. Algorithms for quantum computation: discrete logarithms and factoring. In *Foundations of Computer Science, 1994 Proceedings., 35th Annual Symposium on*, pages 124–134, 1994.
- [6] H. J. Kimble. The quantum internet. *Nature*, 453:1023, 2008.
- [7] S. Lloyd. Universal quantum simulators. *Science*, 273(5278):1073–1078, 1996.
- [8] C. Monroe and J. Kim. Scaling the ion trap quantum processor. *Science*, 339(6124):1164–1169, 2013.
- [9] D. D. Awschalom, L. C. Bassett, A. S. Dzurak, E. L. Hu, and J. R. Petta. Quantum spintronics: Engineering and manipulating atom-like spins in semiconductors. *Science*, 339(6124):1174–1179, 2013.
- [10] J. Clarke and F. K. Wilhelm. Superconducting quantum bits. *Nature*, 453(7198):1031–1042, 2008.
- [11] A. Stern and N. H. Lindner. Topological quantum computation from basic concepts to first experiments. *Science*, 339(6124):1179–1184, 2013.

## Bibliography

---

- [12] P. M. Platzman and M. I. Dykman. Quantum computing with electrons floating on liquid helium. *Science*, 284(5422):1967–1969, 1999.
- [13] D. Ristè, J. G. van Leeuwen, H.-S. Ku, K. W. Lehnert, and L. DiCarlo. Initialization by measurement of a superconducting quantum bit circuit. *Phys. Rev. Lett.*, 109:050507, Aug 2012.
- [14] F. Mallet, F. R. Ong, A. Palacios-Laloy, F. Nguyen, P. Bertet, D. Vion, and D. Esteve. Single-shot qubit readout in circuit quantum electrodynamics. *Nat. Phys.*, 5(11):791–795, 2009.
- [15] M. D. Reed, L. DiCarlo, S. E. Nigg, L. Sun, L. Frunzio, S. M. Girvin, and R. J. Schoelkopf. Realization of three-qubit quantum error correction with superconducting circuits. *Nature*, (7385):382385, 2012.
- [16] L. Steffen, Y. Salathe, M. Oppliger, P. Kurpiers, M. Baur, C. Lang, C. Eichler, G. Puebla-Hellmann, A. Fedorov, and A. Wallraff. Deterministic quantum teleportation with feed-forward in a solid state system. *Nature*, (7462):319–322, 2013.
- [17] Y. Nakamura, Y. A. Pashkin, and J. S. Tsai. Coherent control of macroscopic quantum states in a single-cooper-pair box. *Nature*, 398:786–788, 1999.
- [18] H. Paik, D. I. Schuster, L. S. Bishop, G. Kirchmair, G. Catelani, A. P. Sears, B. R. Johnson, M. J. Reagor, L. Frunzio, L. Glazman, S. M. Girvin, M. H. Devoret, and R. J. Schoelkopf. Observation of high coherence in josephson junction qubits measured in a three-dimensional circuit qed architecture. *arXiv*, quant-ph:1105.4652v4, 2011.
- [19] C. Rigetti, J. M. Gambetta, S. Poletto, B. L. T. Plourde, J. M. Chow, A. D. Córcoles, J. A. Smolin, S. T. Merkel, J. R. Rozen, G. A. Keefe, M. B. Rothwell, M. B. Ketchen, and M. Steffen. Superconducting qubit in a waveguide cavity with a coherence time approaching 0.1 ms. *Phys. Rev. B*, 86:100506, Sep 2012.
- [20] J. M. Martinis, K. B. Cooper, R. McDermott, M. Steffen, M. Ansmann, K. D. Osborn, K. Cicak, S. Oh, D. P. Pappas, R. W. Simmonds, and C. C. Yu. Decoherence in josephson qubits from dielectric loss. *Phys. Rev. Lett.*, 95:210503, Nov 2005.
- [21] R. H. Koch, D. P. DiVincenzo, and J. Clarke. Model for  $1/f$  flux noise in squids and qubits. *Phys. Rev. Lett.*, 98:267003, Jun 2007.
- [22] B. B. Blinov, D. L. Moehring, L. M. Duan, and C. Monroe. Observation of entanglement between a single trapped atom and a single photon. *Nature*, 428:153, 2004.

## Bibliography

---

- [23] A. Sipahigil, M. L. Goldman, E. Togan, Y. Chu, M. Markham, D. J. Twitchen, A. S. Zibrov, A. Kubanek, and M. D. Lukin. Quantum interference of single photons from remote nitrogen-vacancy centers in diamond. *Phys. Rev. Lett.*, 108:143601, Apr 2012.
- [24] H. Bernien, L. Childress, L. Robledo, M. Markham, D. Twitchen, and R. Hanson. Two-photon quantum interference from separate nitrogen vacancy centers in diamond. *Phys. Rev. Lett.*, 108:043604, Jan 2012.
- [25] H. Bernien, B. Hensen, W. Pfaff, G. Koolstra, M. S. Blok, L. Robledo, T. H. Taminiau, M. Markham, D. J. Twitchen, L. Childress, and R. Hanson. Heralded entanglement between solid-state qubits separated by three metres. *Nature*, 497(7447):86–90, 2013.
- [26] F. Bardou, J.-P. Bouchaud, A. Aspect, and C. Cohen-Tannoudji. *Levy statistics and laser cooling: How rare events bring atoms to rest*. Cambridge University Press, 2002.
- [27] A. Aspect, E. Arimondo, R. Kaiser, N. Vansteenkiste, and C. Cohen-Tannoudji. Laser cooling below the one-photon recoil energy by velocity-selective coherent population trapping. *Phys. Rev. Lett.*, 61(7):826–829, Aug 1988.
- [28] J. A. Gupta, R. Knobel, N. Samarth, and D. D. Awschalom. Ultrafast manipulation of electron spin coherence. *Science*, 292(5526):2458–2461, 2001.
- [29] Y. L. A. Rezus, S. G. Walt, R. Lettow, A. Renn, G. Zumofen, S. Götzinger, and V. Sandoghdar. Single-photon spectroscopy of a single molecule. *Phys. Rev. Lett.*, 108:093601, Feb 2012.
- [30] H. de Riedmatten, M. Afzelius, M. U. Staudt, C. Simon, and N. Gisin. A solid-state lightmatter interface at the single-photon level. *Nature*, (7223):773–777, 2008.
- [31] A. L. Falk, B. B. Buckley, G. Calusine, W. F. Koehl, V. V. Dobrovitski, A. Politi, C. A. Zorman, P. X.-L. Feng, and D. D. Awschalom. Polytype control of spin qubits in silicon carbide. *Nature Communications*, page 1819, 2013.
- [32] A. M. Zaitsev. *Optical Properties of Diamond: A Data Handbook*. Springer, 2010.
- [33] J. Maze, A. Gali, E. Togan, Y. Chu, A. Trifonov, E. Kaxiras, and M. Lukin. Properties of nitrogen-vacancy centers in diamond: the group theoretic approach. *New J. Phys.*, 13:025025, 2011.
- [34] J. Loubser and J. V. Wyk. Electron spin resonance in the study of diamond. *Rep. Prog. Phys.*, 91:1201, 1978.

## Bibliography

---

- [35] J. Goss, R. Jones, S. Breuer, P. Briddon, and S. Oberg. The twelve-line 1.682 eV luminescence center in diamond and the vacancy-silicon complex. *Phys. Rev. Lett.*, 77:3041, 1996.
- [36] A. Lenef and S. Rand. Electronic structure of the NV center in diamond: Theory. *Phys. Rev. B*, 53:13441, 1996.
- [37] A. Gali, M. Fyta, and E. Kaxiras. Ab initio supercell calculations on nitrogen-vacancy center in diamond: Electronic structure and hyperfine tensors. *Phys. Rev. B*, 77:155206, 2008.
- [38] L. Rogers, R. McMurtrie, M. Sellars, and N. B. Manson. Time-averaging within the excited state of the nitrogen-vacancy centre in diamond. *New Journal of Physics*, 11:063007, 2009.
- [39] N. B. Manson, J. P. Harrison, and M. J. Sellars. Nitrogen-vacancy center in diamond: Model of the electronic structure and associated dynamics. *Phys. Rev. B*, 74:104303, Sep 2006.
- [40] A. Batalov, V. Jacques, F. Kaiser, P. Siyushev, P. Neumann, L. J. Rogers, R. L. McMurtrie, N. B. Manson, F. Jelezko, and J. Wrachtrup. Low temperature studies of the excited-state structure of negatively charged nitrogen-vacancy color centers in diamond. *Phys. Rev. Lett.*, 102(19):195506, May 2009.
- [41] G. D. Fuchs, V. V. Dobrovitski, R. Hanson, A. Batra, C. D. Weis, T. Schenkel, and D. D. Awschalom. Excited-state spectroscopy using single spin manipulation in diamond. *Phys. Rev. Lett.*, 101(11):117601, Sep 2008.
- [42] A. Gruber, A. Drbenstedt, C. Tietz, L. Fleury, J. Wrachtrup, and C. v. Borczyskowski. Scanning confocal optical microscopy and magnetic resonance on single defect centers. *Science*, 276(5321):2012–2014, 1997.
- [43] L. Childress, M. V. Gurudev Dutt, J. M. Taylor, A. S. Zibrov, F. Jelezko, J. Wrachtrup, P. R. Hemmer, and M. D. Lukin. Coherent dynamics of coupled electron and nuclear spin qubits in diamond. *Science*, 314(5797):281–285, 2006.
- [44] Y. Shen, T. M. Sweeney, and H. Wang. Zero-phonon linewidth of single nitrogen vacancy centers in diamond nanocrystals. *Phys. Rev. B*, 77:033201, Jan 2008.
- [45] P. Tamarat, T. Gaebel, J. R. Rabeau, M. Khan, A. D. Greentree, H. Wilson, L. C. L. Hollenberg, S. Prawer, P. Hemmer, F. Jelezko, and J. Wrachtrup. Stark shift control of single optical centers in diamond. *Phys. Rev. Lett.*, 97:083002, Aug 2006.

# Bibliography

---

- [46] A. Batalov, C. Zierl, T. Gaebel, P. Neumann, I.-Y. Chan, G. Balasubramanian, P. R. Hemmer, F. Jelezko, and J. Wrachtrup. Temporal coherence of photons emitted by single nitrogen-vacancy defect centers in diamond using optical Rabi-oscillations. *Phys. Rev. Lett.*, 100:077401, 2008.
- [47] V. M. Acosta, C. Santori, A. Faraon, Z. Huang, K.-M. C. Fu, A. Stacey, D. A. Simpson, K. Ganesan, S. Tomljenovic-Hanic, A. D. Greentree, S. Prawer, and R. G. Beausoleil. Dynamic stabilization of the optical resonances of single nitrogen-vacancy centers in diamond. *Phys. Rev. Lett.*, 108:206401, May 2012.
- [48] A. Stacey, D. A. Simpson, T. J. Karle, B. C. Gibson, V. M. Acosta, Z. Huang, K. M. C. Fu, C. Santori, R. G. Beausoleil, L. P. McGuinness, K. Ganesan, S. Tomljenovic-Hanic, A. D. Greentree, and S. Prawer. Near-surface spectrally stable nitrogen vacancy centres engineered in single crystal diamond. *Advanced Materials*, 24(25):3333–3338, 2012.
- [49] N. Aslam, G. Waldherr, P. Neumann, F. Jelezko, and J. Wrachtrup. Photo-induced ionization dynamics of the nitrogen vacancy defect in diamond investigated by single-shot charge state detection. *New Journal of Physics*, 15(1):013064, 2013.
- [50] C. Kurtsiefer, S. Mayer, P. Zarda, and H. Weinfurter. Stable solid-state source of single photons. *Phys. Rev. Lett.*, 85(2):290–293, July 2000.
- [51] P. Tamarat, N. B. Manson, J. P. Harrison, R. K. McMurtie, A. Nizovtsev, and *et al.* Spin-flip and spin-conserving optical transitions of the nitrogen-vacancy centre in diamond. *New J. Phys.*, 10:045004, 2008.
- [52] K.-M. C. Fu, C. Santori, P. E. Barclay, L. J. Rogers, N. B. Manson, and R. G. Beausoleil. Observation of the dynamic Jahn-Teller effect in the excited states of nitrogen-vacancy centers in diamond. *Phys. Rev. Lett.*, 103:256404, Dec 2009.
- [53] C. Santori, P. Tamarat, P. Neumann, J. Wrachtrup, D. Fattal, R. G. Beausoleil, J. Rabeau, P. Olivero, A. D. Greentree, S. Prawer, F. Jelezko, and P. Hemmer. Coherent population trapping of single spins in diamond under optical excitation. *Phys. Rev. Lett.*, 97(24):247401, Dec 2006.
- [54] L. C. Bassett, F. J. Heremans, C. G. Yale, B. B. Buckley, and D. D. Awschalom. Electrical tuning of single nitrogen-vacancy center optical transitions enhanced by photoinduced fields. *Phys. Rev. Lett.*, 107:266403, Dec 2011.
- [55] L. Robledo, L. Childress, H. Bernien, B. Hensen, P. F. A. Alkemade, and R. Hanson. High-fidelity projective read-out of a solid-state spin quantum register. *Nature*, 477:574–578, 2011.

# Bibliography

---

- [56] L.-M. Duan, J. I. Cirac, and P. Zoller. Geometric manipulation of trapped ions for quantum computation. *Science*, 292(5522):1695–1697, 2001.
- [57] D. Møller, L. B. Madsen, and K. Mølmer. Geometric phase gates based on stimulated raman adiabatic passage in tripod systems. *Phys. Rev. A*, 75:062302, Jun 2007.
- [58] L.-M. Duan and C. Monroe. Robust quantum information processing with atoms, photons, and atomic ensembles. *Advances in Atomic, Molecular, and Optical Physics*, 55:419–464, 2008.
- [59] P. Neumann, N. Mizuochi, F. Rempp, P. Hemmer, H. Watanabe, S. Yamasaki, V. Jacques, T. Gaebel, F. Jelezko, and J. Wrachtrup. Multipartate entanglement among single spins in diamond. *Science*, 320:1326–1329, 2008.
- [60] M. Ansmann, H. Wang, R. C. Bialczak, M. Hofheinz, and E. L. *et al.* Violation of bell’s inequality in josephson phase qubits. *Nature*, 461:504–506, 2009.
- [61] L. DiCarlo, J. M. Chow, J. M. G. L. S. Bishop, B. R. Johnson, and *et al.* Demonstration of two-qubit algorithms with a superconducting quantum processor. *Nature*, 46:240–244, 2009.
- [62] H. de Riedmatten, M. Afzelius, M. U. Staudt, C. Simon, and N. Gisin. A solid-state light-matter interface at the single-photon level. *Nature*, 456:773, 2008.
- [63] G. Balasubramanian, P. Neumann, D. Twitchen, M. Markham, R. Kolesov, and *et al.* Ultralong spin coherence time in isotopically engineered diamond. *Nature Materials*, 8:383, 2009.
- [64] G. D. Fuchs, V. V. Dobrovitski, D. M. Toyli, F. J. Heremans, and D. D. Awschalom. Gigahertz dynamics of a strongly driven single quantum spin. *Science*, 326:1520, 2009.
- [65] M. V. G. Dutt, L. Childress, L. Jiang, E. Togan, J. Maze, and *et al.* Quantum register based on individual electronic and nuclear spin qubits in diamond. *Science*, 316:1312, 2007.
- [66] F. Kaiser, V. Jacques, A. Batalov, P. Siyushev, F. Jelezko, and J. Wrachtrup. Polarization properties of single photons emitted by nitrogen-vacancy defect in diamond at low temperature. *arXiv:0906.3426*, 2009.
- [67] M. O. Scully and K. Druhl. Quantum eraser: A proposed photon correlation experiment concerning observation and “delayed choice” in quantum mechanics. *Phys. Rev. A.*, 25:2208, 1982.

# Bibliography

---

- [68] T. Wilk, S. C. Webster, and G. R. A. Kuhn. Single-atom single-photon quantum interface. *Science*, 317:488–490, 2007.
- [69] D. Moehring, P. Maunz, S. Olmschenk, K. Younge, D. Matsukevich, L. Duan, and C. Monroe. Entanglement of single-atom quantum bits at a distance. *Nature*, 449(7158):68–71, 2007.
- [70] D. Englund, A. Faraon, I. Fushman, N. Stoltz, P. Petroff, and J. Vuckovic;. Controlling cavity reflectivity with a single quantum dot. *Nature*, (7171):857–861, 2007.
- [71] S. Schietinger, T. Schroder, and O. Benson. One-by-one coupling of single defect centers in nanodiamonds to high-q modes of an optical microresonator. *Nano Letters*, 8:3911, 2008.
- [72] C. F. Wang, R. Hanson, D. D. Awschalom, E. L. Hu, T. Feygelson, and *et al.* Fabrication and characterization of two-dimensional photonic crystal microcavities in nanocrystalline diamond. *Appl. Phys. Lett.*, 91:201112, 2007.
- [73] M. Fleischhauer, A. Imamoglu, and J. P. Marangos. Electromagnetically induced transparency: Optics in coherent media. *Rev. Mod. Phys.*, 77:633, 2005.
- [74] K.-K. Ni, S. Ospelkaus, M. H. G. de Miranda, A. Pe’er, B. Neyenhuis, J. J. Zirbel, S. Kotochigova, P. S. Julienne, D. S. Jin, and J. Ye. A high phase-space-density gas of polar molecules. *Science*, 322(5899):231–235, 2008.
- [75] M. O. Scully and M. Fleischhauer. High-sensitivity magnetometer based on index-enhanced media. *Phys. Rev. Lett.*, 69(9):1360–1363, Aug 1992.
- [76] D. Budker and M. Romalis. Optical magnetometry. *Nature Physics*, 3:227–234, 2007.
- [77] J. Vanier. Atomic clocks based on coherent population trapping: a review. *Applied Physics B: Lasers and Optics*, 81:421–442, 2005.
- [78] P. Neumann, J. Beck, M. Steiner, F. Rempp, H. Fedder, P. R. Hemmer, J. Wrachtrup, and F. Jelezko. Single-shot readout of a single nuclear spin. *Science*, 329:542, 2010.
- [79] J. Maze, P. L. Stanwix, J. S. Hodges, S. Hong, J. M. Taylor, P. Cappellaro, L. Jiang, M. V. G. Dutt, E. Togan, A. S. Zibrov, A. Yacoby, R. L. Walsworth, and M. D. Lukin. Nanoscale magnetic sensing with an individual electronic spin in diamond. *Nature*, 455:644–647, 2008.

# Bibliography

---

- [80] G. Balasubramanian, I. Y. Chan, R. Kolesov, M. Al-Hmoud, J. Tisler, C. Shin, C. Kim, A. Wjcik, P. R. Hemmer, A. Krueger, T. Hanke, A. Leitenstorfer, R. Bratschitsch, F. Jelezko, and J. Wrachtrup. Nanoscale imaging magnetometry with diamond spins under ambient conditions. *Nature*, 455:648–651, 2008.
- [81] E. Togan, Y. Chu, A. S. Trifonov, L. Jiang, J. Maze, L. Childress, M. V. G. Dutt, A. S. Sørensen, P. R. Hemmer, A. S. Zibrov, and M. D. Lukin. Quantum entanglement between an optical photon and a solid-state spin qubit. *Nature (London)*, 466(7307):730–734, August 2010.
- [82] M. Issler, E. M. Kessler, G. Giedke, S. Yelin, I. Cirac, M. D. Lukin, and A. Imamoglu. Nuclear spin cooling using overhauser-field selective coherent population trapping. *Phys. Rev. Lett.*, 105(26):267202, Dec 2010.
- [83] G. Giedke, J. M. Taylor, D. D’Alessandro, M. D. Lukin, and A. Imamoglu. Quantum measurement of a mesoscopic spin ensemble. *Phys. Rev. A*, 74(3):032316, Sep 2006.
- [84] L. Robledo, H. Bernien, I. van Weperen, and R. Hanson. Control and coherence of the optical transition of single nitrogen vacancy centers in diamond. *Phys. Rev. Lett.*, 105:177403, Oct 2010.
- [85] B. B. Buckley, G. D. Fuchs, L. C. Bassett, and D. D. Awschalom. Spin-light coherence for single-spin measurement and control in diamond. *Science*, 330(6008):1212–1215, 2010.
- [86] M. O. Scully and M. S. Zubairy. *Quantum Optics*. Cambridge University Press, 1997.
- [87] D. Stepanenko, G. Burkard, G. Giedke, and A. Imamoglu. Enhancement of electron spin coherence by optical preparation of nuclear spins. *Phys. Rev. Lett.*, 96(13):136401, Apr 2006.
- [88] D. Klauser, W. A. Coish, and D. Loss. Nuclear spin state narrowing via gate-controlled rabi oscillations in a double quantum dot. *Phys. Rev. B*, 73(20):205302, May 2006.
- [89] F. Dolde, H. Fedder, M. W. Doherty, T. Nobauer, F. Rempp, G. Balasubramanian, T. Wolf, F. Reinhard, L. C. L. Hollenberg, F. Jelezko, and J. Wrachtrup. Electric-field sensing using single diamond spins. *Nature Physics*, 7:459–463, 2011.
- [90] P. Siyushev, F. Kaiser, V. Jacques, I. Gerhardt, S. Bischof, H. Fedder, J. Dodson, M. Markham, D. Twitchen, F. Jelezko, et al. Monolithic diamond optics for single photon detection. *Appl. Phys. Lett.*, 97(24):241902–241902, 2010.



## Bibliography

---

- [91] G. Chen, D. L. Bergman, and L. Balents. Semiclassical dynamics and long-time asymptotics of the central-spin problem in a quantum dot. *Phys. Rev. B*, 76(4):045312, Jul 2007.
- [92] M. S. Rudner, L. M. K. Vandersypen, V. Vuletic, and L. S. Levitov. Generating entanglement and squeezed states of nuclear spins in quantum dots. *arXiv:1101.3370v2*, 2011.
- [93] F. Verstraete, M. M. Wolf, and J. I. Cirac. Quantum computation and quantum-state engineering driven by dissipation. *Nature Physics*, 5:633 – 636, 2009.
- [94] P. C. Maurer, G. Kucsko, C. Latta, L. Jiang, N. Y. Yao, S. D. Bennett, F. Pastawski, D. Hunger, N. Chisholm, M. Markham, D. J. Twitchen, J. I. Cirac, and M. D. Lukin. Room-temperature quantum bit memory exceeding one second. *Science*, 336(6086):1283–1286, 2012.
- [95] H. D. Robinson and B. B. Goldberg. Light-induced spectral diffusion in single self-assembled quantum dots. *Phys. Rev. B*, 61:R5086–R5089, Feb 2000.
- [96] W. P. Ambrose and W. E. Moerner. Fluorescence spectroscopy and spectral diffusion of single impurity molecules in a crystal. *Nature*, 349(6306):225 – 227, 1991.
- [97] P. Siyushev, H. Pinto, M. Vörös, A. Gali, F. Jelezko, and J. Wrachtrup. Optically controlled switching of the charge state of a single nitrogen-vacancy center in diamond at cryogenic temperatures. *Phys. Rev. Lett.*, 110:167402, Apr 2013.
- [98] J. O. Orwa, C. Santori, K. M. C. Fu, B. Gibson, D. Simpson, I. Aharonovich, A. Stacey, A. Ciminio, P. Balog, M. Markham, D. Twitchen, A. D. Greentree, R. G. Beausoleil, and S. Praver. Engineering of nitrogen-vacancy color centers in high purity diamond by ion implantation and annealing. *Journal of Applied Physics*, 109(8):–, 2011.
- [99] D. E. Chang, A. S. Sorensen, E. A. Demler, and M. D. Lukin. A single-photon transistor using nanoscale surface plasmons. *Nature Physics*, 3(11):807–812, 2007.
- [100] S. Pezzagna, B. Naydenov, F. Jelezko, J. Wrachtrup, and J. Meijer. Creation efficiency of nitrogen-vacancy centres in diamond. *New Journal of Physics*, 12(6):065017, 2010.
- [101] J. Isberg, J. Hammersberg, E. Johansson, T. Wikström, D. J. Twitchen, A. J. Whitehead, S. E. Coe, and G. A. Scarsbrook. High carrier mobility in single-crystal plasma-deposited diamond. *Science*, 297(5587):1670–1672, 2002.

## Bibliography

---

- [102] M. Markham, J. Dodson, G. Scarsbrook, D. Twitchen, G. Balasubramanian, F. Jelezko, and J. Wrachtrup. {CVD} diamond for spintronics. *Diamond and Related Materials*, 20(2):134 – 139, 2011.
- [103] J. F. Ziegler. Particle interactions with matter. <http://www.srim.org>, 2013.
- [104] M. Seal. The effect of surface orientation on the graphitization of diamond. *Physica Status Solidi (b)*, 3(4):658–664, 1963.
- [105] K.-M. C. Fu, C. Santori, P. E. Barclay, and R. G. Beausoleil. Conversion of neutral nitrogen-vacancy centers to negatively charged nitrogen-vacancy centers through selective oxidation. *Applied Physics Letters*, 96(12):121907, 2010.
- [106] J. Rosa, M. Vanecek, M. Nesladek, and L. Stals. Photoionization cross-section of dominant defects in {CVD} diamond. *Diamond and Related Materials*, 8(2-5):721–724, 1999.
- [107] D. Twitchen, D. Hunt, C. Wade, M. Newton, J. Baker, T. Anthony, and W. Banholzer. The production and annealing stages of the self-interstitial (r2) defect in diamond. *Physica B: Condensed Matter*, 273 - 274(0):644 – 646, 1999.
- [108] D. J. Twitchen, M. E. Newton, J. M. Baker, T. R. Anthony, and W. F. Banholzer. Electron-paramagnetic-resonance measurements on the divacancy defect center  $r4/w6$  in diamond. *Phys. Rev. B*, 59:12900–12910, May 1999.
- [109] D. J. Twitchen and M. Markham, 2013. Unpublished work.
- [110] M. A. Lea-wilsonf, J. N. Lomer, and J. A. Van Wyk. Electron spin resonance of the  $r4/w6$  defect in irradiated diamond. *Philosophical Magazine Part B*, 72(1):81–89, 1995.
- [111] D. F. Talbot-Ponsonby, M. E. Newton, J. M. Baker, G. A. Scarsbrook, R. S. Sussmann, and A. J. Whitehead. Epr and optical studies on polycrystalline diamond films grown by chemical vapor deposition and annealed between 1100 and 1900 k. *Phys. Rev. B*, 57:2302–2309, Jan 1998.
- [112] B. Naydenov, F. Reinhard, A. Laemmle, V. Richter, R. Kalish, U. F. S. D’Haenens-Johansson, M. Newton, F. Jelezko, and J. Wrachtrup. Increasing the coherence time of single electron spins in diamond by high temperature annealing. *Applied Physics Letters*, 97(24):242511, Dec 13 2010.
- [113] A. Faraon, C. Santori, Z. Huang, V. M. Acosta, and R. G. Beausoleil. Coupling of nitrogen-vacancy centers to photonic crystal cavities in monocrystalline diamond. *Phys. Rev. Lett.*, 109:033604, Jul 2012.

# Bibliography

---

- [114] T. Babinec, B. Hausmann, M. Khan, Y. Zhang, J. Maze, P. Hemmer, and M. Lončar. A diamond nanowire single-photon source. *Nat. Nanotechnol.*, 5(3):195–199, 2010.
- [115] A. Gali, T. Simon, and J. E. Lowther. An ab initio study of local vibration modes of the nitrogen-vacancy center in diamond. *New Journal of Physics*, 13(2):025016, 2011.
- [116] T. Plakhotnik, W. Moerner, V. Palm, and U. P. Wild. Single molecule spectroscopy: maximum emission rate and saturation intensity. *Optics Communications*, 114(1-2):83 – 88, 1995.
- [117] J. P. Reithmaier, A. L. G. Sek, S. K. C. Hofmann, S. Reitzenstein, L. V. Keldysh, V. D. Kulakovskii, T. L. Reineck, and A. Forchel. Strong coupling in a single quantum dotsemiconductor microcavity system. *Nature*, (7014):197–200, 2004.
- [118] Y. Dumeige, R. Allaupe, P. Grangier, F. Treussart, and J.-F. Roch. Controlling the single-diamond nitrogen-vacancy color center photoluminescence spectrum with a fabryperot microcavity. *New Journal of Physics*, 13(2):025015, 2011.
- [119] P. E. Barclay, C. Santori, K.-M. Fu, R. G. Beausoleil, and O. Painter. Coherent interference effects in a nano-assembled diamond nv center cavity-qed system. *Opt. Express*, 17(10):8081–8097, May 2009.
- [120] D. Englund, B. Shields, K. Rivoire, F. Hatami, J. Vučković, H. Park, and M. D. Lukin. Deterministic coupling of a single nitrogen vacancy center to a photonic crystal cavity. *Nano. Lett.*, 10(10):3922–3926, September 2010.
- [121] A. Faraon, P. Barclay, C. Santori, K. Fu, and R. Beausoleil. Resonant enhancement of the zero-phonon emission from a colour centre in a diamond cavity. *Nature Photon.*, 5(5):301–305, 2011.
- [122] A. Blanco, E. Chomski, S. Grabtchak, M. Ibisate, S. John, S. W. Leonard, C. Lopez, F. Meseguer, H. Miguez, and J. P. Mondia. Large-scale synthesis of a silicon photonic crystal with a complete three-dimensional bandgap near 1.5 micrometres. *Nature*, (6785):437–440, 2000.
- [123] J. D. Joannopoulos, S. G. Johnson, J. N. Winn, and R. D. Meade. *Photonic Crystals: Molding the Flow of Light*. Princeton University Press, 2008.
- [124] K. Srinivasan and O. Painter. Fourier space design of high-q cavities in standard and compressed hexagonal lattice photonic crystals. *Opt. Express*, 11(6):579–593, Mar 2003.

## Bibliography

---

- [125] Q. Quan and M. Loncar. Deterministic design of wavelength scale, ultra-high q photonic crystal nanobeam cavities. *Opt. Express*, 19(19):18529–18542, Sep 2011.
- [126] B. J. M. Hausmann, B. J. Shields, Q. Quan, Y. Chu, N. P. de Leon, R. Evans, M. J. Burek, A. S. Zibrov, M. Markham, D. J. Twitchen, H. Park, M. D. Lukin, and M. Loncar. Coupling of nv centers to photonic crystal nanobeams in diamond. *Nano Letters*, 13(12):5791–5796, 2013.
- [127] M. J. Burek, N. P. de Leon, B. J. Shields, B. J. M. Hausmann, Y. Chu, Q. Quan, A. S. Zibrov, H. Park, M. D. Lukin, and M. Loncar. Free-standing mechanical and photonic nanostructures in single-crystal diamond. *Nano Letters*, 12(12):6084–6089, 2012.
- [128] S. Pezzagna, D. Rogalla, H.-W. Becker, I. Jakobi, F. Dolde, B. Naydenov, J. Wrachtrup, F. Jelezko, C. Trautmann, and J. Meijer. Creation of colour centres in diamond by collimated ion-implantation through nano-channels in mica. *Physica Status Solidi (a)*, 208(9):2017–2022, 2011.
- [129] J. Meijer, S. Pezzagna, T. Vogel, B. Burchard, H. Bukow, I. Rangelow, Y. Sarov, H. Wiggers, I. Plmel, F. Jelezko, J. Wrachtrup, F. Schmidt-Kaler, W. Schnitzler, and K. Singer. Towards the implanting of ions and positioning of nanoparticles with nm spatial resolution. *Applied Physics A*, 91(4):567–571, 2008.
- [130] S. Mosor, J. Hendrickson, B. C. Richards, J. Sweet, G. Khitrova, H. M. Gibbs, T. Yoshie, A. Scherer, O. B. Shchekin, and D. G. Deppe. Scanning a photonic crystal slab nanocavity by condensation of xenon. *Applied Physics Letters*, 87(14):141105, 2005.
- [131] G. Waldherr, Y. Wang, S. Zaiser, M. Jamali, T. Schulte-Herbrueggen, H. Abe, T. Ohshima, J. Isoya, P. Neumann, and J. Wrachtrup. Quantum error correction in a solid-state hybrid spin register. *arXiv:1309.6424*, 2013.
- [132] C. Nölleke, A. Neuzner, A. Reiserer, C. Hahn, G. Rempe, and S. Ritter. Efficient teleportation between remote single-atom quantum memories. *Phys. Rev. Lett.*, 110:140403, Apr 2013.
- [133] H. Krauter, D. Salart, C. A. Muschik, J. M. Petersen, H. Shen, T. Fernholz, and E. S. Polzik. Deterministic quantum teleportation between distant atomic objects. *Nature Physics*, (7):400–404, 2013.
- [134] C. Hepp, T. Müller, V. Waselowski, J. N. Becker, B. Pingault, H. Sternschulte, D. Steinmüller-Nethl, A. Gali, J. R. Maze, M. Atatüre, and C. Becher. The electronic structure of the silicon vacancy color center in diamond. *arXiv:1310.3106*, 2013.

# Bibliography

---

- [135] L. J. Rogers, K. D. Jahnke, L. Marseglia, C. Mller, B. Naydenov, H. Schauffert, C. Kranz, T. Teraji, J. Isoya, L. P. McGuinness, and F. Jelezko. Creation of multiple identical single photon emitters in diamond. *arXiv:1310.3804*, 2013.
- [136] Y. Kubo, C. Grezes, A. Dewes, T. Umeda, J. Isoya, H. Sumiya, N. Morishita, H. Abe, S. Onoda, T. Ohshima, V. Jacques, A. Dréau, J.-F. Roch, I. Diniz, A. Auffeves, D. Vion, D. Esteve, and P. Bertet. Hybrid quantum circuit with a superconducting qubit coupled to a spin ensemble. *Phys. Rev. Lett.*, 107:220501, Nov 2011.
- [137] P. Rabl, S. J. Kolkowitz, F. H. L. Koppens, J. G. E. Harris, P. Zoller, and M. D. Lukin. A quantum spin transducer based on nanoelectromechanical resonator arrays. *Nature Physics*, (8):602–608, 2010.
- [138] F. Jelezko and J. Wrachtrup. Quantum information processing in diamond. *J. Phys.: Condens. Matter*, 18:S807–824, 2006.
- [139] J. J. L. Morton, A. M. Tyryshkin, A. Ardavan, S. C. Benjamin, K. Porfyakis, and et al. Bang-bang control of fullerene qubits using ultrafast phase gates. *Nature Physics*, 2:40, 2006.
- [140] Y. Kanazawa. An optimal variable cell histogram based on the sample spacings. *The Annals of Statistics*, 20:291–304, 1992.
- [141] J. Olivero and R. Longbothum. Empirical fits to the voigt line width: A brief review. *J. Quant. Spectrosc. Radiat. Transfer*, 17:233–236, 1977.
- [142] V. Jacques, P. Neumann, J. Beck, M. Markham, D. Twitchen, J. Meijer, F. Keiser, G. Balasubramanian, F. Jelezko, and J. Wrachtrup. Dynamic polarization of single nuclear spins by optical pumping of nitrogen-vacancy color centers in diamond at room temperature. *Phys. Rev. Lett.*, 102:057403, 2009.
- [143] E. Vanoort and M. Glasbeek. Electric-field-induced modulation of spin echoes of n-v centers in diamond. *Chem. Phys. Lett.*, 168:529–532, 1990.
- [144] J. M. Taylor, P. Cappellaro, L. Childress, L. Jiang, D. Budker, P. R. Hemmer, A. Yacoby, R. Walsworht, and M. D. Lukin. High-sensitivity diamond magnetometer with nanoscale resolution. *Nat. Phys.*, 4:810–816, 2008.